

**A 100-electron-beam source from
a high brightness Schottky emitter for fast
patterning applications**

A 100-electron-beam source from a high brightness Schottky emitter for fast patterning applications

PROEFSCHRIFT

ter verkrijging van de graad van doctor
aan de Technische Universiteit Delft,
op gezag van de Rector Magnificus Prof. dr. ir. J. T. Fokkema,
voorzitter van het College voor Promoties,
in het openbaar te verdedigen
op dinsdag 18 november 2008 om 15:00 uur.

door

Yanxia ZHANG

Master of Science
Concordia University, Montreal, Canada

geboren te Huhhot, P.R.China

Dit proefschrift is goedgekeurd door de promotor:

Prof.dr.ir. P. Kruit

Samenstelling promotiecommissie:

Rector Magnificus	voorzitter
Prof. dr. ir. P. Kruit	Technische Universiteit Delft, promotor
Prof. dr. U. Staufer	Technische Universiteit Delft
Prof. dr. H. P. Urbach	Technische Universiteit Delft
Prof. dr. ir. H. S. J. van der Zant	Technische Universiteit Delft
Dr. C. W. Hagen	Technische Universiteit Delft
Dr. E. Munro	MEBS, UK
Prof. dr. ir. A. Gisolf	Technische Universiteit Delft, reserve lid

Het onderzoek beschreven in dit proefschrift is financieel ondersteund door de Novel Electron Source Project (NES).

Printed by PrintPartners Ipskamp, Enschede

ISBN: 978-90-9023706-0

Copyright 2008 by © Y. Zhang

To Xinyang, and my parents

Table of Contents

1 Introduction to Multi-electron-beam Systems	1
1.1 Overview of Multi-electron-beam Systems	1
1.1.1 Multi-axis Systems	5
1.1.2 Multi-source, Single Column Systems	7
1.1.3 Single Source, Single Column Systems	10
1.1.4 Single Source, Multi-column Systems	13
1.1.5 Conclusion	15
1.2 Challenges in the Design of a Multi-electron-beam Source	16
1.2.1 Off-axial Performance of the Schottky Electron Source	16
1.2.2 Aberration Minimization	21
1.2.3 Reduction of Crosstalk, Charging and Contamination	29
1.2.4 Conclusion	32
1.3 Scope of the Thesis	32
1.4 Project Publications	33
 2 Electron Optics of Microlenses with Inclined Beams	 41
2.1 Introduction	42
2.2 Method of Analysis	43
2.3 Aberrations-minimized Microlens Array	45
2.4 Microlens Array in Multibeam Systems	47
2.4.1 The Configuration of the Multibeam Source	49
2.4.2 Multibeam Source Performance	51
2.5 Conclusions.	54
 3 High Brightness Multi-electron-beam Source for Massively Parallel Electron Beam Lithography	 59
3.1 Introduction	60
3.2 The Multibeam Source Configuration.	60
3.3 Aperture Lens.	63

3.4	The Aperture Lens Array	65
3.5	The Off-axial Aberrations of the Macro Lens	69
3.5.1	Transverse Chromatic Aberration of the Macro Lens	71
3.5.2	Field Curvature Correction using Microlens Strength Variation	72
3.6	System Performance	74
3.7	Conclusions	75
4	High Brightness 100-electron-beam Source for High-resolution Applications	77
4.1	Introduction	78
4.2	The Configuration of the Multibeam Source	79
4.3	Axial Aberrations of the Aperture Lens	81
4.4	The Aperture Lens Array	83
4.5	The Accelerator Lens.	87
4.6	Field Curvature Correction.	90
4.7	The Multibeam Source Performance.	91
4.8	Conclusions.	92
5	Integrated Multi-electron-beam Blanker Array for Sub-10 nm Electron beam Induced Deposition	95
5.1	Introduction.	96
5.2	Design of the Integrated Blanker Array	97
5.3	Fabrication.	102
5.4	Conclusions	104
6	Experiments towards a High Brightness 100-electron-beam Source	107
6.1	The Multibeam Source for Experiments	108
6.2	Low Power Schottky Emitter	111
6.2.1	The Experimental Setup	112
6.2.2	Microfabrication of the Extractor Electrode	115
6.2.3	Experimental Results	117
6.2.4	Discussions and Summary.	122
6.2.4.1	The Angular Current Density	122
6.2.4.2	High Voltage Supply	124
6.2.4.3	Microfabrication	125
6.2.4.4	Summary.	126
6.3	The Optical Column.	126
6.3.1	Microfabrication	126

6.3.2	Optical Column Buildup and Alignment	129
6.3.3	Discussions.	133
6.4	The Blanker Array.	134
6.5	Conclusions.	135
7	Summary and Conclusions	137
8	Samenvatting en Conclusies	141
	Acknowledgement	145
	About the Author	147

Chapter 1

Introduction to Multi-electron-beam Systems

1.1 Overview of Multi-electron-beam Systems

The Scanning Electron Microscope (SEM) was pioneered by Von Ardenne in 1937 and first commercialized in 1965 by Cambridge Instruments. In a typical SEM, a high energy electron beam is focused and scanned on the specimen, and high resolution images are produced from signals of electron-material interactions. The wavelength of the high energy electrons is a few picometers. In contrast to optical microscopy, the contribution of diffraction in the beam blur is very small and the ultimate resolution is, for practical purposes, unlimited. Nowadays, with the high brightness Schottky emitter and suitable electron optical configurations, the resolution of a start-of-art electron microscope can be improved to 1 nm with a probe current of a few pico-amperes. Other applications of a focused electron beam system include transmission electron microscopes (TEM), semiconductor inspection tools, electron beam lithography systems, and analytical instruments.

Usually, electron beam systems are characterized by their probe sizes and probe current. To achieve most desirable performance, the optical column is optimized so that the probe current is maximized for a specific probe size. The probe current that can be obtained in a probe-forming system can be expressed as:

$$I_p = B_r \frac{\pi}{4} d_i^2 \pi \alpha^2 V \quad (1-1)$$

where B_r is the reduced brightness of the electron source, d_i is the source image in the probe, V is the beam potential, and α is the aperture angle, *i.e.*, the semi-apex angle of the convergent cone of the electron probe. The probe current, size and aperture angle cannot be adjusted independently because they are related via the reduced brightness. The reduced brightness is uniquely determined by the types of electron sources and their operating parameters, such as the temperature and the field. It is invariant in any electron-optical column.

As shown in Eq. (1-1), the probe current is proportional to the square of the aperture angle, which may be limited by diffraction and aberrations. Diffraction is inversely proportional to α and thus only limiting at an instrument's ultimate resolution. Electron lenses, consisting of a rotational symmetric magnetic or electrostatic field, in most cases, determine the aperture angle by their spherical and chromatic aberrations. Compared to optical lenses, the aberrations of electron lenses are much larger: the typical electron-probe aperture is limited to around 0.5 degree by lens aberrations, while the aperture angle is up to 70 degrees in an optical microscope. The large aberrations of electron lenses are due to the impossibility of arbitrarily shaping the lens surface and non-existence of strong negative lenses. Apart from the source brightness, diffraction and lens aberrations, the total current is affected by the Coulomb repulsions, too.

The progress in microelectronics, microfabrication and material science demands an ever-increasing spatial resolution and throughput in electron optical systems. Along with the continuous resolution improvement, the throughput of electron beam systems, however, becomes lower due to the fact that the probe current is proportional to the square of the source image in the probe, as shown in Eq. (1-1).

The throughput has been a major problem for electron beam systems, especially for electron beam lithography system where high current is desired. Electron beam lithography is usually referred as maskless lithography because it does not require a mask to generate the final pattern. Instead, the final pattern is created from a digital representation on a computer, and the beam is switched on / off as it scans across the resist-coated substrate to write the pattern. This “serial” nature of electron beam lithography makes the pattern generation very slow compared with a parallel technique such as photolithography. In photolithography, the final pattern is patterned at once by projecting the photomask - a media that stores the pattern information - onto the resist-coated substrate. Due to its low throughput, electron beam lithography is primarily used for manufacturing photomasks. Nowadays, a set of masks costs several million dollars and it becomes a big burden in terms of cost and turnaround time between design and market.

A great alternative of photolithography would be high throughput maskless lithography, where the need for the photomasks is eliminated and a reasonable throughput such as a few wafers per hour can be realized. Various system concepts, writing strategies, and high brightness electron sources have been developed to increase the throughput. The most straightforward way to increase the throughput is to replace the Gaussian beam with a variable-shaped beam (VSB) [1.1]. In a VSB system, the electron beam is shaped by two square apertures: shaping signals are applied to electrostatic deflectors and the electron beam passing the first aperture will shift laterally with respect to the second shaping aperture. The compound image formed by both apertures is subsequently demagnified and projected onto the wafer. In a Gaussian beam system, the intensity distribution of the electron probe can be described by Gaussian function and the achievable beam current is limited by the Coulomb interactions. The VSB systems, on the other hand, do not suffer from the interactions to such a degree because the beam current is less concentrated in its conjugated planes and at the targeted substrate. The VSB increases the exposure rate by projecting typically up to 100 image pixels in parallel. The throughput is restricted for complex patterns because the pattern has to be divided into many smaller elementary shapes. By replacing the second square aperture in

the VSB system with an array of complicated cell patterns, the shot number can be reduced drastically. This is called variable electron beam cell projection lithography (VCP) [1.2]. However, as the technology node shrinks down, it is more and more difficult for VSB and VCP systems to obtain a practical throughput due to electron-electron interactions. Electron-beam-projection methods represent another approach: that is, a large subfield of the mask is illuminated to produce the corresponding image on the target in one shot. The two most promising candidates of the projection methods were SCALPEL (Scattering with Angular Limitation Projection Electron-beam Lithography) and PREVAIL (Projection Reduction Exposure with Variable Axis Immersion Lenses). Unlike the conventional projection methods where the masks consist of transmitting and absorbing regions, SCALPEL [1.3] makes use of the difference in electron scattering properties of different portions of the mask, and higher resolution can be achieved. In a SCALPEL system, the mask is illuminated by a stationary beam while mechanically scanning the reticle and wafer at 4:1 speed ratio. A filter is located at the back focal plane of the projection lens to filter out electrons that have large scattering angles to generate a high contrast image. PREVAIL [1.4] carries the concept of SCALPEL further by combining electronic beam scanning with continuous stage motions. This approach provides a significantly larger effective field size and higher throughput. However, the masks for SCALPEL and PREVAIL are a metal scattering layer on a 100 nm silicon nitride membrane with supporting struts, which raise severe practical challenges. And the fact that a mask must be fabricated is a burden in terms of the cost and turn around time. Finally, a crossover in the projection system results in Coulomb interactions, which induces beam blur and displacement, and limits the system throughput.

The concept of multi-electron beam systems, aiming at improving the throughput of electron beam systems without suffering from source brightness limitations and Coulomb interactions, was first introduced in the late sixties [1.5]. The research and development of multibeam systems continues with different approaches in many groups worldwide, which can be subdivided into 4 categories:

1) multi-axis systems [1.6-1.15]: where multiple miniaturized single-beam columns are arrayed to generate multiple beams;

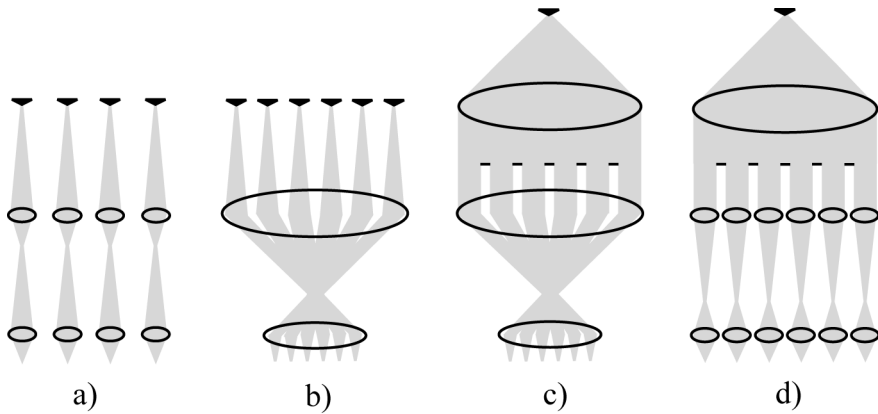


Figure 1-1: a) multi-axis systems; b) multi-source, single column systems; c) single source, single column systems, and d) single source, multi-column systems.

2) multi-source, single column systems [1.18-1.32] where multiple beams are generated from a multiple-laser-driven photocathode or an emitter array. The beams are subsequently delivered to a single optical column;

3) single source, single column systems[1.34-1.45], where multiple beams are created from a single electron source and delivered to a single column; and

4) single source, multi-column systems, where massive parallel beams emitted from a single source are projected by multiple columns at the wafer.

The schematic of these four multi-electron beam systems are illustrated in Figure 1-1.

1.1.1 Multi-axis Systems

The concept of arrayed micro-columns [1.6-1.8], as shown in Figure 1-2.a, was first invented at IBM, developed later at Etec and now at Novellx. As shown, each miniature electron column consists of a low-extraction-voltage thermal field emitter and optical components

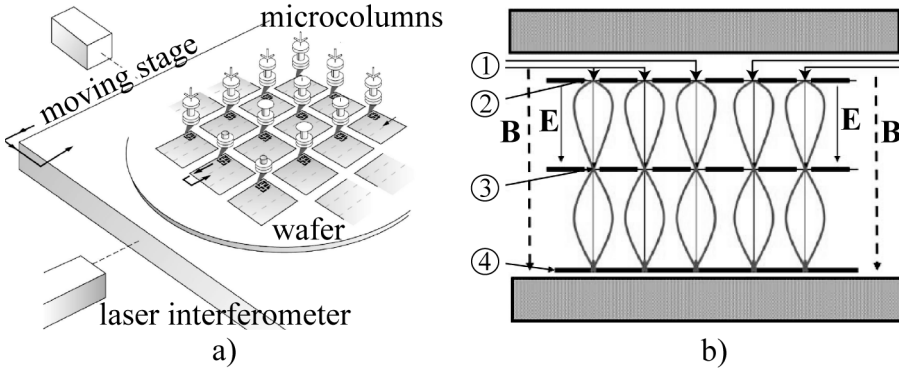


Figure 1-2: a) arrayed micro-columns (from [1.6]); b) distributed axis electron beam system for lithography (from [1.15])

fabricated using MEMS (Micro-Electro-Mechanical System) technology, including an objective lens, a blanker, an octupole deflector and a condenser lens. The advantages of the arrayed columns are that high brightness electron sources are used and there is no Coulomb interactions or crosstalk between the beams. Two columns in a 1 x 4 micro-column array have been tested simultaneously and demonstrated with 75 nm half-pitch lines written into resist. However, it is difficult either to scale up the number of columns or scale down with the technology node, due to the obstacles of making each column delivering the same current with the same probe sizes at desired positions.

The arrayed columns can also employ the variable shaped beam or cell projection principles [1.9-1.10]. The column pitch is typically 25 mm, fabricated using precision mechanical machining. The system usually has a vector scan beam deflection and a “write-on-the-fly” stage motion control. This method is very effective, particularly in the writing of memory patterns containing a lot of repetitions, because only a few cells dramatically reduce the number of shots. However, when fabricating patterns with few repetitions, the throughput is limited by the number of cells. The concept faces similar technical challenges as the arrayed micro-columns, *e.g.*, individual column calibration.

The distributed-axis, variable-shaped (DiVa) system [1.11-1.15] has been proposed for maskless lithography and inspection, where a uniform

axial magnetic field focuses multiple beams simultaneously, as shown in Figure 1-2.b. The spot sizes at the wafer are diffraction-limited, as aberrations of the uniform field are claimed to be negligible. In the DiVa system, the planar cathode acts as a mask in the convention lithography: the electrons emitting from the patterned cathode are focused onto the wafer with one-to-one magnification. Because of this fixed one-to-one imaging, the pattern fidelity of the cathodes must be at least as good as the required pattern fidelity in the printed image. In addition, the patterned areas of the cathode must emit uniformly and stably to within approximately one percent. Few, if any, experiment result is published for the DiVa system due to the unavailability of appropriate cathodes. Sub-100 nm resolution has been demonstrated with the distributed-axis, fixed-aperture (DiFa) system, where a LaB_6 cathode and a source-aperture are used and only one single beam is imaging. The resolution of the DiFa system, certainly, is determined by the size of the source-aperture.

DAFEA (Digitally Addressable Field Emitter Array) [1.16] is another multi-axis system. The emitters are vertically aligned carbon nanofibers grown on a substrate with CMOS integrated circuits. The emitters are individually addressed by the logic, memory and control circuits. When biased sufficiently negative relative to the extraction grid, the emitters are switched on. The electrostatic focusing is integrated on the DAFEA. These electrodes are separated by SiO_2 . Initial experiments of a 3×3 array present $1 \mu\text{m}$ patterns in resist at a working distance of $500 \mu\text{m}$ which extrapolates to around 300 nm at the nominal working distance of $100 \mu\text{m}$ [1.17]. To meet the requirements of lithography, a large array of emitters with stable emission, low noise and long lifetime must be fabricated. Furthermore, all the emission properties of the emitters must be identical. These remain to be the main challenges for this concept.

1.1.2 Multi-source, Single Column Systems

In the multi-axis system, it is difficult to ensure the quality of each projection column and the throughput is limited by the number of columns. A solution would be to use a common projection lens for all the beams, that is, multi-source, single column systems. In such systems,

multiple electron beams may be created by multiple sources, either multiple-laser-driven photocathodes [1.18-1.27] or microfabricated emitter arrays [1.28-1.32]. These arrayed sources are collectively projected, with a conventional single electron-optical column, into an array of demagnified images. At the crossover where all the beams pass through, the electron-electron interactions may induce blur and beam displacement. In addition, the beam pitch is usually smaller than that of the multi-axis system depending on the source pitch and the system demagnification; therefore repulsion between the beams may not be negligible. The Coulomb interactions in such a single column is larger than that of the multi-axis systems. A 50-kV multi-source setup with laser-driven photocathodes, as shown in Figure 1-3.a, has been built and the Coulomb interactions are evaluated [1.24-1.27]. Beam displacement up to tens of nanometers, induced by electron-electron interactions, has been observed in a 32-beam system with a few nano-ampere for each beam. The Coulomb interactions may be reduced by adjusting the beam pitch, column length, and the number of beams. A careful optical design that optimizes the Coulomb interactions, lens aberrations, the system demagnification and the scan field is required.

In the single-axis column with multiple electron sources, off-axial aberrations start to contribute to the beam blur. For instance, the strong extraction field in the gun region acts as a diverging lens, causing the virtual source images formed on a curved surface rather than a flat plane, as illustrated in Figure 1-3.b. A field lens, in close proximity to the photocathode, is necessary to mitigate off-axial aberrations in the subsequent demagnification lenses.

The key challenge for the multi-source single-column systems is, instead of Coulomb interactions and off-axial aberrations which can be optimized, to fabricate photocathodes or microfabricated emitter arrays with high stability, high brightness, low energy spread and long lifetime.

Planar negative-electron-affinity (NEA) photocathodes [1.18-1.23] are promising candidates because of their low energy spread, low emission noise, picosecond-scale switching time, and the ability of producing multiple high-brightness electron beams from low power, inexpensive lasers that are modulated outside the vacuum enclosure. The NEA photocathode normally consists of a semiconductor, usually a III-V

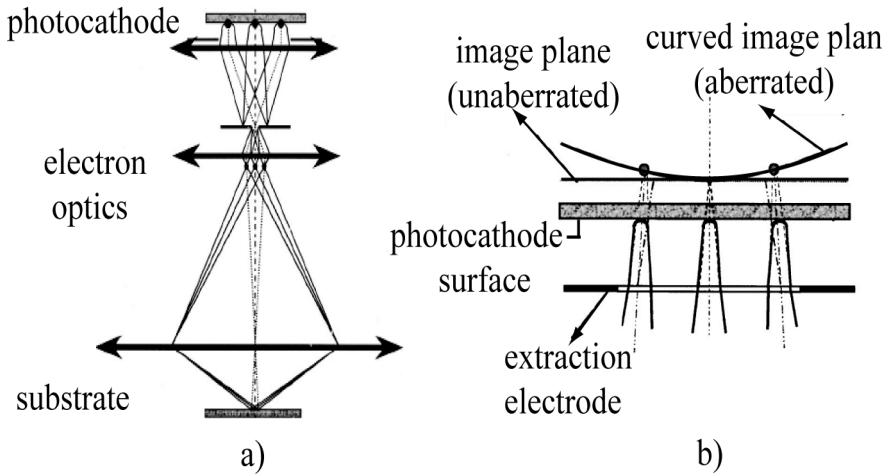


Figure 1-3: a) schematic of multiple electron column; b) details of gun extraction region optics with a ray diagram including aberrations (from [1.26]).

compound such as GaAs, epitaxially grown on top of a diffusion blocking layer on a glass substrate. The semiconductor is heavily *p*-doped so as to raise the conduction band relative to the Fermi level. And an activation layer of cesium and oxygen lowers the work function of the semiconductor such that the conduction band in the bulk is above the vacuum level, a condition named negative electron affinity. The required high current density and brightness, however, may cause significant photocathode degradation due to electron- and photon-stimulated desorption and chemistry at the photocathode and its surrounding surfaces. Moreover, the photocathodes are sensitive to contamination. The stability and lifetime of the NEA photocathode remain to be the obstacles for its application in electron beam lithography.

A very different approach of creating multiple beams is microfabricated cold field emitter arrays [1.28,1.29]. Cold field emitters are promising candidates due to the superior properties of their metal counterparts: high brightness and low energy spread. Microfabricated emitter arrays have additional desirable properties of low operation

voltage, small source spacing and the possibility of volume production. Process development has demonstrated successful fabrication of emitter arrays, however, it is difficult to produce uniform arrays of reliable emitters that fulfill the requirements of lithography or inspection. Oxidation and contamination due to resist outgassing are also big challenges for cold field emitters. Few microfabricated emitter array demonstrates low-noise, stable emission with long lifetime.

An interesting variation of the cold field emitter array is the field emission photocathode array [1.30-1.33]. The field emission photocathode is made of *p*-type semiconductor, which is sensitive to light. The emission is due to the tunnelling of conduction band electrons that are excited from the valence band by a photon. Compared to the planar photocathode, the brightness is enhanced because the emission is defined by the size of field emitters instead of the laser spot. In addition, the emission of these emitters is supposed to be more stable than the conventional cold field emitters because the emission current is determined by the amount of available electrons in the conduction band instead of the tunnelling chance, and a small change in tip radius will not change the emission current. Most obstacles are overcome, such as dark current and low emission stability. However, the two main problems are the instability of the apertured current and the energy shift instability. These phenomena can be explained by a model of the emission process involving an induced *p-n* junction inside the tip. The conclusion, unfortunately, is that *p*-doped silicon field emission photocathodes are not particularly useful for applications in electron beam lithography.

1.1.3 Single Source, Single Column Systems

To avoid a large array of individual electron sources, the concept of multi-electron-beam sources is proposed [1.34-1.46], where multiple beams are created from a single electron source and delivered to a single electron optical column. The multibeam source usually consists of an electron source, a collimator lens, an aperture array and an individually addressed blanker array. Thermionic electron sources, such as LaB₆, are often used because they provide enough current (up to hundreds of micron-amperes) with high current density. The broad beam emitted from

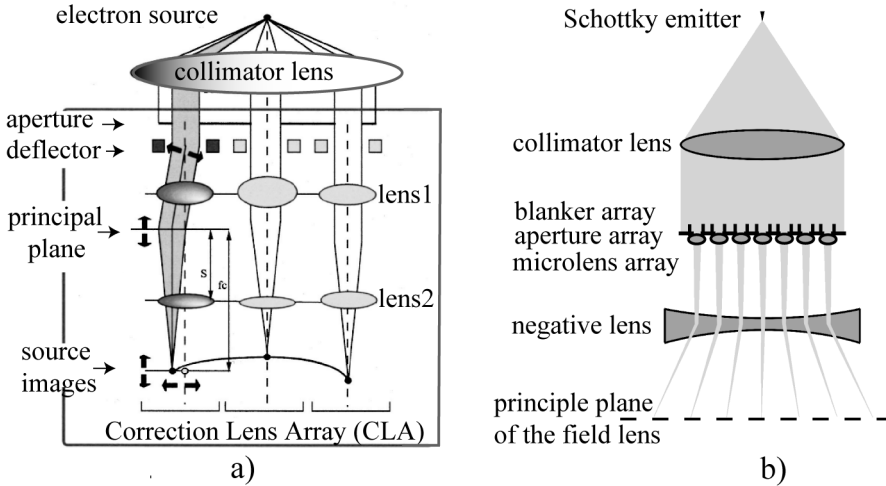


Figure 1-4: a) the correction lens array (from [1.40]); b) the multibeam source for electron beam induced deposition (from [1.42]).

the source is first collimated then split by the aperture array. These beam-defining apertures, usually a square pattern of tens of square microns, serve as secondary source images which are demagnified by the reduction optics. The blanker array is arranged below the aperture array, and together with a beam stop down in the column, switches each beam on/off.

Large demagnification ratio is required to project the micron-sized aperture images. Strong electron lenses are desired due to their smaller axial aberrations. The off-axial aberrations in the reduction optics need to be carefully studied because the typical pitch in the aperture array is 30 μm , around an order of magnitude larger than that in the emitter array, and the off-axial aberrations are much worse for the same number of beams. In case of large imaging and scan field, strong electron lenses increase off-axial aberrations. Tradeoff between axial and off-axial aberration should be considered.

In single source, single column systems, large Coulomb interactions may occur before the broad beam reaches the aperture array, where hundreds of micro-amperes current travels together. Unlike the Coulomb

interactions at the crossover in the projection lens, the e-e interactions before the aperture array do not reduce the resolution, but only result in a lower source brightness and higher energy spread. To reduce the Coulomb interactions, the distance between the electron source and the aperture array should be as short as possible. Having a current limiting aperture directly after the electron source may help to diminish coulomb interactions, too.

Usually, the aberrations in the collimator lens can be neglected for resolution of 100 nm or larger. This is because the blur due to the collimator lens is demagnified together with the aperture images. For high resolution optical columns, however, the aberrations in the collimator lens need to be investigated with caution. For example, Tanimoto and Kamaruri found, in their 65-nm half pitch prototype, that the astigmatic aberration occurring in the illumination optics perturbs the beam travelling angle and is the main cause for misalignment [1.44, 1.45]. The multibeam source used in this prototype differs from the original design in the way it deals with the field curvature and distortion occurring in the objective optics. In the original system [1.40], as shown in Figure 1-4.a, a deflector array and two sets of lens arrays are used between the aperture array and blanker array, which is at the conjugate plane of the source. The deflectors bend the paths of outer beams to compensate distortion. And the field curvature is corrected by adjusting the focal length of individual lenses in the lens arrays. But this original concept is too complex to implement. Van Bruggen [1.42] proposed a multibeam source for the fabrication of sub-10-nm structures. The module comprises of a Schottky emitter, a collimator lens, a blanker array, an aperture array, a microlens array and a negative lens, as shown in Figure 1-4.b. The negative lens, with negative aberration coefficients, is designed to compensate or mitigate the positive aberrations of the collimator lens. Later, however, this mitigation is discovered not sufficient to realize sub-10 nm structures. It is necessary to mention here that the multibeam source proposed by Van Bruggen is the first multibeam source using the Schottky emitter, which is promising for high resolution applications due to its high brightness. In addition, the useful current from a Schottky emitter is around several micro-amperes, the

Coulomb interactions are less severe than that in other multibeam sources.

1.1.4 Single Source, Multi-column Systems

To keep the advantages of a single source and avoid Coulomb interactions in the single column, the single source multi-column concept is developed. MAPPER system [1.47,1.48] is an example of this. Aiming at high throughput maskless lithography, the MAPPER system is designed to generate tens of thousands parallel beams, which are focused and scanned on the wafer simultaneously, as illustrated in Figure 1-5. Each beam can be individually controlled via its own blanker and beam stop aperture. The MAPPER system is a hybrid system: the upper part of the column, having a collimator lens, an aperture array, and a blanker array stimulated via fiber optics, resembles a multibeam source; the lower column resembles a multi-axis system, where each beam has its own beam stop aperture, deflector and projection lens. In contrast to the collective projection, each beam passes its own projection lens without suffering from off-axial aberrations. Projection free from off-axial aberrations is essential to realize tens of thousands of beams. Further,

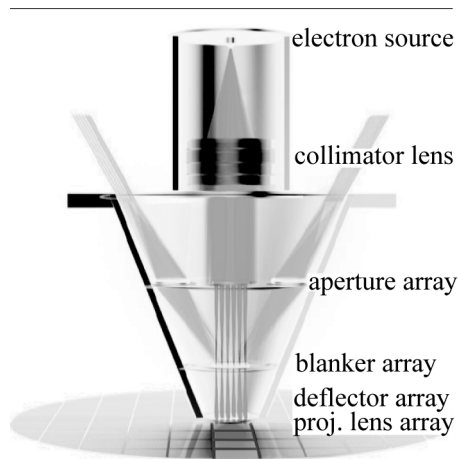


Figure 1-5: Massively parallel multibeam system (from MAPPER Lithography B. V.)

there is no crossover once the broad beam is split by the aperture array, thus the Coulomb interactions can be neglected thereafter.

A large number of beams is appealing for high throughput electron beam lithography, but it also poses several challenges. First of all, such a system demands a low aberration collimator lens, which is capable of illuminating a large field (tens of millimeters) with parallelism of less than 10 micro-radians. Secondly, the Coulomb interactions are expected to be severe due to high current before the aperture array, which may cause large energy spread (thus large chromatic aberration) and defocus. The parallelism of the broad beam is the overall effect of collimating and Coulomb defocus, therefore the collimation needs to be manipulated with caution. Thirdly, in order to have the massive beams writing simultaneously, a blanker array equipped with CMOS (Complementary Metal Oxide Semiconductor) electronics is necessary, which pose a compatibility challenge between the surface micromachining and the bulk micromachining. In addition, fiber optics is used to transfer a large amount of data from the computer to the blanker array, and this may complicate the electronics. And last but not the least, all the beams must be within focus and stigmatic without individual control, and this requires the lens electrodes to be exactly round, all of exactly equal diameter and well aligned. And astigmatism caused by charging or contamination must be prevented at all times [1.47].

The recent progress of Mapper Lithography is the demonstration of 110 electron beams writing simultaneously [1.48]. Out of the 110 beams, 72 beams create 45 nm dense line patterns in resist. These exposure results indeed verify the functionality of the column, including the electron source, the collimator lens, the blanker array, and the projection lens array. Moreover, the multibeam electron optics column meets the requirements for the beam-to-beam critical dimension uniformity: the beam-to-beam critical dimension uniformity is better than 10% of the critical dimension. 25 out of the 110 beams suffered from defocus due to end-of-array effect. This adverse effect, however, can be conveniently removed by adding dummy lenses. In this experiment, the aberrations of the collimator lens are buried by the end-of-array effect and the aberrations of the projection lenses. For the future 13,000-beam lithography system, the angular error due to the collimator lens increases

around 1000 times. It is not difficult to imagine that the massive parallel EBL system works only if the aberrations in the collimator lens are much smaller than what they are now in the demonstrator.

1.1.5 Conclusion

To improve the throughput of electron optical systems, multi-electron-beam systems are proposed, and they can be categorized as: multi-axis systems, multi-source single-column systems, single sources single column systems, and single source multi-column systems. Different approaches are discussed and analyzed. In this work, we choose to continue developing multi-electron-beam sources for the following reasons: first, it doesn't require to calibrate large number of optical columns; second, well-established electron sources can be used, i.e., thermionic sources with high current and stable emission (LaB_6 or CeB_6) or Schottky emitters with high brightness and low energy spread; and third, the multibeam source can be used either in single source single column systems or multi-column systems. Research of the multibeam source will focus on reducing the aberrations and Coulomb interactions, decreasing the crosstalk in the blanker array, and if possible, providing a possibility of compensating the aberrations in the projection optics.

In this work, the Schottky emitter is preferred over the other electron sources. Schottky emitters are well known for their small source size, high current stability, high brightness, low energy spread and long lifetime. Nowadays they are predominant in most commercially available electron-beam instruments. The typical brightness of Schottky emitters is $5 \times 10^7 \text{ A/m}^2\text{srV}$, two decades higher than that of thermionic sources. The Schottky emitters are also preferred over cold field emitters because of their higher stability and less stringent vacuum requirements. The useful current of a Schottky emitter is, however, only several micro-amperes. For high current applications such as high throughput electron beam lithography, we also research the possibility of arraying such multibeam source units to generate tens of thousands of beams. The arrayed multibeam source may act as the source unit for the future generation MAPPER systems.

1.2 Challenges in the Design of a Multi-electron-beam Source

In order to generate multiple high brightness beams with the same probe size and current, the multibeam source should have a low aberration optical column with low Coulomb interactions, and employ conjugate blanking with reduced crosstalk. Therefore, the multibeam source should contain, at least, a Schottky emitter, a beam-splitting aperture array, a microlens array, and a blanker array. The microlens array focuses the sub-beams at the center of blanking electrodes for conjugate blanking. A macrolens, e.g., a collimator lens, might be used.

Challenges of the multibeam source are associated with its requirements and components: 1) obtaining identical probe size and current for all the beams demands identical axial and off-axial performance of the Schottky emitter; 2) the multibeam source should deliver as much current as possible, which necessitates to minimize axial and off-axial aberrations of the microlens array and macrolens; and 3) reducing crosstalk, charging and contamination in the blanker array.

1.2.1 Off-axial Performance of the Schottky Electron Source

The triode-type Schottky gun is shown in Figure 1-6, comprising a ZrO/W(100) emitter, an extractor electrode and a suppressor electrode. Unlike the thermionic gun in which there is a crossover of the electrons, the source image of the Schottky gun is virtual and around 30 μm behind the emitter facet. The work function of the Tungsten (100) crystal face is lowered from 4.2 eV to around 2.9 eV by the ZrO complex supplied by surface diffusion from a ZrO₂ reservoir on the emitter shank. The typical operating temperature is from 1700 K to 1800 K at ultra high vacuum of 10^{-9} mbar. Because the emitter protrudes from the suppressor electrode, the field in front of the emitter is in the order of 5×10^8 V/m. The (100) facet remains stable as long as the field strength exceeds 8×10^8 V/m, which corresponds to an angular intensity of 0.2 mA/sr for a 0.5 μm emitter [1.49].

The high electric field lowers the potential barrier and enhances the emission current with respect to the thermionic emission. The cathode current density J_s for the Schottky emission regime is related to the work function ϕ , temperature T , and electric field F by the Schottky equation [1.49]:

$$J_s = \frac{4\pi me}{h^3} (kT)^2 \exp\left(\frac{e^{3/2} F^{1/2} - \phi}{kT}\right) \quad (1-2)$$

where m , e , k , h are the usual physical constants. The electric field F is equal to the product of the field enhancement factor β and the extraction voltage V_E :

$$F = \beta V_E \quad (1-3)$$

where β (cm^{-1}) is a function of the emitter apex radius r , gun geometry L_{SA} , L_{TA} as shown in Figure 1-6, and the ratio of the suppression voltage over the extraction voltage x [1.49]:

$$\beta = \frac{L_{SA} - (1-x)(L_{TA} - 0.0068)}{0.366 L_{SA} r^{0.758}} \quad (1-4)$$

Usually the Schottky emitter operates in the “extended Schottky regime”, where the tunnelling current cannot be neglected. A measure of the tunnelling current is given by the dimensionless parameter q . For $0.15 < q < 0.7$, the current density can be approximated by [1.49]:

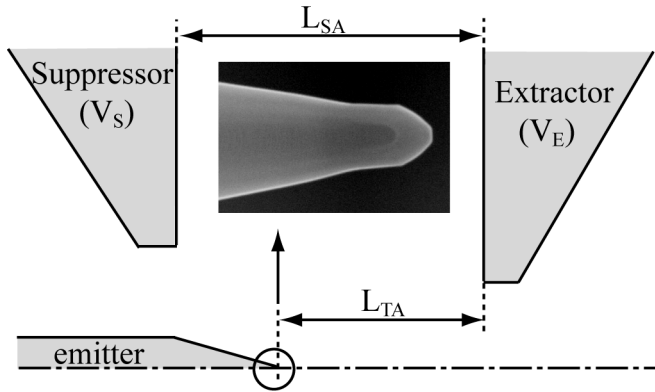


Figure 1-6: The triode-type gun geometry, comprising a Schottky emitter (see insert, from [1.50]), an extractor electrode, and a suppressor electrode.

$$J_{ES} = J_s \frac{\pi q}{\sin(\pi q)} \quad (1-5)$$

The angular current density is related to the cathode current density through the angular magnification m between the cathode surface and the virtual source position, as shown in Figure 1-7. The angular current density can be expressed as [1.49]:

$$I' = \frac{J(r\phi)^2}{\theta^2} = J \left(\frac{r}{m} \right)^2 \quad (1-6)$$

The reduced source brightness can be described as the current per unit area into a solid angle unit divided by the electron acceleration voltage. The reduced brightness only depends on the work function, the electric field at the tip apex and the temperature of the source. Magnifying or aperturing does not change the brightness. For a probe-forming system, it is the “practical reduced brightness” that determines how much current the electron source can deliver in a certain probe size. The practical reduced brightness B_r can be expressed as:

$$B_r = \frac{I'}{\pi/4 d_v^2 V_E} \quad (1-7)$$

where d_v is the FW50 value (full width at 50% current, or the minimum disk containing 50% current) of the virtual source size. In spite of the importance of the reduced brightness, only a few attempts have been

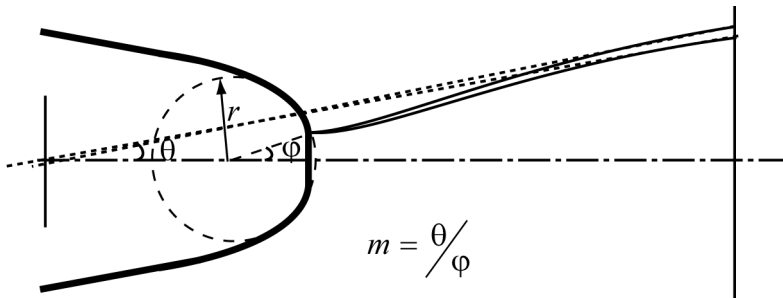


Figure 1-7: The angular magnification m and the trajectories of two electrons with different tangential energy (redrawn from [1.56]).

made to determine it experimentally [1.52-1.55] due to the difficulty of measuring the nanometer scale geometrical source image. In a recent article of Bronsgeest *et al.*[1.56], the FW50 virtual source size is considered at the virtual source plane: the projection of the Gaussian tangential velocity distribution at the emitting surface onto the virtual source plane gives a Gaussian spatial current density distribution, and the FW50 virtual source size can be expressed as:

$$d_v = 1.67 \frac{r}{m} \sqrt{\frac{\langle \mathcal{E} \rangle}{eV}} = 1.67 \frac{r}{m} \sqrt{\frac{kT}{eV_E}} \quad (1-8)$$

where $\langle \mathcal{E} \rangle$ is the mean tangential energy and it is equal to kT for Schottky emitters. Combining Eq. (1-6), Eq. (1-7) and Eq. (1-8), the practical brightness of the Schottky sources can be expressed as [1.56]:

$$B_r = 1.44 \frac{eJ}{\pi kT} \quad (1-9)$$

With the practical reduced brightness, the performance of the axial probe in a multibeam source can be evaluated quantitatively. For the off-axial beams, the probe current - probe size relation cannot be simply quantified with the axial brightness. This is because the electrons arriving at the off-axial lenses originate from an off-center patch in the cathode surface, where the local electric field is higher than that of the central patch. The higher electric field gives the following consequences: 1) according to Eq. (1-2) the current density J at an off-axial cathode surface is higher, and the 'brightness' of the off-axial patch is higher than the axial brightness; and 2) the higher electric field at an off-axial patch also results in a larger angular magnification m . This is also revealed by Fujita [1.57], through the relation between the initial ray position at the cathode surface $r\phi$ and the emission angle θ .

The probe current of an off-axial beam is proportional to the angular current density at its corresponding off-axial position. As shown in Eq. (1-6), the angular current intensity is a function of J and m . At low extraction voltage, the higher J at an off-axial patch cannot balance the higher angular magnification, and the angular current intensity drops at larger emission angles. At high extraction voltage, the emitter works in the extended Schottky regime. The J outweighs the higher angular magnification and the “dog-ears” appear in the emission pattern. For a

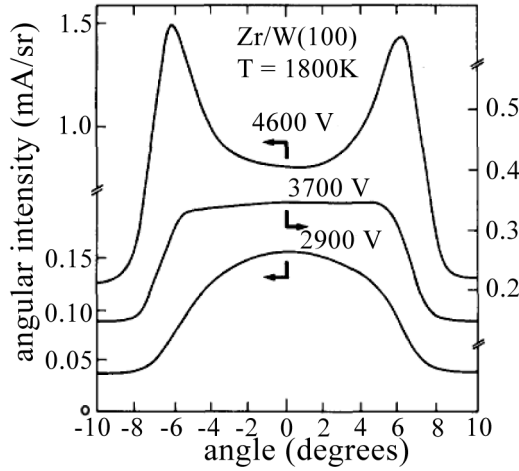


Figure 1-8: Experimentally measured angular current density distribution at the indicated extractor voltages for a ZrO/W emitter with $r = 0.8 \mu\text{m}$ (from [1.51]).

multibeam source, the optimal source operating condition is when the angular current density is uniform over the full emission angle. That is when the higher current density at outer facet is balanced by the larger angular magnification. A typical measured angular current density distribution is shown in Figure 1-8, where the three different emission patterns can be distinguished. By tuning the extraction voltage, a uniform angular current density can be achieved within a half emission angle of around 5 degrees.

The virtual source size seen by an off-axial microlens, in principle, can also be calculated using Eq. (1-8). Due to the larger angular magnification for the off-axial facet at the cathode surface, the virtual source size seen by an off-axial lens is smaller. Thus at the optimal source operation condition, the off-axial beams can deliver the same probe current into a smaller probe size. Therefore, without taking Coulomb interactions and aberrations into account, the off-axial beams outperform the axial beam.

Coulomb interactions may influence the performance of the Schottky emitter. The trajectory displacement enlarges the virtual source size,

resulting in lower source brightness. The trajectory displacement on the axial beam can be estimated with the slice method [1.55], but its influence on the off-axial virtual source size is not yet clear. The Boersch effect broadens the energy spread, and it lowers the resolution through the chromatic aberration. The Boersch effect on the axial beam can be adequately determined by fitting the convolution of the intrinsic distribution and a bell shaped curve representing the Boersch contribution to the experimental data [1.58]. For the off-axial beams at the optimal source operating condition, the current density at an off-axial patch is higher and thus a larger Boersch energy spread is expected.

For all the beams in a multibeam source, the virtual source images are blurred by the spherical and axial chromatic aberrations. In addition, the performance of the off-axial beams may be influenced by the off-axial aberrations. The off-axial probes are also blurred by coma, astigmatism, field curvature and transverse chromatic aberration. In the next section, the aberrations in a multibeam source will be treated separately from the off-axial source performance. Their effects on the off-axial probe sizes will be evaluated for each multibeam configuration.

A more optimistic analysis about the off-axial performance of the Schottky emitter may be found in [1.59]. The actual off-axial performance needs to be verified experimentally.

1.2.2 Aberration Minimization

Without electron-electron interactions, the reduced brightness is conserved throughout the optical column. The probe current and the source image at the target can be calculated through the reduced brightness:

$$I_p = B_r \frac{\pi}{4} (M d_v)^2 \pi \alpha^2 V \quad (1-10)$$

where d_v is the virtual source size, M is the magnification of the optical column, α is the half opening angle of the probe and V is the beam potential at the target.

The source image is, however, blurred at the target as a result of diffraction and aberrations. Barth and Kruit [1.60] have shown the

calculation of FW50 probe size: by wave optical addition of diffraction and spherical aberration contributions and subsequently convolution with the source distribution and chromatic aberration. Note that the full width at 50% of the current is the most popular measure for probe sizes and will be used throughout this thesis, unless otherwise mentioned. The FW50 probe size can be approximated by the following addition rule:

$$d_p = \left\{ \left[d_I^{1.3} + (d_A^4 + d_s^4)^{1.3/4} \right]^{2/1.3} + d_c^2 \right\}^{1/2} \quad (1-11)$$

where d_I , d_A , d_s and d_c are the contributions from the source image, the diffraction disk, the FW50 spherical aberration disk and the FW50 chromatic aberration disk respectively, given by:

$$d_I = M d_v = \frac{2}{\pi} \sqrt{\frac{I}{B_r V}} \frac{1}{\alpha} \quad (1-12)$$

with d_v the virtual source image, M the magnification from the virtual source to the target, and V the beam potential,

$$d_A = 0.54 \frac{\Lambda}{V^{1/2}} \frac{1}{\alpha} \quad (1-13)$$

with $\Lambda = 1.226 \times 10^{-9} \text{ m V}^{1/2}$,

$$d_s = 0.18 C_s \alpha^3 \quad (1-14)$$

with C_s the spherical aberration coefficient of the system, and

$$d_c = 0.6 C_c \frac{\Delta U}{V} \alpha \quad (1-15)$$

with C_c the chromatic aberration coefficient of the system, and ΔU the FW50 of the energy distribution of the source. Note that when the full width at half maximum (FWHM) of the energy spread is used, the prefactor in Eq. (1-15) is 0.34 instead of 0.6.

The optical column is usually optimized so that the contribution of the source image to the probe size is approximately equal to the contributions from the other causes, such as diffraction, aberrations and Coulomb interactions. Kruit *et al.* [1.61] have analyzed the probe current - probe size relation for a two-lens system, comprising a collimating gun lens and a probe-forming lens. The optical system optimization is to

choose the optimal aperture angle which balances the contributions from the probe-forming lens, which increase with α , and the contributions from diffraction, the source image and the gun lens aberrations, which decrease with α . Figure 1-9 plots the probe current vs. probe size relation for the two-lens system with a Schottky emitter. In the graph, three regimes can be defined. At the ultimate resolution of the system as shown in regime 1, the source image and the gun lens aberrations are negligible due to large demagnification. The ultimate resolution depends on the diffraction and the chromatic aberration of the probe-forming lens. In regime 2, with larger aperture angle, the probe size is balanced between the source image and the spherical aberration of the probe-forming lens. The gun lens aberrations start to contribute to the blur. This is illustrated with the dashed line, which is plotted for the same system but having larger gun lens aberration coefficients. In regime 3, where larger source image is projected, the probe size is dominated by the spherical aberration of the gun lens. Figure 1-9 also shows that the maximum probe current is determined by the gun lens aberrations.

Stochastic Coulomb interactions disturb the trajectories and increase the energy spread, causing an additional blur of the probe. Precise

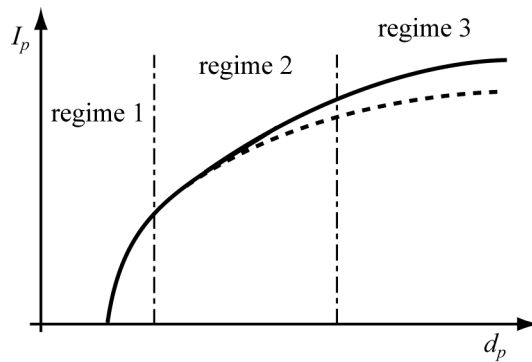


Figure 1-9: The probe current versus probe size in a two-lens optical system comprising a collimating gun lens and a probe-forming lens. A Schottky emitter is used as the electron source. The dashed line is for the same system having larger gun lens aberration coefficients (re-drawn from [1.61]).

calculation of the blur contribution of Coulomb interactions is difficult due to their stochastic nature. Their effect, nevertheless, can be approximated by analytical equations [1.62]. In the two-lens system having a Schottky emitter with brightness of 5×10^7 A/m²srV, the Coulomb interactions do not play a role [1.61].

In a multibeam source, there is usually a current limiting aperture array and the aperture angle is optimized at the blanker array: the geometrical source image at the blanker array is balanced with the blur contributions in the multibeam source. For the multibeam system, usually another current limiting aperture array, the final beam-defining aperture array, is located just before the projection lens. The final apertures angle, corresponding to a half opening angle α_e at the source, should be optimized by balancing the source image at wafer and the blur due to diffraction, aberrations and Coulomb interactions. For a 100-beam source employing a Schottky emitter with several micro-ampere useful current, the probe current is around several nano-amperes. For a typical angular current density of 0.5 mA/sr, the probe half opening angle α_e is several milli-radians. In this regime, the diffraction disk is usually small compared to the source image and thus is negligible. The electron-electron interactions in the multibeam source mainly occur before the broad beam is split. The blur due to Coulomb interactions is expected to be less than that due to aberrations and their effect will be estimated for each multibeam configuration separately. Therefore, the aberrations of microlenses and macrolens, particularly the spherical aberration, are expected to introduce the largest blur and thus determine the half opening angle of the beams. In order to deliver as much current as possible, as the goal for most multibeam systems, a multibeam source with low axial aberrations (allowing a large beam current) and off-axial aberrations (allowing a large number of beams) is desired.

Large off-axial aberrations may be introduced by a macrolens, if there is a macrolens in the multibeam source. The off-axial aberrations of a collimator lens are well explained in [1.63]. The multibeam configuration containing a collimator lens is shown in Figure 1-10.a. The broad beam is refracted to create a parallel beam, which is subsequently split by an aperture array and focused by a microlens array. Seen from a point in the collimator lens, as plotted in Figure 1-10.b, the finite source

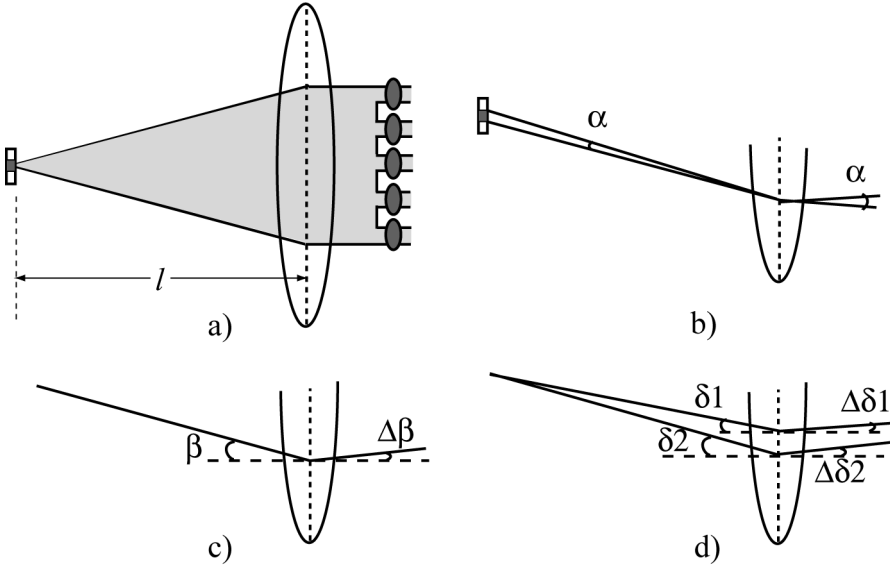


Figure 1-10: The aberrations in a collimator lens: a) the setup configuration; b) the intrinsic opening angle; c) the chromatic aberration; and d) the spherical aberration.

size is equal to $\alpha x/l$, where the finite angle α is called the intrinsic opening angle of the electron beam and l is the distance between the collimator lens and the source. Due to an intrinsic energy spread within the beam, the refraction angle of each electron in the collimator is not well-defined. The axial and transverse chromatic aberrations result in a dispersion $\Delta\beta$ in the beam refraction angle, as shown in Figure 1-10.c. When the $\Delta\beta$ is of the same order as or larger than the intrinsic opening angle α , the size of the source increases from $\alpha x/l$ to $(\alpha + \Delta\beta)x/l$, a significant reduction of resolution results in the off-axis beams.

Besides the dispersion due to the energy spread, the inclination of the off-axis image-forming rays induces geometrical off-axis aberrations at the collimator lens. The effect of the geometrical aberrations is shown in Figure 1-10.d: for two rays with inclination angles of δ_1 and δ_2 impinging at different off-axis positions in the collimator lens, the refraction angles turn away from the collimated direction by $\Delta\delta_1$ and

$\Delta\delta_2$, and $\Delta\delta_2$ is larger than $\Delta\delta_1$ due to the larger off-axial distance. Therefore, the source image seen by the subsequently off-axial microlens is blurred, and at different locations from that seen by the axial microlens. The total effect of these geometrical off-axial aberrations can be separated into four different effects, which together determine the deviation of the actual image from the ideal, sharp, geometrically faithful images. As in the terminology of light optics, these are referred to as coma, field curvature, astigmatism and distortion. Coma causes the image of a point off the axis to assume a cometlike appearance. The dimensions of the comet are proportional to the square of the aperture angle and to the first power of the off-axial distance. Field curvature, if alone present, a perfect sharp image may be obtained on a curved surface. Astigmatism causes the tangential and radial rays not converging at a point, but in two mutually perpendicular line segments. The disks of field curvature and astigmatism in the Gaussian image plane are proportional to the first power of aperture angle and the second power of off-axial distance. And finally, distortion does not affect the sharpness, but only the faithfulness of the image. The deviation of the distortion is proportional to the cube of the off-axial distance. Therefore, the maximum off-axial distance, or the number of the beams, is set by the off-axial aberrations of the collimator lens.

The deteriorative effects of chromatic and geometrical aberrations in the collimator lens can be mitigated, as proposed by Kruit [1.63], by splitting the broad beam and projecting each beam using a microlens array to the principal plane of the collimator lens, as shown in Figure 1-11. The aperture angle of each sub-beam, α , is determined by the size of the beamlet in the microlens, d , and the distance between the microlens and the collimator lens, m , as d/m . By adjusting the d and m , the aperture angle α can be made substantially larger than the chromatic dispersion $\Delta\beta$. Moreover, the geometrical off-axial aberrations due to the collimator lens is also reduced, because the electrons within a sub-beamlet arrive at the same off-axial position and the difference of the refraction angle error $\Delta\delta$ within a sub-beam is smaller. These focused spots at the collimator lens serve as the secondary source images, and will be imaged by the reduction optics. The resolution of this multibeam

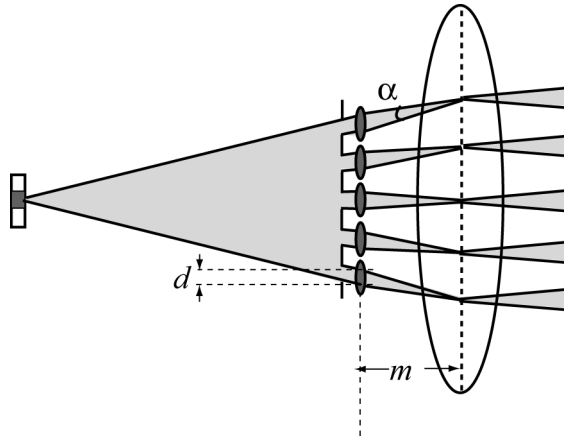


Figure 1-11: The multibeam system proposed by Kruit [1.63].

source, however, now depends on the axial and off-axial aberrations of the microlenses.

Let's first analyse the axial aberrations of electrostatic lenses. The chromatic aberration coefficient of electrostatic lenses is roughly twice the focal length and independent of the lens geometry. On the other hand, the spherical aberration coefficient increases drastically with decreasing the lens diameter. In multibeam sources, the diameter of the microlenses is usually from tens of microns to hundreds of microns, which is at least an order of magnitude smaller than that of the conventional electron lens. Therefore, the spherical aberration coefficient of the microlenses is much larger. The spherical aberrations of the macrolens (if it exists in the multibeam source) can be neglected with respect to that of the microlenses. Special effort should be devoted to reduce the spherical aberration coefficient of the microlenses: different lens types, geometries and operation modes should be investigated in order to find the configuration with minimal spherical aberration coefficient. For the outer microlenses, the electron source is not on the optical axes, and large off-axial aberrations may occur. Therefore, decreasing the aberration of the microlens array is essential for this concept.

Similar to the single column two-lens system, the maximum current that a multibeam system can deliver at wafer is strongly dependent on the aberrations of the multibeam source. For a multibeam source similar to

that drawn in Figure 1-11, the total transmitted current is equal to the product of the beamlet current and the number of beams. Assuming uniform angular current density in the broad beam, the total transmitted current can be expressed as:

$$\begin{aligned}
 I &= N \times I_{beam} = c \times \left(\frac{2\alpha l}{p_l} \right)^2 \times j\pi \left(\frac{d_b}{2l} \right)^2 = cj\pi\alpha^2 \left(\frac{d_b}{p_l} \right)^2 \\
 &= cj\pi\alpha^2 \left(\frac{d_b}{d_l} \right)^2 \left(\frac{d_l}{p_l} \right)^2 = cj\pi\alpha^2 FF^2 \left(\frac{d_l}{p_l} \right)^2
 \end{aligned} \tag{1-16}$$

where j is the angular current density, c is a coefficient related to the geometrical arrangement of the microlenses, α is the useful half emission angle of the electron source, l is the distance between the electron source and the microlens array, p_l is the lens pitch, d_l is the diameter of the microlenses, and d_b is the diameter of the electron beam in the microlens plan, as illustrated in Figure 1-12. The filling factor, FF , is the ratio between the beam diameter in the lens plane and the lens diameter.

As indicated by Eq.(1-16), the total transmitted current is proportional to the geometrical coefficient c , the useful emission current of the electron source ($j\pi\alpha^2$), the second power of the filling factor FF , and the second power of d_l/p_l . Adjusting the microlens arrangement may give marginal increase of the geometrical coefficient c , e.g., the c of a hexagonal pattern is around 16% larger than that of a square pattern. The useful emission current is dependent on the angular current density, the uniformity of the angular current density, and the off-axial aberrations. Schottky emitters with high extraction voltage have high angular current density, but the maximal j is restricted by its uniformity, as explained in the previous section. Low off-axial aberrations permit more current to be used by accepting rays with larger inclination angle. Thus microlenses with low off-axial aberrations helps to increase the total current on the wafer. The ratio of d_l/p_l is limited by the robustness of the lens electrode, which must be rigid enough to avoid electrostatic bending. Improving the filling factor of the microlenses may increase the total transmitted current. The filling factor for a conventional electron lens is around 10% due to aberrations. Reducing the aberrations of the microlenses allows a larger aperture angle or half opening angle at the source, thus a higher

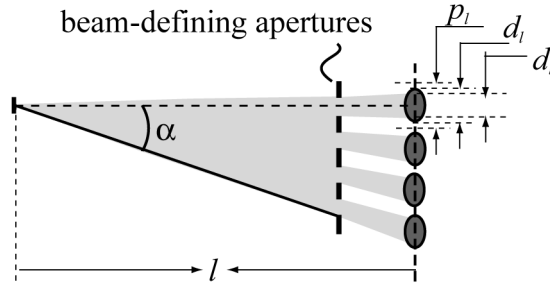


Figure 1-12: The beam-defining aperture, beam diameter at the lens plane, lens diameter and lens pitch.

filling factor and total transmitted current. For example, for spherical aberration dominated probes, lowering the spherical aberration coefficient by a factor of 2 allows a rise of $2^{1/3}$ of the filling factor with the same spherical FW50 disk, and thus the probe current can be increased by a factor of $2^{2/3}$.

To conclude, minimizing the axial and off-axial aberrations of the microlenses in the multi-electron-beam source is very important for the high resolution and high throughput applications.

1.2.3 Reduction of Crosstalk, Charging and Contamination

Besides the low aberration microlens array, the blanker array is the other key component in the multi-electron-beam source. The blanker array should be individually addressed with high speed and low crosstalk, and it should not be subjected to charging and contamination. Various blanker arrays are fabricated using MEMS technology, and successfully demonstrated individual on/off switching. In general, the blanking is due to the existence of an electric field between two opposite electrodes. The field, however, is not exclusively between these two electrodes; it extends to all other electrodes and surfaces on the chip. It is clear from Figure 1-13.a that the fringing field causes angular errors on the neighbour beam. These simulated results agree fairly well with the experimental data and up to 15% crosstalk has been observed. Crosstalk changes the angle of adjacent beams, causing position displacements at the beam stop aperture (causing partial blanking of unblanked beams); at

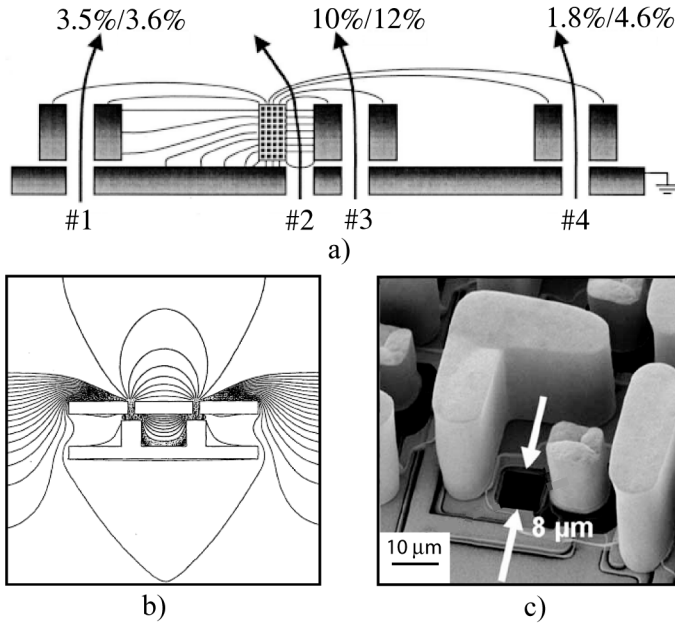


Figure 1-13: a) The model vs. experimental of the crosstalk due to fringing fields (model result%/experimental data%) (from [1.39]); b) the simulation results of electrostatic interference from adjacent blankers with a guard wall attached to the ground electrode (from [1.36]); and c) SEM micrograph of the electroplated AU electrodes (from [1.43]).

the lens (causing addition aberrations); and the most deteriorating, on the wafer. Therefore, the main challenge for the blanker array is to minimize crosstalk. The fringing field can be reduced by adding guard walls connected to the ground electrode, as shown in the top view plot in Figure 1-13.b, where the fringing field extending from the sidewalls of the active electrode is effectively suppressed. Blankers with high height-to-gap aspect ratio, guard walls or a ground cap wafer have smaller crosstalk. Furthermore, crosstalk can be reduced by replacing the monopolar blankers with bipolar blankers because the excitation on each blanker plate is reduced by a factor of two [1.39].

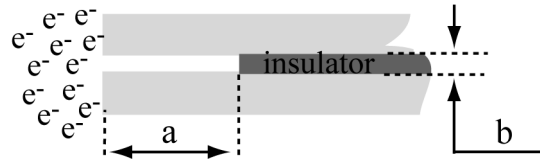


Figure 1-14: The beam-defining aperture, beam diameter at the lens plane, lens diameter and lens pitch.

Recently, Eder-Kapl *et al.*, [1.43] have recorded less than 1% crosstalk in a blanker array as shown in Figure 1-13.c. The extreme low crosstalk can only be explained by the suppression of the fringing field both from the sidewalls and top surface of the active electrodes. This is achieved by the height difference between the active electrodes and the ground electrodes, as indicated in the SEM micrograph.

The inferior effects of the crosstalk can also be relieved by arranging the blanker array in a conjugate plane of the source [1.40, 1.44, 1.45]. In this case, a lens array is necessary to focus the multiple beams at the blanker array. The beam positions on the wafer are the projection of the conjugate source image and thus are not affected by the crosstalk. In addition, the deflection aberration is less for conjugate blanking. Heating of the beam stopping aperture may be attenuated by deflecting the beams over individual apertures rather than over a common aperture [1.38, 1.43].

Besides the low crosstalk requirement, contamination and charging should be prevented at all times to avoid long-term position drift, transient position errors and blanking errors. Contamination is due to surface migration of hydrocarbon molecules to the irradiated region. Surface charges can develop from the contamination layers and result in micro-discharges. The blanking electrodes and the opening aperture between the electrodes are in the close vicinity of the beam, and must be free from direct illumination. Usually the charging of dielectric materials can be reduced by a suitable geometric design. The rule of thumb is the distance between the insulator and the beam (a) at least three times of the insulator gap (b), as shown in Figure 1-14.

In summary, the challenge of the blanker array is realizing low crosstalk and free of charging and contamination at the same time. The design should be also compatible to microfabrication processes.

1.2.4 Conclusion:

To design a multi-electron-beam source for high-resolution high-throughput maskless lithography or inspection, the requirements or the challenges include: the off-axial performance of the Schottky emitter should be the same as that of the axial performance; the aberrations of all the optical components in the multibeam source should be minimized; and the crosstalk, charging and contamination in the blanker array should be controlled. Besides the above mentioned challenges, we also have strict requirements on the roundness of the lenses, the stability of power supplies and alignment between the optical components.

1.3 Scope of the Thesis

Previous work on multiple beam systems is investigated and analyzed in chapter 1.1. Out of the four categories, the multi-electron-beam source is chosen for further investigation. Even though many designs and experiments already exist, a low-aberration multibeam source has never been realized. The subject of this thesis is to design a low aberration multi-electron-beam source for high resolution applications and future generation maskless lithography. The challenges are discussed in chapter 1.2.

Chapter 2 and chapter 3 focus on designing a multibeam source for the future generation maskless lithography, where the multibeam source units should be arranged in a pitch of 1.5 mm to generate massively parallel electron beams. The requirements are defined and two multibeam source designs are discussed and evaluated. The design in chapter 2 is published in the Journal of Vacuum Science and Technology B. The multibeam source design in chapter 3 is presented at the 7th International Conference on Charged Particle Optics and published in Physics Procedia.

In chapter 4, a multi-electron-beam source is designed for SEM-type systems, where 100 beams are generated from a Schottky emitter. The multiple beams emerge at 30 kV and are compatible with most SEM systems commercially available. The multibeam source, together with the SEM column, is capable of improving the throughput of high resolution applications, such as inspection, electron beam induced deposition or analytical applications. The design is presented at the 51st International Conference on Electron, Ion and Photon Beam Technology and Nanofabrication and published in the Journal of Vacuum Science and Technology B.

Chapter 5 elaborates on the design and fabrication of a blanker array. Efforts are taken to reduce crosstalk, charging and contamination. The work is presented at the 50th International Conference on Electron, Ion and Photon Beam Technology and Nanofabrication and published in the Journal of Vacuum Science and Technology B.

Chapter 6 presents the experimental results of a prototype multibeam source similar to the one discussed in chapter 4. The result is presented at the 52nd International Conference on Electron, Ion, and Photon Beam Technology and Nanofabrication. Finally, chapter 7 summarizes the main innovations and conclusions of this work.

1.4 Project Publications

Patent:

1) Y. Zhang, M. J. Van Bruggen and P. Kruit, A multiple beam charged particle optical system, patent requested by Mapper Lithography B. V., Delft, 25-7-2006, appl. no. US60/833394.

Papers:

1) Yanxia Zhang, M. Van Bruggen, C. T. H. Heerkens, and P. Kruit, Integrated multi-electron-beam blanker array for sub-10 nm electron beam induced deposition, presented in EIPBN 2006 Baltimore, J. Vac. Sci. Technol. B 24(6), 2857 (2006).

- 2) Yanxia Zhang and P. Kruit, Design of a high brightness multi-electron beam source, presented in CPO-7 Cambridge, Physics Procedia 1, 553 (2008).
- 3) Yanxia Zhang and P. Kruit, High Brightness 100-electron-beam source for high-resolution applications, presented in EIPBN 2007 Denver, J. Vac. Sci. Technol. B 25(6), 2239 (2007).
- 4) Yanxia Zhang, J. E. Barth, and P. Kruit, Electron optics of micro-lenses with Inclined beams, J. Vac. Sci. Technol. B 26(2), 655 (2008).
- 5) B. van Someren, M. J. Van Bruggen, Y. Zhang, C. W. Hagen and P. Kruit, Multibeam electron source using MEMS electron optical components, J. Phys.: *Conf. Ser.* 34, 1092 (2006).
- 6) A. K. Dokania, J. F. M. Velthuis, Yanxia Zhang, and Pieter Kruit, Thermal model of miniaturized Schottky emitter for parallel electron beam lithography, J. Vac. Sci. Technol. B 25(2), 504 (2007).

Reference

- [1.1] H. C. Pfeiffer, J. Vac. Sci. Technol. 15, 887 (1978).
- [1.2] Y. Nakayama, S. Okazaki, N. Saitou and H. Wakabayashi, J. Vac. Sci. Technol. B 8, 1836 (1990).
- [1.3] S. D. Berger, and J. M. Gibson, Appl. Phys. lett. 57 (2), 153 (1990).
- [1.4] R. S. Dhaliwal *et al.*, Advan. Semicon. Litho. 45 (5), 615 (2001).
- [1.5] T. W. O’Keeffe and R. M. Handy, IEDM, 148 (1967).

- [1.6] T. H. Chang, D. P. Kern, and L. P. Muray, J. Vac. Sci. Technol. B 10(6), 2743 (1992).
- [1.7] L. P. Muray *et al.*, J. Vac. Sci. Technol. B 18(6), 3099 (2000).
- [1.8] C. S. Silver, J. P. Spallas, and L. P. Muray, J. Vac. Sci. Technol. B 25(6), 2258 (2007).
- [1.9] T. Haraguchi *et al.*, J. Vac. sci. Technol. B 20(6), 2726 (2002).
- [1.10] T. Haraguchi *et al.*, J. Vac. Sci. Technol. B 22(3), 985 (2004).
- [1.11] T. R. Groves, and R. A. Kendall, J. Vac. Sci. Technol. B 16(6), 3168 (1998).
- [1.12] D. S. Pickard, C. Campbell, T. Crane, L. J. Cruz-Rivera, A. Davenport, W. D. Meisburger, and R. F. W. Pease, J. Vac. Sci. Technol. B 20(6), 2662 (2002).
- [1.13] D. S. Pickard, T. R. Groves, W. D. Meisburger, T. Crane, and R. Fabian Pease, J. Vac. Sci. Technol. B 21(6), 2834 (2003).
- [1.14] D. S. Pickard, C. Kenney, S. Tanimoto, T. Crane, T. Groves, and R. F. W. Pease, J. Vac. Sci. Technol. B 25(6), 2277 (2007).
- [1.15] R. F. Pease, Microelec. Engi. 78-79, 381 (2005).
- [1.16] L. R. Baylor *et al.*, J. Vac. Sci. Technol. B 20(6), 2646 (2002).
- [1.17] L. R. Baylor *et al.*, J. Vac. Sci. Technol. B 22(6), 3021 (2004).
- [1.18] J. E. Schneider, A. W. Baum, G. I. Winograd, R. F. W. Pease, M. McCord, and W. E. Spicer, J. Vac. Sci. Technol. B 14(6), 3782 (1996).

- [1.19]A. W. Baum, J. E. Schneider, R. F. W. Pease, M. A. McCord, W. E. Spicer, K. A. Costello, and V. W. Aebi, J. Vac. Sci. Technol. B 15(6), 2707, (1997).
- [1.20]P. Arcuni, S. Presley, V. Aebi, and W. E. Spicer, J. Vac. Sci. Technol. B 19(6), 2585 (2001).
- [1.21]F. Machuca, Z. Liu, J. R. Maldonado, S. T. Coyle, P. Pianetta, and R. F. W. Pease, J. Vac. Sci. Technol. B 22(6), 3565 (2004).
- [1.22]Z. Liu, Y. Sun, P. Pianetta, and R. F. W. Pease, J. Vac. Sci. Technol. B 23(6), 2758 (2005).
- [1.23]M. W. Geis, S. Deneaul, K. E. Krohn, M. Marcant, T. M. Lyszczarz, and D. L. Cooke, Appl. Phys. Lett. 87, 192115 (2005).
- [1.24]M. Mankos *et al.*, J. Vac. Sci. Technol. B 18(6), 3010 (2000).
- [1.25]M. Mankos, A. Sagle, S. T. Coyle, and A. Fernandez, J. Vac. Sci. Technol. B 19(6), 2566 (2001).
- [1.26]M. Mankos, S. Coyle, A. Fernandez, A. Sagle, W. Owens, J. Sullivan, and T. H. P. Chang, J. Vac. Sci. Technol. B 19(2), 467 (2001).
- [1.27]M. L. Yu, S. T. Coyle, W. Devore, and B. Shamoun, J. Vac. Sci. Technol. B 23(6), 2589 (2006).
- [1.28]E. Yin, A. D. Brodie, F. C. Tsai, G. X. Guo, and N. W. Parker, J. Vac. Sci. Technol. B 18(6), 3126 (2000).
- [1.29]W. Barth *et al.*, J. Vac. Sci. Technol. B 18(6), 3544 (2000).
- [1.30]D. K. Schroder, R. N. Thomas, J. Vine, and H. C. Nathanson, IEEE Trans. Elec. Dev. 21, 785 (1974).

- [1.31]M. J. Wieland, B. J. Kampherbeek, P. Addressi, and P. Kruit, *Microelec. Engi.* 57-58, 155 (2001).
- [1.32]A. van Zuuk, C. T. H. Heerkens, A. H. V. van Veen, T. F. Teepen, M. J. Wieland, O. Groening, and P. Kruit, *Microelec. Engi.* 73-74, 106 (2004).
- [1.33]T. F. Teepen, A. H. V. van Veen, H. van't Spijker, S. W. H. K. Steenbrink, A. van Zuuk, C. T. H. Heerkens, and M. J. Wieland, *J. Vac. Sci. Technol. B* 23(2), 359 (2005).
- [1.34]T. H. Newman, R. F. W. Pease, and W. DeVore, *J. Vac. Sci. Technol. B* 1(4), 999 (1983).
- [1.35]G. W. Jones, S. K. Jones, M. D. Walters, and B. W. Dudley, *IEEE Trans. Elec. Dev.* 36, 2686 (1989).
- [1.36]H. Yasuda *et al.*, *Jpn. J. Appl. Phys.* 32, 6012 (1993).
- [1.37]H. Yasuda *et al.*, *J. Vac. Sci. Technol. B* 14(6), 3813 (1996).
- [1.38]I. L. Berry, A. A. Mondelli, J. Nichols, and J. Melngailis, *J. Vac. Sci. Technol. B* 15(6), 2382 (1997).
- [1.39]G. Winograd, V. Krishnamurthi, R. Garcia, L. H. Veneklasen, M. Mankos, and F. Pease, *J. Vac. Sci. Technol. B* 18(6), 3052 (2000).
- [1.40]M. Muraki, and S. Gotoh, *J. Vac. Sci. Technol. B* 18(6), 3061 (2000).
- [1.41]M. Nakasuji, S. Yoshikawa, T. Satake, and N. Noji, *Jpn. J. Appl. Phys.* 44, 5570 (2005).
- [1.42]M. J. Van Bruggen, B. van Someren, and P. Kruit, *J. Vac. Sci. Technol. B* 23(6), 2833 (2005).

- [1.43]S. Eder-Kapl *et al.*, Microelec. Engi. 83, 968 (2006).
- [1.44]S. Taminoto *et al.*, J. Vac. Sci. Technol. B 25 (2), 380 (2007).
- [1.45]O. Kamimura *et al.*, J. Vac. Sci. Technol. B 25(1), 140 (2007).
- [1.46]A. J. van den Brom, A. H. V. van Veen, W. M. Weeda, G. Z. M. Berglund, M. Wieland, and P. Kruit, J. Vac. Sci. Technol. B 25(6), 2245 (2007).
- [1.47]P. Kruit, Microelec. Engi., 84, 1027 (2007).
- [1.48]E. Slot *et al.*, Proc. of SPIE, Vol. 6921 (2008).
- [1.49]J. Orloff, *Handbook of Charged Particle Optics*, Chapter 2, CRC Press (1997).
- [1.50]<http://www.yps-ltd.com/images/schottkytip.jpg>
- [1.51]D. W. Tuggle and L. W. Swanson, J. Vac. Sci. Technol. B 3(1), 220 (1984).
- [1.52]N. Samoto, R. Shimizu, H. Hashimoto, N. Tamura, K. Gamo, and S. Namba, Jpn. J. Appl. Phys., 24, 766 (1985).
- [1.53]M. T. Otten, Proc. ICEM-13, 235 (1994).
- [1.54]M. Franssen, Ph. D Dissertation, *Towards High-brightness, Monochromatic Electron Sources* (1999).
- [1.55]A. H. V. van Veen, C. W. Hagen, J. E. Barth, and P. Kruit, J. Vac. Sci. Technol. B 19(6), 2038 (2001).
- [1.56]M. S. Bronsgeest, J. E. Barth, L. W. Swanson, and P. Kruit, J. Vac. Sci. Technol. B 26(3), 949 (2008).

- [1.57]S. Fujita and H. Shimoyama, J. Electron. Microsc. 54(5), 413 (2005).
- [1.58]M. S. Bronsgeest, J. E. Barth, G. A. Schwind, L. W. Swanson, and P. Kruit, J. Vac. Sci. Technol. B 25(6), 2049 (2007).
- [1.59]M. Van Bruggen, Ph. D Dissertation, *Multi-electron Beam System for High Resolution Electron Beam Induced Deposition* (2008).
- [1.60]J. E. Barth, and P. Kruit, Optik, 101(3), 101 (1996).
- [1.61]P. Kruit, M. Bezuijen and J. E. Barth, J. Appl. Phys. 99, 024315 (2006).
- [1.62]G. H. Jansen, *Coulmb Interations in Particle Beams*, Advances in Electronics and Electron Physics, Supplement 21, Academic Press, (1990).
- [1.63]P. Kruit, *Apparatus for Generating a Plurality of Beamlets*, Patent No. US 7129502 B2 (2006).

Chapter 2

Electron Optics of Microlenses with Inclined Beams

Journal of Vacuum Science and Technology B 26(2), 655 (2008).

Abstract

For multi-electron beam systems with a single electron source, the outside beams need to be collimated before entering the individual micro columns. As an alternative of the traditional multibeam source design where the broad beam from the source is collimated by a single lens, the broad beam can be first split in sub-beams that are focused by a microlens array and subsequently collimated by a deflector array. This configuration avoids the large angular error due to spherical and chromatic aberration of the collimator lens. The electron optics of the microlenses that are focusing skewed beams is investigated for different lens types and geometries. A 2-electrode immersion microlens array with offset apertures is a good candidate due to its small off-axial aberrations. A 100-beam source unit, comprising a Schottky emitter, an immersion microlens array and deflector array, is capable of generating 100 parallel beamlets with beamlet current of 2 nA.

2.1 Introduction

The technology of Micro-electro-mechanical systems (MEMS) offers the possibility of making micro-sized electrostatic lenses, deflectors, blankers, and multi-poles [2.1]. A single-beam miniature electron column is capable of writing sub-100 nm patterns and resolving less than 35 nm features [2.2]. By arraying such miniature columns [2.3-2.7] or stacking micro-sized optical component arrays [2.8-2.12] to create plural focused and individually-controlled beams, the total current delivered to the wafers can be increased without suffering from source brightness limitation and Coulomb interactions. Multibeam systems with stacked optical component arrays are good candidates for maskless lithography where thousands of beams are necessary to meet the throughput requirements.

In multibeam systems with stacked optical arrays, the broad beam is usually collimated, subsequently split into multiple beams by an aperture array, focused by a microlens array, and controlled via a blanker array located at the conjugate plane. For high resolution applications, the size of the lens array or the throughput is limited by the off-axial aberrations of the collimator lens [2.13]. Alternatively, the broad beam may impinge on an aperture array and lens array obliquely, and the beamlets are collimated by a deflector array at the conjugate plane. This configuration provides a solution of avoiding the angular error due to spherical and chromatic aberrations of a collimator lens [2.14]: by focusing each beamlet at the deflector array, the opening angle in the beam can be made substantially larger than the chromatic angular error; and the spherical angular error in the collimator lens is eliminated by collimating using the deflector array.

The off-axial aberrations of the lens array with skewed incidence can be minimized through the use of offset current limiting apertures. This was first proposed by Kurihara [2.15] for an einzel lens matrix with skewed incidence, where field curvature is corrected by changing the focus using a correction lens array. However, the beamlet incident angle is restricted to 30 mrad due to astigmatism and the throughput is limited by the number of beamlets. The alignment between the einzel lens array,

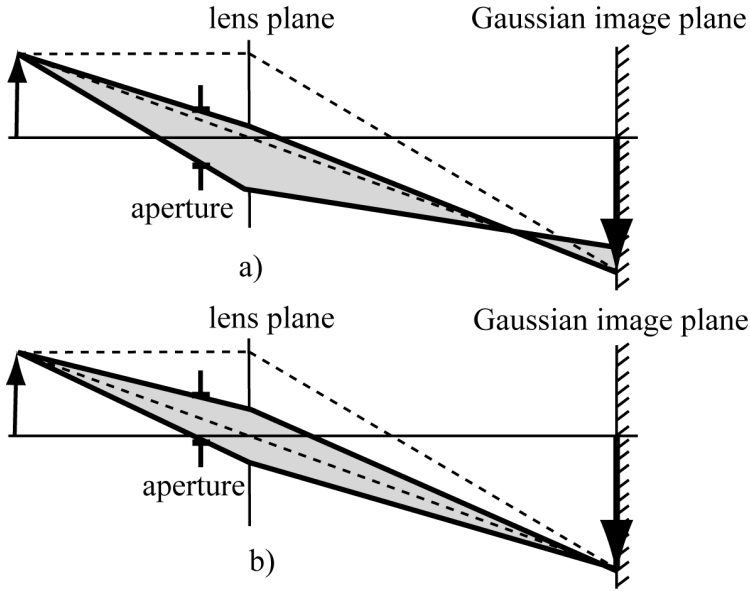


Figure 2-1: Off-axial aberrations with a) an aperture on the axis, b) an offset aperture such that the “virtual aperture” is centered in the lens plane.

aperture array and the correction lens array raises serious engineering challenges.

In this work, the electron optics of microlenses with skewed incidence is investigated for different lens types and geometries. It shows that a 2-electrode immersion microlens array is a good candidate for generating multiple probes with small off-axial aberrations. A multibeam source is designed, where the aperture array is integrated with the microlens array and the field curvature is corrected by adjusting the diameters of the outer lenses. The performance of the multibeam source is evaluated.

2.2 Method of Analysis

The typical dimension of microlenses are around 50-150 μm for a beam voltage of 1-5 kV. For a 10-by-10 microlens array with skewed

incidence, the off-axial distance for the outermost lens is more than 0.25 mm and the off-axial aberrations deteriorate the images of outer lenses. The off-axial aberrations, however, can be reduced by offsetting the current limiting aperture from the axis (Figure 2-1.a) such that the “virtual aperture” is centered in the lens plane (Figure 2-1.b). For electrostatic lenses where a lens-plane aperture interrupts the lens field, the aperture should be in a field-free region.

The off-axial aberrations can be evaluated by deviations from the paraxial trajectory in the Gaussian image plane. The third order radial deviations can be calculated using formulas in Table 2-1, where S_A , K_A , F_A , A_A , D_A , X_A^* and T_A^* are aperture-dependent aberration coefficients, and α_a and β_o are the complex slope and complex coordinate in the object plane [2.16, 2.17]. The aberration coefficients are obtained from a 2D finite element method program - Electrostatic Lens Design (ELD) [2.18]. The radius of the total blur is roughly estimated by the square root square sum of the deviations.

The plane of best focus in general does not coincide exactly with the Gaussian image plane. By taking into account only the spherical aberration, for example, the disk of least confusion is only one-fourth as large as the circle of confusion in the Gaussian image plane. In the world of analytical microscopy and lithography, people use the FW50 disk (the minimum spot diameter containing 50% probe current) for probe size

TABLE 2-1:Radial deviations from the paraxial trajectory in the Gaussian image plane for optical systems with apertures.

Geometric aberrations	Spherical	$M \cdot S_A \alpha_a^2 \bar{\alpha}_a$
	Coma	$M \cdot K_A \alpha_a \beta_o \bar{\alpha}_a$
	Field curvature	$M \cdot F_A \alpha_a \beta_o \bar{\beta}_o$
	Astigmatism	$M \cdot A_A \beta_o^2 \bar{\alpha}_a$
	Distortion	$M \cdot D_A \beta_o^2 \bar{\beta}_o$
Chromatic aberrations	Axial	$M \cdot X_A^* \alpha_a \Delta V / V$
	Transverse	$M \cdot T_A^* \beta_o \Delta V / V$

characterization: the spherical FW50 disk is only 9% of the circle of confusion in the Gaussian image plane [2.19]. As the microlens array may be used for applications in lithography or inspection, it is important to evaluate the FW50 blur. A finite difference method program, SIMION, is used for this purpose: 500 electrons emitted from an infinitely small spot with pseudo-random angular distribution and zero energy spread are traced through the microlenses; positions and angles of each electron are recorded and input into MATLAB, where through focus series are produced and the FW50 blur is determined.

2.3 Aberrations-minimized Microlens Array

The aberrations for an electrostatic lens are dependent on lens type, geometry and the aperture position. Computer models of an einzel lens array and a two-electrode immersion lens array are compared at the image side, with the same potential, focal length, magnification and half opening angle. The immersion lens or einzel lens is composed of two / three 400 μm thick electrodes with a 400 μm separation, and the lens radii are 200 μm . The potentials of the electrodes are determined such that both lenses have the same focal length at the image side. The object plane is chosen to have the same magnification. The half opening angle is chosen such that the beam is around 10% of the lens diameter, which is

TABLE 2-2: The optical properties of the axial einzel lens and the 2-electrode immersion lens.

Potential at object side (V)	8000	4000
Potential at image side (V)	8000	8000
Potential at middle electrode (V)	5067	N.A.
Focal length at image side (mm)	8.72	8.72
Magnification	-5.0	-5.0
Angular Magnification	-0.20	-0.14
Half opening angle image side (mrad)	0.38	0.38
Spherical FW50 (nm)	65.0	71.5
Chromatic FW50 (nm)	6.3	8.4

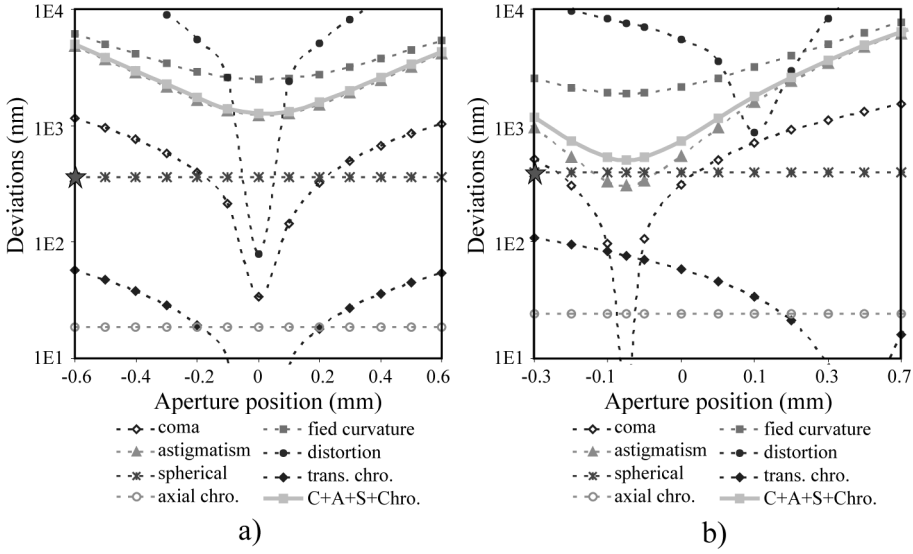


Figure 2-2: The deviations and total blur in the Gaussian image plane for a) an outer einzel lens at an off-axial distance of 1 mm; b) an outer 2-electrode immersion lens at an off-axial distance of 1 mm.

usually the maximum filling for conventional lenses. The optical properties for the axial lenses are listed in Table 2-2. Note that the spherical and chromatic FW50 disks are different from their deviations in the Gaussian image plane.

The aperture-dependent aberration coefficients of the lenses are obtained in ELD. The deviations in the Gaussian image plane are calculated using formula in Table 2-1 for an outer lens with an off-axial distance of 1 mm (equal to an incident angle of 115 mrad). The deviations are plotted in Figure 2-2 as a function of the z-position of the “virtual aperture”, with the origin located at the geometrical centre of the lenses. The axial blur is indicated by a star on the y-axis. The total blur (C+A+S+Chro) is estimated as square root square sum of coma, astigmatism, spherical and chromatic aberration. Field curvature can be compensated by adjusting the lens diameters as will be explained in the next paragraph. Even though having similar axial aberrations, it is clear

in Figure 2-2 that the off-axial aberrations of the immersion lens are much smaller than that of the einzel lens: the total blur is 1268 nm for the outer einzel lens and 506 nm for the outer immersion lens. For the immersion lens, a 50 μm shift from the optimum aperture position, which, with an incident angle of 115 mrad corresponds to a misalignment of 5.75 μm between the aperture and lens, gives a rise to about 25 nm in the total blur.

The immersion microlenses can be modelled by two coaxial cylinders with equal diameters and separated by a small distance. Numerical calculations show that for a given ratio of electrode potentials, the focal length becomes larger by increasing the lens diameter [2.20]. Therefore, it is possible to correct field curvature by enlarging the diameter of the outer lenses. With offset apertures and the field curvature correction technique, a large-sized multibeam system may be made with the immersion microlens array.

2.4 Micro lens Array in Multibeam Systems

The microlens array with skewed incidence may be used in multibeam systems to improve the throughput by delivering more current than a single beam system. The total current transmitted through the microlens array can be expressed as:

$$I = N \times I_{beam} = cj\pi\alpha^2 FF^2 \left(\frac{d_l}{p_l} \right)^2 \quad (2-1)$$

α is the electron source half emission angle, within which the angular current density j is uniform. These two parameters are determined by the type of electron sources and the source operation conditions. High brightness Schottky sources are preferred in lithography and microscopy systems which demand both high resolution and high current density. Schottky sources and their operation conditions will not be discussed in this paper, but more details can be found in ref. [2.21]. c is a coefficient related to the geometric arrangement of microlenses; d_l/p_l is the ratio of lens diameter and lens pitch, which is limited around 0.8 to maintain

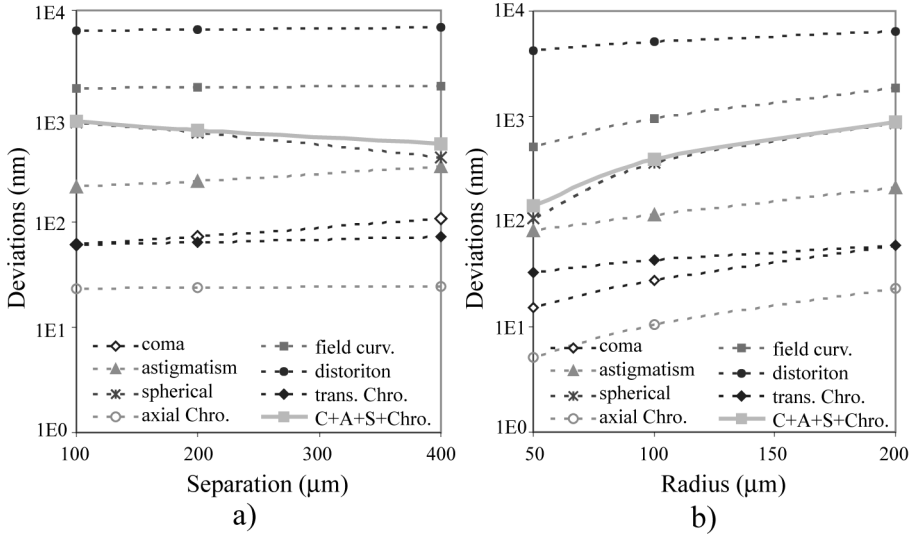


Figure 2-3: The relationship of the lens geometry and deviations of the outermost lens in the microlens array, when keeping the focal length, magnification, filling factor and the total current the same: a) deviations as a function of lens electrode separation (lens radius equals to 200 μm); b) deviations as a function of lens radius (lens separation equals to 100 μm).

enough physical strength of the lens electrodes and prevent electrostatic bending. FF is the filling factor defined as the ratio of beam diameter in the lens plane and the lens diameter. The maximal filling factor of a conventional lens is around 10% and obtained when the FW50 blur (due to Coulomb interactions and aberrations) reaches the geometrical spot size. In multibeam systems, effects of Coulomb interactions are greatly reduced by splitting the broad beam into beamlets. In order to have a large total current, the aberrations of the microlenses should be minimized to allow for a large filling factor.

The aberrations of the microlenses are investigated for different lens geometries. The comparison is carried out under the condition that the

total current transmitted through the microlens arrays is equal. Assuming identical source parameters (angular current density and useful source half emission angle) and d_l/p_l , the filling factor should be the same. The outermost lenses in the microlens arrays, for which the incident angles are 115 mrad, are compared at the same focal length, magnification, and beam potential at the image side.

First, the deviations in the Gaussian image plane are plotted in Figure 2-3.a for different electrode separations, while the lens radius is fixed at 200 μm . The total deviation increases from 536 nm to 894 nm by changing the electrode separation from 400 μm to 100 μm , with decreasing astigmatism and coma, and increasing spherical deviation. The total blur, when keeping the separation at 100 μm , however, decreases to 141 nm by choosing a lens radius of 50 μm , as shown in Figure 2-3.b. This seems counter-intuitive since the lens aberrations of each lens increase with decreasing radius, but the reader is reminded here that the filling factor is kept constant and that the total number of lenses is increased. A smaller total blur then allows a larger filling factor (or an opening angle) until the FW50 blur reaches about half the geometrical spot size. The advantages are a larger total current and a spherical aberration-dominated blur, which is preferred in terms of spot size uniformity. (Spherical aberration is proportional to the cube of the opening angle and increases faster than other aberrations)

For a microlens array to be used in multibeam systems, the lens pitch is tens of microns in order to put the probes at a typical pitch of 150 μm . The current per beamlet is around several nano-amperes. The electrode separation is a trade-off between the spherical aberration, astigmatism and practical implementation. As an example, one particular multibeam source system is designed and the performance is evaluated.

2.4.1 The Configuration of the Multibeam Source

The multibeam source is designed to generate 100 parallel beamlets and the configuration is shown in Figure 2-4. The broad beam emitted from the Schottky emitter is split by an aperture array and beamlets are projected by the microlens array at the center of the deflector electrodes. Subsequently, the beamlets are collimated by applying a voltage

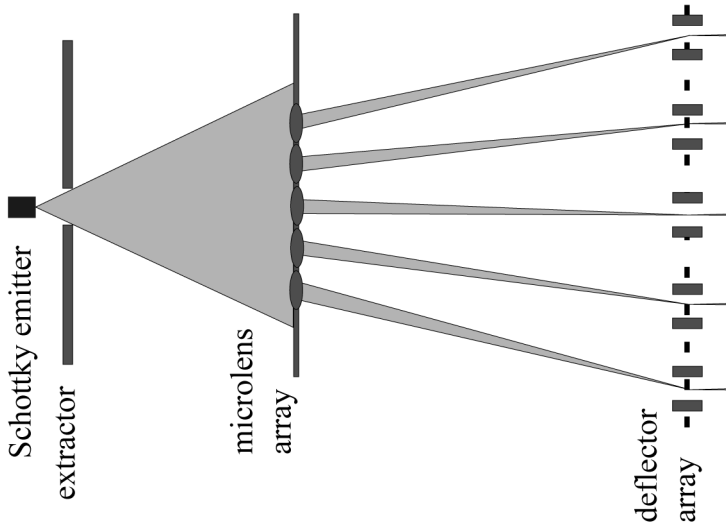


Figure 2-4: The configuration of the multibeam source.

proportional to the landing angles at the deflector array. To reduce the deflection voltage for the outer beams, the extraction voltage is set at 1 kV. The distance between the tip and the extractor is adjusted to have sufficient field near the tip. Furthermore, a deceleration microlens is used to restrict the deflection voltage below 15 volts. The 100-beam source unit should be able to work either as a single unit or arranged in an array to generate massive parallel beamlets for maskless lithography [2.22, 2.23].

The distance between the tip and the aperture array, where most of the trajectory displacement occurs, is set to 2.7 mm. The microlenses are arranged hexagonally with a pitch of 50 μm . The lens configuration and equipotential lines are illustrated in Figure 2-5. As shown, the lens field is locally limited in the bore, thus the current limiting aperture can be integrated on the first electrode and sit in a field free region. The integration improves the alignment between the lens array and aperture array by aligning with a mask aligner, which has typical sub-micron alignment accuracy.

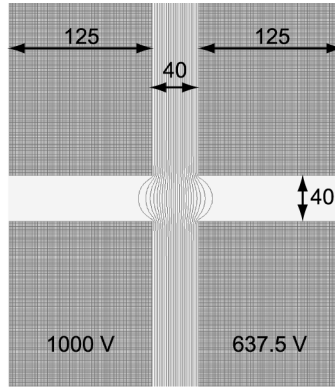


Figure 2-5: a) The geometry (unit: micron), potential and equipotential lines of the 2-electrode immersion lens with integrated current limiting aperture in a field free region.

2.4.2 Multibeam Source Performance

The optical properties of the axial microlens are listed in Table 2-3. The microlens array projects multiple source images in a pitch of around

TABLE 2-3: The image side optical properties of the axial microlens.

Objective distance	2.7 mm
Image distance	4.8 mm
Magnification	-2.0
Angular magnification	-0.63
Focal length	1.55 mm
Geometrical spot size	100 nm
Spherical coefficient	1.74E5 mm
Axial chromatic coefficient	2.1E1 mm
Half opening angle	1.16 mrad
Spherical FW50	49.1 nm
Chromatic FW50	6.7 nm
Filling factor	25%

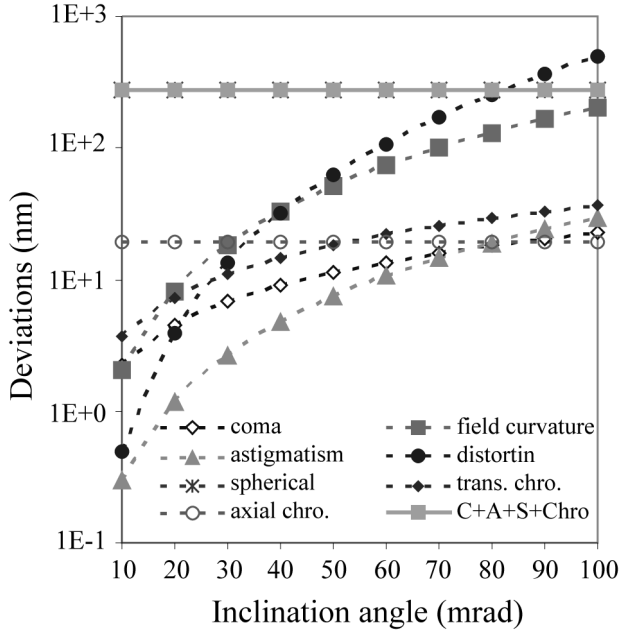


Figure 2-6: The deviations and total blur as a function of incident angle on the microlens array.

140 μm . The filling factor is limited to 25% by the spherical FW50 disk. Assuming the low-extraction-voltage Schottky emitter having a brightness of $10^8 \text{ A/m}^2\text{srV}$, a virtual source size of 50 nm and an angular current density of 200 $\mu\text{A/sr}$, then the current per beamlet is 2.15 nA, and the total current at wafer is 215 nA.

The deviations in the Gaussian image plane are plotted in Figure 2-6, as a function of the incident angle on the microlens array. The total blur is dominated by the spherical aberration.

The geometrical FW50 blur (including spherical aberration, coma and astigmatism) for the outer lenses are determined more precisely using through focus series. The through focus series (100 μm before and after the best focus plane) for the central lens is shown in Figure 2-7.a. The beam profile changes rapidly with image positions and only spherical aberration is present in the probe. The FW50 blur is 54 nm, indicated with a circle in the second image. The slight difference from the theoretic value in Table 2-3 may be due to higher order aberrations in the through

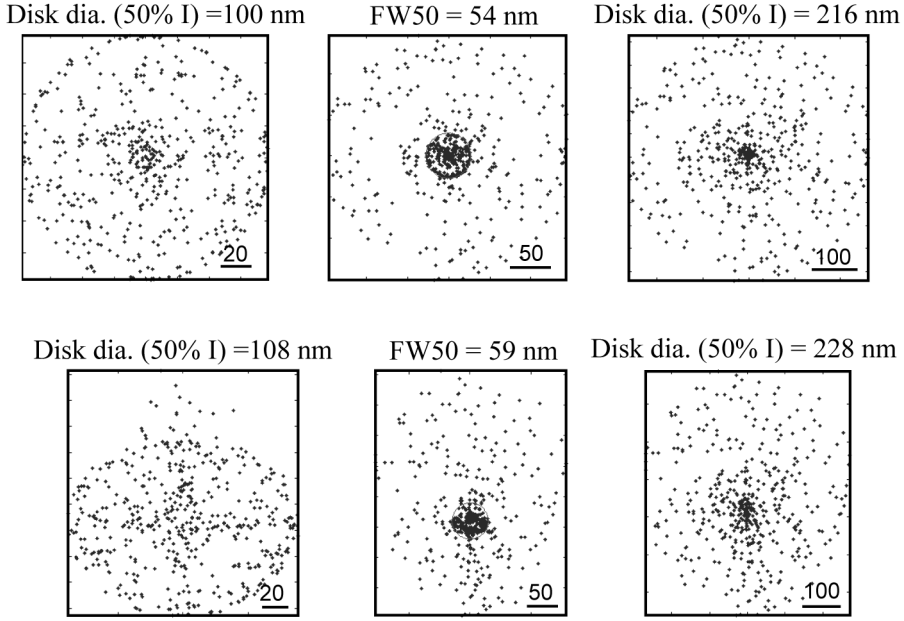


Figure 2-7: The through focus series of the micro-lenses a) axial lens; b) an outer lens with inclination angle of 90 mrad. The FW50 blur is indicated by a circle.

focus series. The geometrical FW50 blur for an outer lens with incident angle of 90 mrad is shown in Figure 2-7.b, where coma and astigmatism are present besides the spherical aberration. The FW50 blur rises to 59 nm.

The total spot size can be obtained using the power root sum (RPS) algorithm [2.19], by adding the spherical aberration dominated FW50 blur (d_{FWs50}) and the geometrical spot size (d_{Geo}) using power = 1.3; the result is then added with the chromatic FW50 blur (d_{FWc50}) using power = 2:

$$d = ((d_{Geo}^{1.3} + d_{FWs50}^{1.3})^{2/1.3} + d_{FWc50}^2)^{1/2} \quad (2-2)$$

where the chromatic FW50 blur is estimated by:

$$d_{FWc50} = 0.34 \times M(X_A^* \frac{VV}{V} \alpha_a + T_A^* \beta_0 \frac{VV}{V}) \quad (2-3)$$

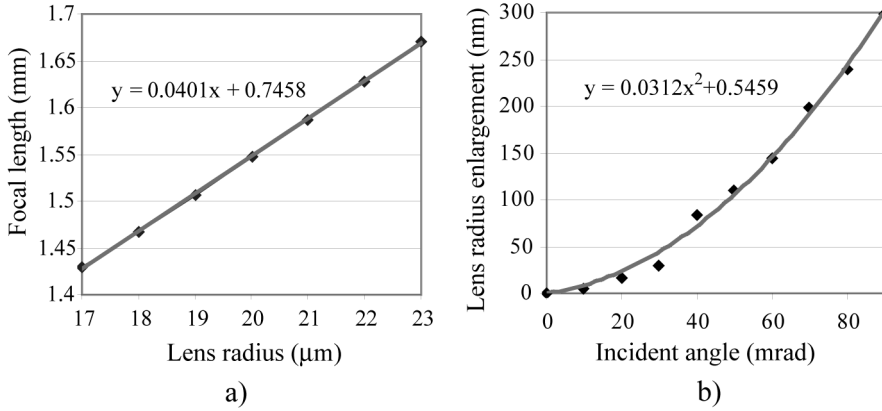


Figure 2-8: The relationship of the focal length and lens radius; b) the radii enlargement for outer lenses for full compensation of field curvature.

The RPS spot size is 133 nm for the central beam, and 138 nm for the outermost beam.

In principle, by adjusting diameters of outer lenses, the field curvature can be fully compensated. The relationship between the focal length and lens radius is shown in Figure 2-8.a. The radius enlargement for outer lenses is calculated and plotted in Figure 2-8.b. Distortion may be avoided by adjusting the position of microlenses. However, in practice, the field curvature and distortion compensation are limited by the lithography resolution and the accuracy of pattern transfer from lithography to dry etching. For the current settings, a 10 nm deviation from the ideal lens diameter gives a blur around 8 nm, and the position error from microfabrication translates by a factor of 2 to probe position error.

2.5 Conclusions

The 2-electrode immersion microlens array presents superior properties for focusing inclined beams when compared to the three-electrode Einzel lens. The total blur is minimized by offsetting the

aperture. Other developments include integrating the aperture array with sub-micron alignment resolution, and correcting field curvature by adjusting diameters of outer lenses. These make the application in multibeam systems possible.

A 100-beam source unit is designed as an example. The design avoids angular errors due to spherical and chromatic aberration of the collimator lens in a traditional multibeam source. The multibeam source is capable of delivering a total current of 215 nA at the wafer with uniform spot sizes.

In some cases, it is possible to use single-electrode microlenses, or aperture-lenses. These turn out to have even smaller aberrations than 2-electrode immersion lenses. An analysis of those systems can be found in reference [2.23] and [2.24].

Reference

- [2.1] P. Kruit, *Microelec. Engi.* 84, 1027, (2007).
- [2.2] L. P. Muray, C. S. Silver, and J. P. Spallas, *J. Vac. Sci. Technol. B* 24, 2945 (2006).
- [2.3] J. P. Spallas, C. S. Silver, and L. P. Muray, *J. Vac. Sci. Technol. B* 24, 2892 (2006).
- [2.4] T. Haraguchi, T. Sakazaki, T. Satoh, M. Nakano, S. Hamaguchi, T. Kiuchi, H. Yabara, and H. Yasuda, *J. Vac. Sci. Technol. B* 22, 985 (2004).
- [2.5] E. Yin, A. D. Brodie, F.C. Tsai, G. X. Guo, and N. W. Parker, *J. Vac. Sci. Technol. B* 18, 3126 (2000).
- [2.6] M. Mankos, S. Coyle, A. Fernandez, A. Sagle, P. Allen, W. Owens, J. Sullivan and T. H. P. Change, *J. Vac. Sci. Technol. B* 18, 3010 (2000).
- [2.7] L. R. Baylor, *et.al*, *J. Vac. Sci. Technol. B* 22, 3021 (2004).

- [2.8] O. Kamimura, *et al.*, J. Vac. Sci. Technol. B 25, 140 (2007).
- [2.9] H. Yasuda, S. Arai, J. Kai, Y. Ooae, T. Abe, S. Maruyama, and T. Kiuchi, J. Vac. Sci. Technol. B 14, 3813 (1996).
- [2.10] M. Muraki and S. Gotoh, J. Vac. Sci. Technol. B 18, 3061 (2000).
- [2.11] Stefan Eder-Kapl, *et al.*, Microelec. Eng. 83, 968 (2006).
- [2.12] M. J. Van Bruggen, B. van Someren, and P. Kruit, J. Vac. Sci. Technol. B 23, 2833 (2005).
- [2.13] S. Tanimoto, *et al.*, J. Vac. Sci. Technol. B 25, 380 (2007).
- [2.14] P. Kruit, Apparatus for Generating a Plurality of Beamlets, publication No. US2007029509.
- [2.15] Kenji Kurihara, J. Vac. Sci. Technol. B 4, 1251 (1986).
- [2.16] B. Lencova and M. Lenc, Optik, 105, No. 3 (1997).
- [2.17] B. Lencova and M. Lenc, Optik, 97, No. 3 (1994).
- [2.18] B. Lencova and G. Wisselink, Electron Optical Design Program Packages ELD 3.7 (2002).
- [2.19] J. E. Barth, P. Kruit, Optik, 101, No. 3 (1996).
- [2.20] V. K. Zworykin, G. a. Morton, E. G. Ramberg, J. Hillier, and A. W. Vance, *Electron Optics and the Electron Microscope*, Wiley & Sons, New York (1945).
- [2.21] J. Orloff, *Handbook of Charged Particle Optics*, CRC, Boca Raton, FL (1997).

[2.22]A. K. Dokania, J. F. M. Velthuis, Yanxia Zhang and Pieter Kruit, J. Vac. Sci. Technol. B 25, 504 (2007).

[2.23]Yanxia Zhang and P. Kruit, Physics Procedia 1, 553 (2008).

[2.24]Yanxia Zhang and P. Kruit, J. Vac. Sci. Technol. B 25, 2239 (2007).

Chapter 3

High Brightness Multi-electron-beam Source for Massively Parallel Electron Beam Lithography

Physics Procedia 1, 553 (2008).

Abstract

An electron optics design is presented for forming 100 high brightness beamlets from a single “Schottky” type “thermal field emission” source, such as used in present day electron microscopes and lithography machines. The footprint of the whole system is only 1.5x1.5 mm, so that it can be used as one element in an array of many elements for application in high throughput maskless lithography or high throughput electron beam inspection. Novel electron optical components are used such as an array of electrostatic aperture lenses with an 85% filling factor and a zero-strength electrostatic decelerating lens. For a source brightness of 10^8 A/m²srV, each beamlet can deliver 15 nA without an increase of the spot diameter by lens aberrations.

3.1 Introduction

In order to increase the throughput of electron beam lithography systems (EBL), several single-source multi-beam systems [3.1-3.4] have been proposed. The difficulty for the single-column systems is that the source provides enough current, but the brightness is too low. To achieve the high throughput of $1\text{cm}^2/\text{s}$ as defined by Pease [3.5], an excessive number of beams are required.

An alternative approach is multi-source multi-beam systems, with one beam per source. In the DEAL concept proposed by Baylor [3.6], an array of vertically aligned carbon nanofibers (VACNF) is used as electron sources. The VACNF has high brightness, but not sufficient stability. Arrayed micro-columns [3.7] with Schottky sources, which are bright and stable, are under development. The throughput, however, is severely limited by the number of columns.

Another approach is multi-source multi-beam systems, with multiple beams per source.

In this paper, we propose a high brightness multi-electron beam source with arrayed Schottky emitters, where the diverging beam emitted from each source is split into 100 beamlets with a tight control of aberrations. Thus, with an array of 200 Schottky sources, it is possible to produce 20,000 high brightness beams. Aberrations, especially the off-axial aberrations, are analyzed. The total current transmitted is evaluated. Although our objective was to design a 100-beam unit that has a small enough footprint to be part of an array, the 100-beam unit itself is also expected to have applications, for instance in multibeam SEM [3.8], inspection, or nanolithography.

3.2 The Multibeam Source Configuration

The Multi-electron Beam Source (MBS) is designed for a multi-source multi-beam system, with multiple beams per source. The system is aiming for the 22 nm half pitch node, with a throughput of 5-10 WPH. The Schottky source array comprises 200 Schottky emitters,

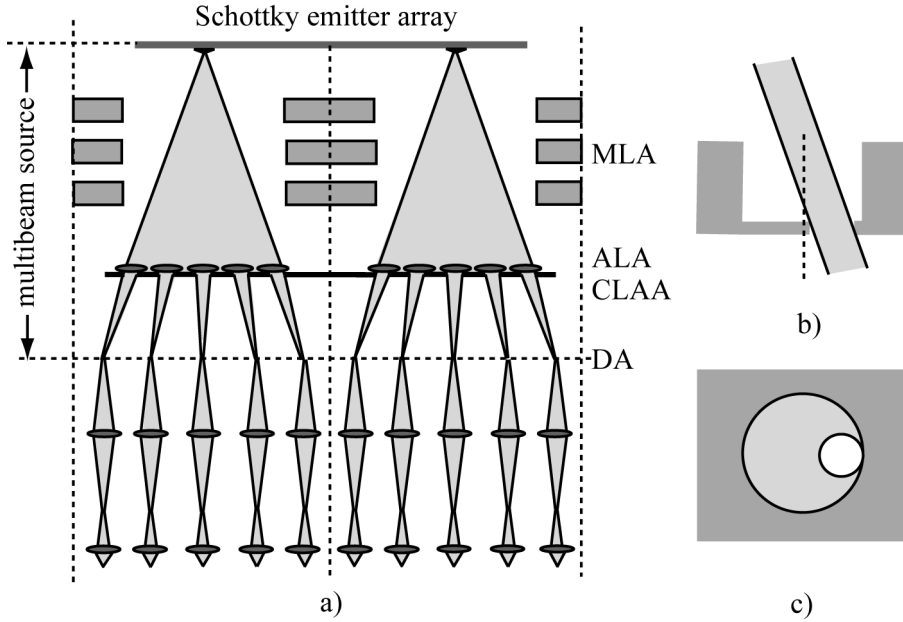


Figure 3-1: a) The configuration of the multi-electron beam source; b) the cross-sectional view and c) the top view of the aperture lens.

arranged in a pitch of 1.5 mm. Each source provides the current for 100 beams with a beamlet current of 10-20 nA. The total number of beamlets delivered to the substrate is 20,000.

The configuration of the MBS is shown in Figure 3-1.a. including a Schottky emitter array, a macro lens array (MLA), an aperture lens array (ALA), a current limiting aperture array (CLAA) and a deflector array (DA). Because the beams from neighbouring sources must be close together, it is not possible to use a collimating lens for obtaining parallel beams. The filling factor (defined as the ratio of beam diameter in the lens plane and the lens diameter) of a normal electron lens is typically no larger than 20%, so the collimating lens would be much larger than the array of 100-beam units. Therefore, an array of deflectors is used to collimate and enable neighbouring groups of beams.

To reduce the deflection aberration in the deflector array, an aperture lens array projects multiple source images at the centre of the deflecting

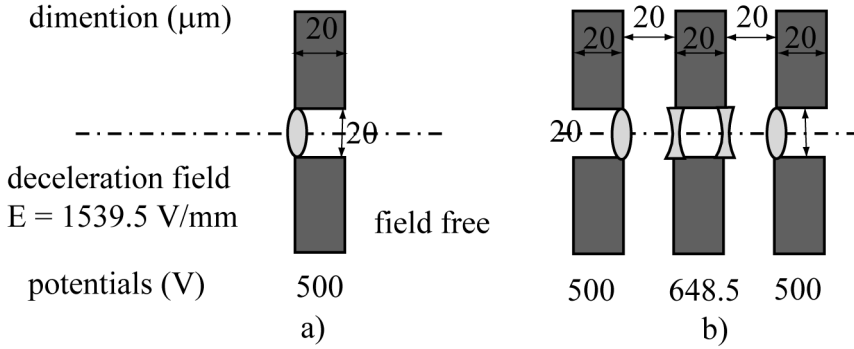


Figure 3-2: The geometry (in microns) and the potential (in volts) of the electrodes, a) an aperture lens; b) an einzel lens

electrodes. These source images serve as secondary sources for the reduction optics. Aperture lenses are preferred because they have smaller spherical aberration coefficients and they are more compact than einzel lenses. Details will be illustrated in section 3 and 4.

When the deflectors are used as a collimating lens, large deflection angles up to tens of mrad are required for the off-axial beamlets. The deflection voltage required can be calculated using the formula below:

$$V = \frac{2d}{l} E \alpha \quad (3-1)$$

where E is the potential of the beam at the deflector array, α is the deflection angle, d and l is the separation and length of the deflecting electrodes. To reduce the deflection voltage, the potential of the deflector array must be kept below 1000 V. Thus, the aperture lens effect must be formed from a deceleration field between the tip and the aperture lens, instead of an acceleration field between the aperture lens and the deflector array. The potential of the aperture lens and the deflector array is designed to be equal. Supports for the thin aperture plate may be put in this field free region.

To avoid beam broadening and transverse chromatic aberration due to the deceleration field, a three-electrode macro lens is introduced in front of the aperture lens array. The aperture lens holes are facing the macro lens, as shown in Figure 3-1.b, and the current limiting apertures are on

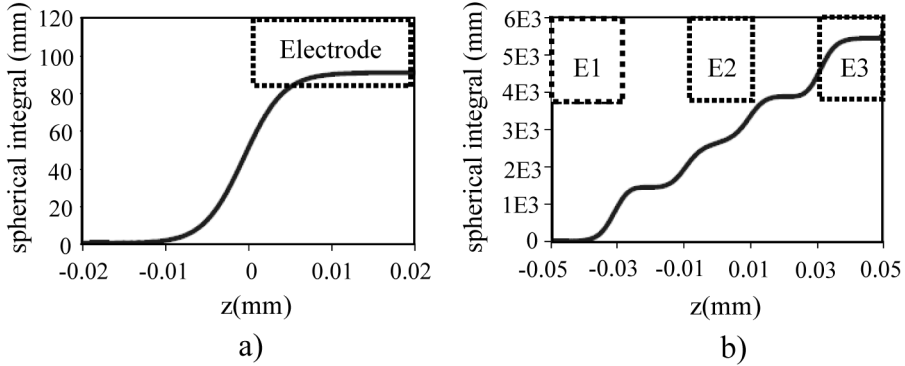


Figure 3-3: a) The spherical aberration integral for the aperture lens; b) the spherical aberration integral for the einzel lens.

the backside of the plate, in a field free region. The field between the macro lens and aperture lens holes forms the aperture lens effect.

The key component in the MBS is the aperture lens array, which should focus inclined beamlets with minimized off-axial aberrations. At the same time, the off-axial aberrations in the macro lens should be minimized.

3.3 Aperture Lens

The aperture lens is the most elementary electrostatic lens, comprising a single circular aperture in a plane electrode separating two regions of different uniform field. Aperture lenses are often characterized as inferior to uni-potential Einzel lenses because of large chromatic aberrations. The chromatic aberrations of an acceleration field have been studied by Bauer [3.9].

Despite the notorious chromatic aberrations caused by the uniform field, which will be dealt with in section 3.5.1, aperture lenses are expected to have smaller spherical aberration coefficients.

An aperture lens and an einzel lens are simulated for comparison. The geometry and potentials are shown in Figure 3-2. They have the same

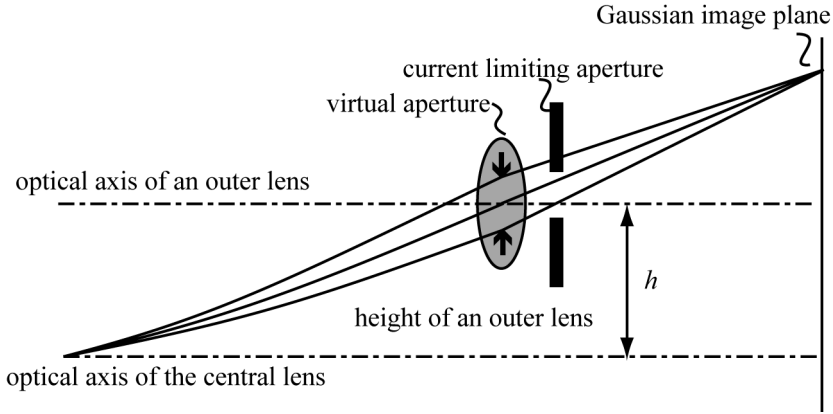


Figure 3-4: An outer lens in the aperture lens array with a shifted current limiting aperture.

focal length of 1.312 mm in the image side. The spherical aberration coefficients are evaluated when the source is at infinity.

The spherical aberration coefficients are obtained in ELD [3.10], where the local contributions to the spherical aberration coefficients are calculated and the integrals of these local contributions along the optical path form the spherical aberration coefficients. Thus the local contributions at different parts of the lens field can be evaluated from the spherical aberration integral plot.

The spherical aberration of the aperture lens is 91 mm, coming from the only focusing effect in the lens aperture, as shown in Figure 3-3.a. The spherical aberration integral of the einzel lens is shown in b, where not only the focusing effects in the first and last electrodes, but also the diverging effects in the central electrode (as shown in Figure 3-2.b) contribute to a positive spherical aberration coefficient of about 1400 mm per part. The total spherical aberration coefficient of the einzel lens is 5458 mm, 60 times larger than that of the aperture lens. When the filling factors of the two lenses are the same, the convergence angle is the same, and the spherical aberration disk of the einzel lens is 60 times larger than that of the aperture lens.

Because the aperture lens has a smaller spherical aberration coefficient, a larger filling factor can be used. For the multi-beam source

with fixed number of beamlets, the total current transmitted to the reduction optics is proportional to the square of the filling factor. Thus the aperture lens is desired because the filling factor is approximately 4 times larger ($60^{1/3}$) than that of the einzel lens. And the total current transmitted from an aperture lens array is approximately 16 times larger than that from an einzel lens array.

3.4 The Aperture Lens Array

The schematic of an outer aperture lens in the aperture lens array is shown in Figure 3-4. The origin is located at the centre of the central aperture lens. The trajectory of the beam is curved due to the deceleration field. The current limiting aperture is in a field free region and shifted to reduce off-axial aberrations, as proposed by Kurihara [3.11]. The virtual aperture is symmetrical with the optical axis and sits in the centre of the lens plane.

The geometry of the aperture lens is the same as that in Figure 3-2.a. The potential in the objective plane is 6621 V and 500 V in the image plane. With an objective distance of 3.976 mm, the electrical field in front of the aperture lens is the same as that of the aperture lens discussed in the previous section, so the aperture lenses have the same strength. The

TABLE 3-1: The optical properties of the central aperture lens

Objective distance (mm)	3.976
Image distance (mm)	5.585
Magnification	-3.258
Angular magnification	-1.117
Focal length (mm)	1.312
Spherical coefficient at image side (mm)	29276
Axial chromatic coefficient at image side (mm)	16.96
Half opening angle at the source (mrad)	1.28
Spherical aberration FW50 (nm)	15.13
Chromatic aberration FW50 (nm)	8.24

optical properties for the central aperture lens are calculated using ELD [3.10] and listed in Table 3-1. Note that Cs here is not the Cs(∞) discussed in the previous section: the Cs at the image side for a situation in which the object is magnified is always larger than Cs(∞). For a half opening angle of 1.28 mrad at the source, the filling factor of the aperture lens is 80%. The image-side spherical and chromatic FW50 disks, the minimum aberration disk containing 50% current of the probe, are calculated using formulas in [3.12].

To evaluate off-axial aberrations of the aperture lens, the deviation from the paraxial trajectory in the Gaussian image plane are calculated using the formulas in Table 3-2, where S_A , K_A , F_A , A_A , D_A , X_A^* and T_A^* are aperture dependent aberration coefficients [3.13, 3.14]. These aberration coefficients of the aperture lens are obtained in ELD [3.10]. The aberration coefficients for a uniform deceleration field, the same as the deceleration field in front of the aperture lens, are also listed for comparison. It is shown that the transverse chromatic aberration, distortion and coma are mainly due to the deceleration field, instead of the aperture lens itself.

The deviations in the Gaussian image plane are plotted in Figure 3-5 as a function of the height of the aperture lens. The total aberration

TABLE 3-2: The deviations from the paraxial trajectory in the Gaussian image plane.

		Coefficients		Deviations
		Aperture lens	DECL	
Geometric	Spherical	1.25E4	-3.00E1	$M \cdot S_A \alpha_a^2 \bar{\alpha}_a$
	Coma	7.72	4.80	$M \cdot K_A \alpha_a \beta_o \bar{\alpha}_a$
	Field curvature	1.31	-7.70E-1	$M \cdot F_A \alpha_a \beta_o \bar{\beta}_o$
	Astigmatism	-6.39E-2	-7.70E-1	$M \cdot A_A \beta_o^2 \bar{\alpha}_a$
	Distortion	1.23E-1	1.23E-1	$M \cdot D_A \beta_o^2 \bar{\beta}_o$
Chromatic	Axial	7.70E1	-3.00E1	$M \cdot X_A^* \alpha_a \Delta V/V$
	Transverse	4.80	4.80	$M \cdot T_A^* \beta_o \Delta V/V$

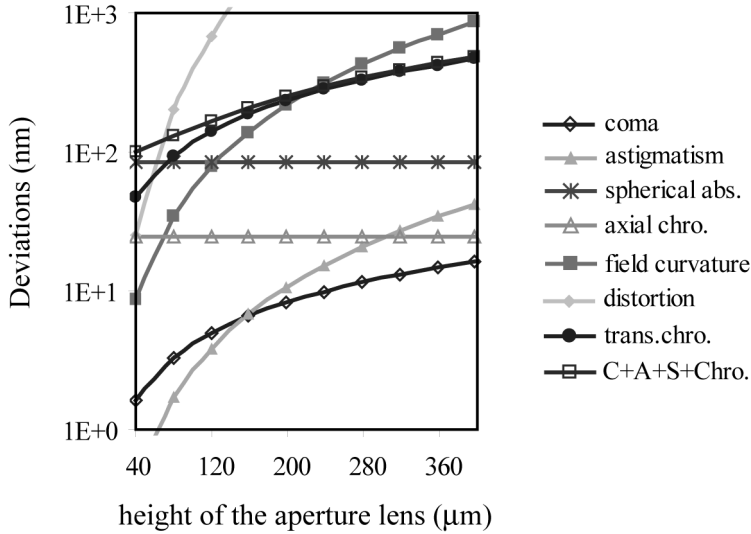


Figure 3-5: The deviations in the Gaussian image plane of the aperture lens.

(square root sum square of spherical aberration, coma, astigmatism and chromatic aberration - C+A+S+Chro) is also shown. The field curvature can be compensated by microlens strength variation, which will be illustrated in section 5.2. Distortion can be corrected by adjusting the lens positions. The total aberration disk is dominated by the transverse chromatic aberration. The transverse chromatic aberration will be greatly reduced by introducing a three-electrode macro lens in section 5.1. Here we will only analyze the uncorrectable geometrical aberrations, e.g., spherical aberration, coma and astigmatism.

The spherical aberration, coma and astigmatism of the aperture lens are evaluated by the FW50 disk. The FW50 disk is determined through ray tracing in Simion [3.15], by recording the through focus series of 500 electrons emitted from an infinitely small source with zero energy spread.

The through focus series of the central aperture lens is shown in Figure 3-6.a. For each beam profile, the aberration disk containing 50% current is determined by increasing the diameter until 250 electrons are included in the disk. The FW50 is determined from the plot of aberration disk versus image position, as shown in the fourth image. The second

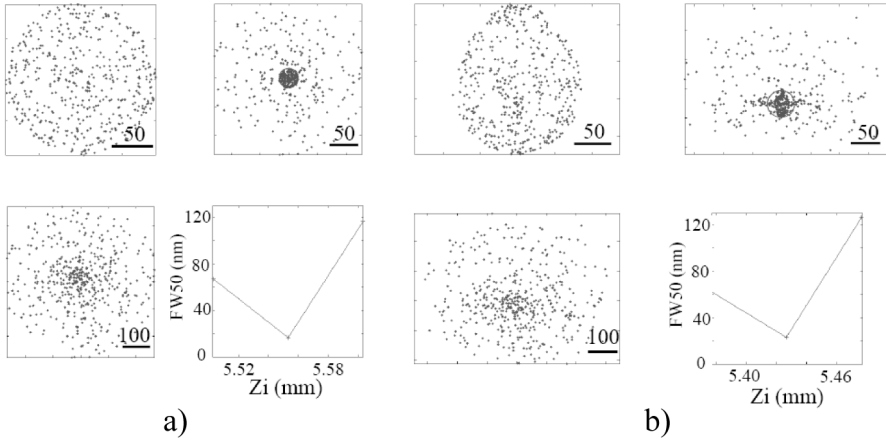


Figure 3-6: The FW50 disk: a) the central aperture lens; b) the aperture lens at 375 μm away from the axis.

image shows the FW50 disk, which has a diameter of 16.4 nm, as indicated by the circle. The first and third images are at 50 μm before and after the FW50 disk. The beam profile changes rapidly with the image position and only spherical aberration is present in the probe. The theoretical spherical FW50 disk is 15.13 nm, as listed in Table 3-1. The theoretical FW50 disk and the FW50 disk determined from ray tracing are in good agreement. The through focus series of the aperture lens at a height of 375 μm is plotted in b, The FW50 disk is determined using the same method and it is 23.0 nm. Astigmatism and a small coma aberration appear in the series.

The FW50 disk versus the height of the aperture lens is shown in Figure 3-7, the incident angle on the aperture lens is also plotted. It is shown that for the aperture lens up to a height of 375 μm , the FW50 disk increases from 16.9 nm to 23.8 nm and the incident angle on the aperture lens increases from 0 mrad to 110 mrad. Assuming a virtual source size of 50 nm, the geometrical source image is 162.9 nm. The total spot size increases from 163.8 nm to 164.6 nm. An aperture lens array with the outermost lens no larger than a height of 375 μm shows acceptable off-axial aberrations. Thus the aperture lens array is a good candidate for

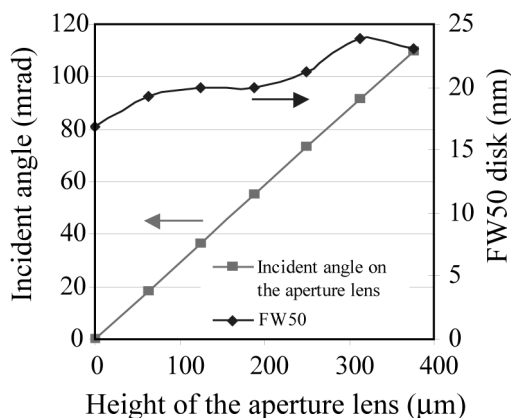


Figure 3-7: The diameter of FW50 disk and the incident angle on the aperture lens.

the MBS, if the transverse chromatic aberration and the field curvature can be reduced.

3.5 The Off-axis Aberrations of the Macro Lens

In order to reduce the transverse chromatic aberration and field curvature, and prevent beam broadening due to the deceleration field, a three-electrode macro lens is used. The 3-electrode macro lens configuration and electrode potentials are shown in Figure 3-8. The aperture lens plate and the deflector array plate (not shown in Figure 3-8) are both at 500 V.

The field between the macro lens and the aperture lens has three functions:

- 1), The potential difference between the last macro electrode and the aperture lens plate forms a deceleration field, which is necessary for the aperture lens effect. The electrical field in front of the aperture lens is equal to that of the aperture lens in section 3.

- 2), Comparing the equipotential lines in Figure 3-9.a (without aperture plate) and b (with aperture plate), the focusing effect in the last macro electrode is suppressed by the aperture lens plate, as circled in b.

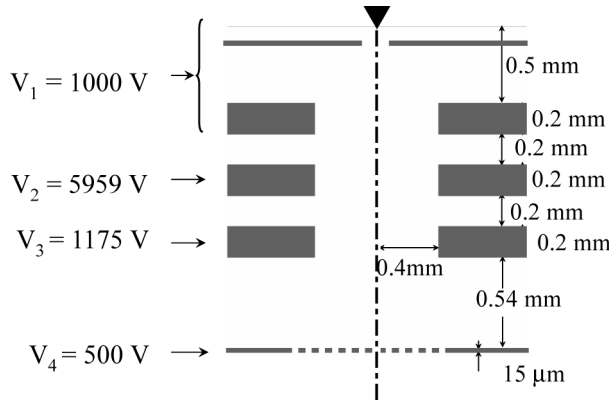


Figure 3-8: The macro lens configuration and the potentials for the electrodes.

As a result, the diverging effect in the central electrode is larger than the focusing effect and the beam diverges in the last part of the macro lens. If the beam half opening angle is 100 mrad, the beam diameter in the aperture lens plate is 300 μm . From the ray tracing result in c, the macro lens operates in a 'zero strength' mode: a ray emitted with an angle of 100 mrad hits the aperture lens plate with 85 mrad.

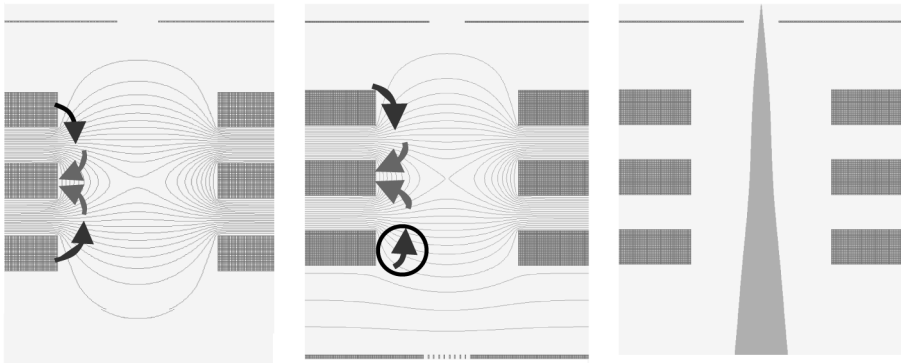


Figure 3-9: a) The equipotential lines of the macro lens without the aperture lens plate; b) the equipotential lines of the macro lens with the aperture lens plate; c) the ray tracing through the macro lens.

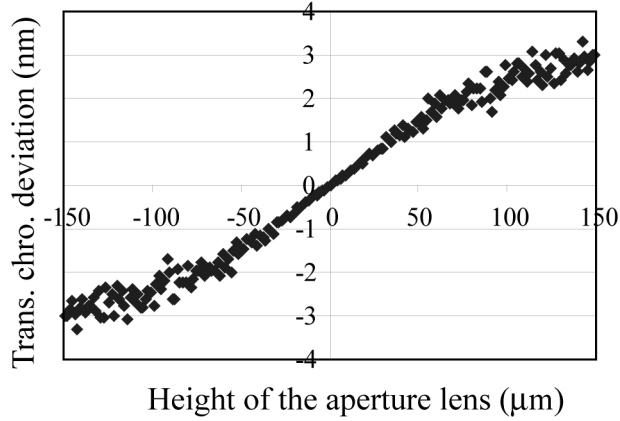


Figure 3-10: The transverse chromatic deviation of the macro lens.

3), The field for the central aperture lens is stronger than that of the outer lenses. This field variation induces microlens strength variation, which may be used for field curvature correction.

3.5.1 Transverse Chromatic Aberration of the Macro Lens

By introducing the macro lens, the deceleration field is limited between the last macro electrode and the aperture lens plate. By adjusting the potentials and distance between the macro lens and the aperture lens plate, the transverse chromatic aberration of the deceleration field can be compensated by the focusing effect in the first two macro electrodes.

The transverse chromatic deviation of the MBS for an energy spread of 0.5 eV is evaluated in the virtual Gaussian image plane using the method of ray tracing. The transverse chromatic deviations seen by aperture lenses are plotted in Figure 3-10, as a function of the height of the aperture lens. The deviation is 3 nm for the outermost aperture lens. The magnification of the macro lens is 1.612, so assuming a virtual source size of 50 nm, the virtual image of the source is 80.5 nm. Thus the transverse chromatic aberration can be neglected.

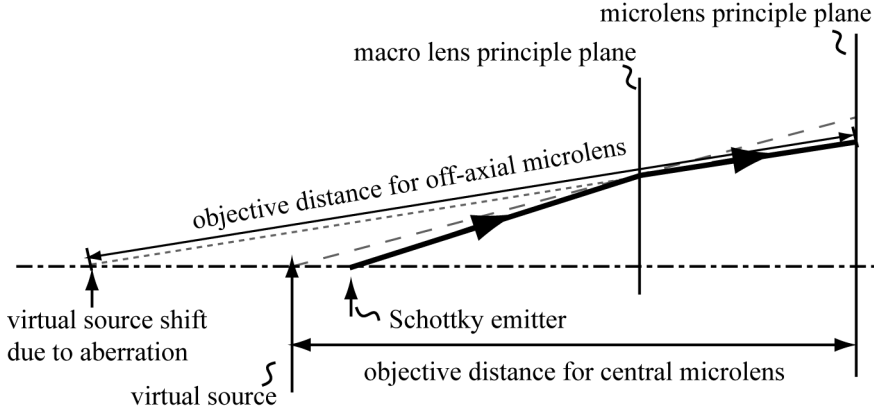


Figure 3-11: The different objective distance for central and outer apertures.

3.5.2 Field Curvature Correction using Microlens Strength Variation

The field curvature of the MBS can be categorized as two parts: the geometrical field curvature and the field curvature due to the macro lens aberration, as shown in Figure 3-11. The geometrical field curvature is intrinsic for the MBS due to the outer beam travelling with an angle. The macro lens aberration shifts the virtual source seen by the outer lenses further, resulting a longer objective distance and thus a positive field curvature in the image side.

The field curvature can be corrected using microlens strength variation. The electrical field in front of the aperture plate is plotted in Figure 3-12.a as a function of the height of the aperture lens. The focal length of the aperture lens is inversely proportional to the electrical field, calculated using formula $f = 4U/E$, where U is the potential in the centre of the aperture lens and E is the electrical field in front of the aperture lenses. The focal lengths of the aperture lenses are plotted in b, where the central aperture lens has a smaller focal length. The objective distances seen by the aperture lenses are determined from simulation. The image distance is then calculated and plotted in c, which shows the field

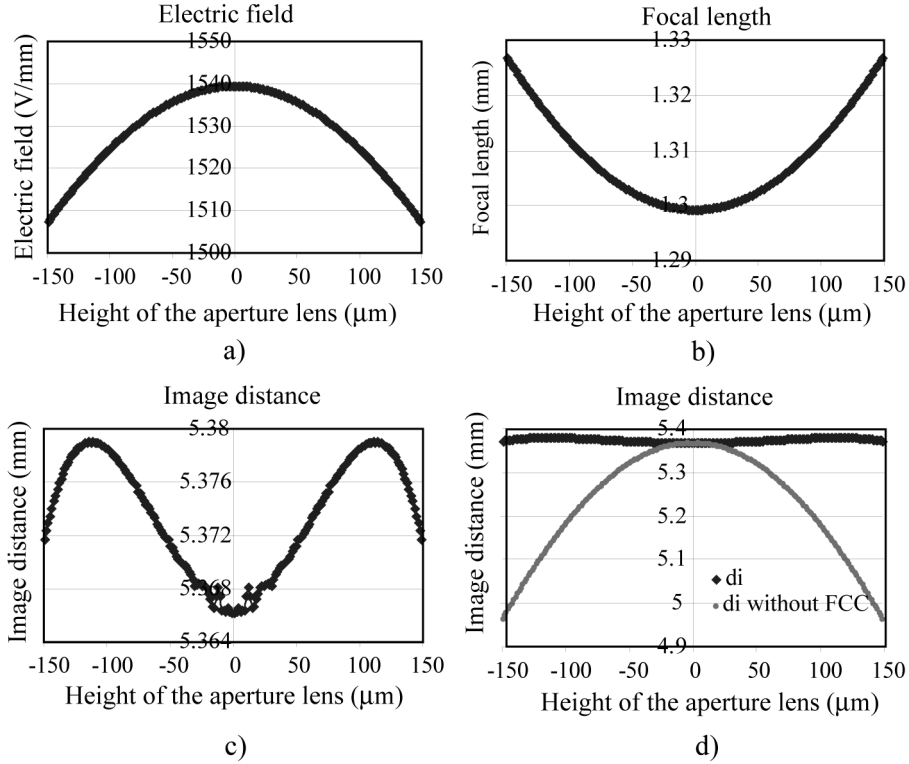


Figure 3-12: a) The electrical field in front of aperture lenses; b) the focal length of the aperture lenses; c) the remaining field curvature after correction; b) the comparison of the field curvature with and without correction.

curvature is within $13 \mu\text{m}$. The shape of the field curvature is due to leftover higher order aberrations. The image distance without field curvature correction (assuming the focal length of outer lenses are the same as that of the central lens) is plotted in d for comparison, where the field curvature is $403.8 \mu\text{m}$.

The transverse chromatic aberration and field curvature are greatly reduced. The beam broadening effect of the deceleration field is

compensated by the focusing effect of the macro lens and thus a larger half opening angle at the source can be used for the same filling factor.

3.6 System Performance

The total column length from the tip to the deflector array is 7.5 mm. 100 aperture lenses are arranged hexagonally with a pitch of 25 μm approximately. The macro lens and the aperture lens array project multiple source images with a pitch around 105 μm at the deflector array. The magnification of source unit comprising the macro lens and the aperture lens is -5.1.

Generally speaking, the aberrations are proportional to the refraction power of a lens. For the 'zero strength' macro lens, the aberrations are expected to be small. Thus it is appropriate to assume the off-axial aberrations of outer aperture lenses with macro lens are smaller than that of outer aperture lenses with a deceleration field. From the FW50 plot in Figure 3-7, we can assume the FW50 (spherical aberration, coma and astigmatism) for the outermost lens is around 50% larger than the central lens in the MBS. The best image plane is taken in the middle of the field curvature shape. The primary aberrations of the central aperture lens and the outermost lens are listed in Table 3-3, assuming a virtual source size of 50 nm and a half opening angle of 5 mrad (equal to a filling factor of 85%). The transverse chromatic aberration for the outermost lens is equal to the product of the transverse chromatic deviation in the virtual

TABLE 3-3: Primary aberrations for the central and outermost aperture lenses.

	Central	Outermost
FW50 (spherical aberration, coma, astigmatism)	13.2 nm	19.8 nm
Field Curvature	9.0 nm	1.2 nm
Axial chromatic aberration	10.4 nm	10.4 nm
Transverse chromatic aberration	-	9.4 nm
Geometrical spot size	254.4 nm	254.4 nm
Total Spot size	255.1 nm	255.6 nm

Gaussian image plane of the macro lens and the magnification of the aperture lens. Distortion, which can be compensated by adjusting the aperture lens position, is not listed in the table.

Assuming the source brightness of 10^8 A/m²srV and an extraction voltage of 1 kV, the angular current density is 200 μ A/sr. The current per beamlet is 15.7 nA and the total current transmitted from each Schottky source is then 1570 nA. Coulomb interactions will be calculated in the near future.

The deflection voltage can be calculated as $V = 2dE\alpha l$. Assuming the aspect ratio of the deflector is 8, the maximum deflection voltage is 10.625 V.

3.7 Conclusions

Novel electron optical components have been presented with very promising results. The aperture lens is capable of having a filling factor of 85% due to small spherical aberration. The aperture lens array allows skewed incidence up to 110 mrad with very small off-axial aberrations. Together with the macro lens operating at 'zero strength mode', the transverse chromatic aberration and field curvature of the MBS are greatly reduced. From each Schottky source, these optical components produce 100 beamlets with a beamlet current of 15.7 nA.

Reference

- [3.1] G. Winograd, V. Krishnamurthi, R. Garcia, L. H. Veneklasen, M. Mankos, and F. Pease, J. Vac. Sci. Technol. B 18(6), 3052 (2000).
- [3.2] Masato Muraki and Susumu Gotoh, J. Vac. Sci. Technol. B 18, 3061 (2000).
- [3.3] H. Yasuda *et al.*, J. Vac. Sci. Technol. B 14(6), 3813 (1996).
- [3.4] S. Eder-Kapl *et al.*, Microelec. Eng. 83, 968 (2006).

- [3.5] R. F. Pease, *Microelec. Engi.* 78-79, 381 (2005).
- [3.6] L. R. Baylor *et al.*, *J. Vac. Sci. Technol. B* 22, 3021 (2004).
- [3.7] T. H. P. Chang, L. P. Muray, U. Staufer, D. P. kern, *Microelec. Engi.* 21, 129 (1993).
- [3.8] M. J. Van Bruggen, B. van Someren, and P. Kruit, *J. Vac. Sci. Technol. B* 23, 2833 (2005).
- [3.9] E. Bauer, *Ultramicroscopy* 17, 51 (1985).
- [3.10] B. Lencova and G. Wisselink, *ELD 3.7, Electron Optical Design Program Package ELD 3.7* (2002).
- [3.11] K. Kurihara, *J. Vac. Sci. Technol. B* 4(5), 1251 (1986).
- [3.12] J. E. Barth and P. Kruit, *Optik Stuttgart* 101, 101 (1996).
- [3.13] B. Lencova and M. Lenc, *Optik Stuttgart* 97, 121 (1994).
- [3.14] B. Lencova and M. Lenc, *Optik Stuttgart* 105, 121 (1997).
- [3.15] David A. Dahl, *Simion 3D 7.0* (2000)

Chapter 4

High Brightness 100-electron-beam Source for High-resolution Applications

Journal of Vacuum Science and Technology B 25(6), 2239 (2007).

Abstract

The design of a 100-beam source for high-resolution applications is presented, comprising a Schottky emitter, an aperture lens array, an accelerator lens, and a conjugate blanker array. The beamlets emerge at 30 kV, compatible with most scanning electron microscope-type systems commercially available. The aberrations due to the aperture lens array and the accelerator lens are carefully minimized. For a Schottky source with brightness of 1.5×10^8 A/m²srV, the multibeam source is designed to allow a transmission of more than 1000 nA current to the reduction optics with uniform spot sizes.

4.1 Introduction

The progress in microelectronics, nanotechnology and material science demand an ever-increasing spatial resolution and throughput in charged particle beam lithography and inspection. The total current that can be obtained in a single beam is limited by the brightness of the electron source and the Coulomb repulsion between the electrons in the beam. Multibeam systems [4.1-4.11] are under development, which improve throughput without suffering from brightness limitations and Coulomb interactions. To avoid large arrays of individual electron sources in such systems, a multibeam unit is usually arranged between the electron source and the reduction optics, splitting the broad beam into beamlets and generating multiple source images, which serve as intermediate virtual sources for the reduction columns. The design of the multibeam unit presents several challenges. The first one is to accept as much of the emitted broad beam into the sub-beams as possible; after all, the goal is to create a high current system. This translates to the demand for large filling of the microlenses, which is, apart from limitations by normal lens aberrations, complicated further by the inclination of the outside beamlets in the lens array. The second challenge is to bend the outermost beams from the single source into the right direction without introducing deflection aberrations that would deteriorate the effective brightness of the beamlets.

Electron sources with Schottky emitters are the most widely used sources for high resolution applications in electron microscopy, inspection and lithography. The useful current of Schottky sources, which is emitted from the facet of the emitter and having uniform current density, is limited to a few microamperes. So for applications with a few nanoamperes per beamlet, the maximum number of beamlets for a single Schottky emitter is about 100. For massively parallel lithography or inspection, we have proposed to develop a source with arrayed Schottky emitters at a pitch of 1.5 mm, and 100 beamlets per emitter [4.11]. The requirement that the 100-beamlet single Schottky emitter units have to be stacked in a closely packed array, limits the design parameters. This results in a design with severe engineering challenges, such as fine

alignment, extremely high tip stability requirement, high electric field and tight thermal control of close-packed array of emitters [4.12]. We are also worried about the Coulomb interactions in such a design.

In this work, a new configuration for a 100-beam source is presented. The configuration of the multibeam source is described in section 4.2. Aberrations due to different components are discussed in section 4.3-4.5. Field curvature correction is explained in section 4.6 and the system performance is evaluated in section 4.7.

4.2 The Configuration of the Multibeam Source

The configuration of the multibeam source (MBS) is shown in Figure 4-1, comprising a Schottky emitter, an aperture lens array, an accelerator lens and a blanker array. The aperture lens array splits the broad beam into beamlets and projects multiple source images at the blanker array. These source images serve as secondary sources for the reduction optics. Individual beam on/off switching is controlled by the blanker array and a blanking aperture (or blanking aperture array) in the reduction column. The blanker array is in a conjugate plane of the source, chromatic deflection aberration is reduced and spots at the wafer do not shift during blanking or due to crosstalk. The blanker array will not be discussed in this work, but the design and fabrication of a similar type has been presented elsewhere [4.13].

The extraction voltage of the Schottky emitter is chosen at 4 kV. The distance between the tip and the extractor is decided accordingly to obtain sufficient electric field in front of the tip. The distance between the tip and current limiting aperture array is kept small (~ 3 mm) to limit Coulomb interactions, while leaving enough space for a multipole deflector (not shown in Figure 4-1), which is used to compensate for tip drift.

The aperture lens array is made on a thin Silicon membrane and is at the potential of extraction. The aperture lens effect is formed by penetration of the strong acceleration field into the lens holes, as shown by the equipotential lines in Figure 4-1. The current limiting aperture is on the other side of the membrane (closer to tip), integrated with the

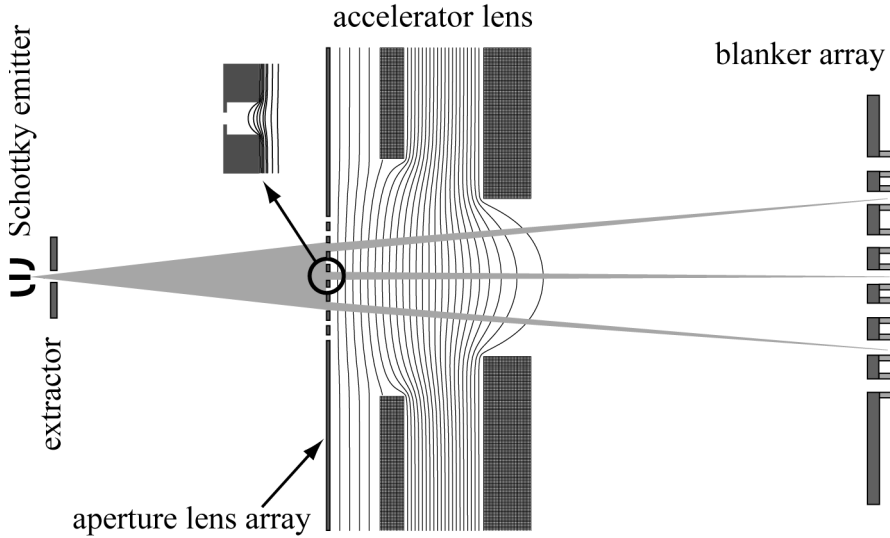


Figure 4-1: Configuration of the multibeam source, comprising a Schottky emitter, an aperture lens array, an accelerator lens and a blanker array. The equipotential lines are plotted. The central aperture lens is enlarged, showing the integrated current limiting aperture and the equipotential lines forming the aperture lens effect.

aperture lens array and sitting in a field free region, as shown in the enlarged central aperture lens. One of the great advantages of a single aperture lens array is that the precise alignment of two or more lens electrodes is avoided. The two-electrode accelerator lens elevates the potential to 30 kV. The high voltage is compatible with most SEM-type systems commercially available.

The key component in the MBS is the aperture lens array, which should focus inclined beamlets with minimized off-axial aberrations. At the same time, the off-axial aberrations in the accelerator lens should be well controlled.

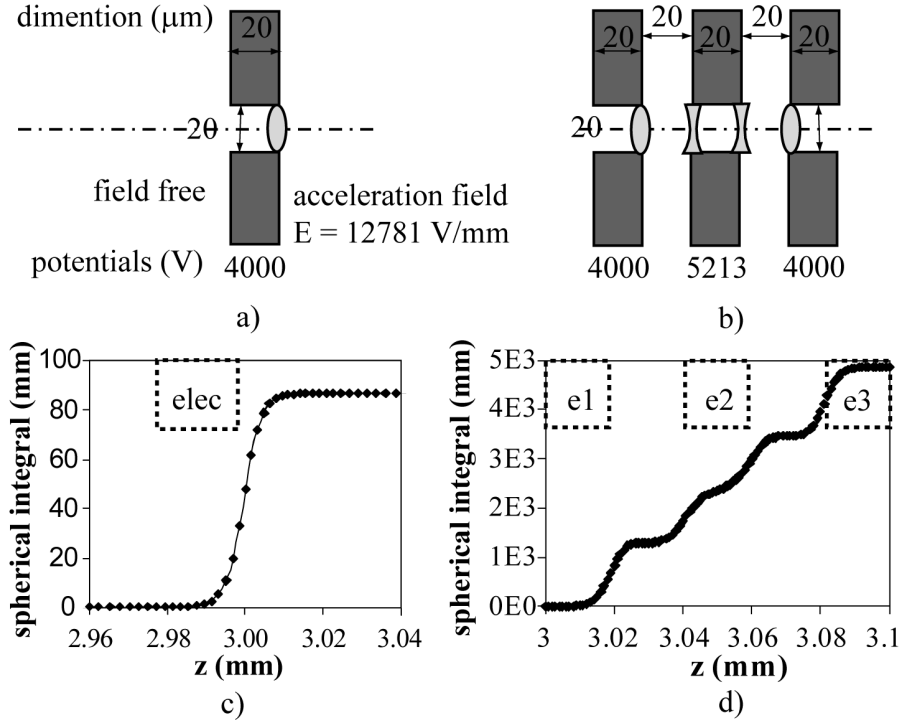


Figure 4-2: a) Geometry, potential and field of the aperture lens; b) the geometry and potential of the einzel lens; c) The spherical integral of the aperture lens; and d) the spherical integral of the einzel lens.

4.3 Axial Aberrations of the Aperture Lens

As the most elementary electrostatic lens, aperture lenses have superior properties: for the same maximum field, aperture lenses have the shortest focal length and very low spherical aberrations, comparable to and better than those of magnetic lenses of the same focal length [4.14].

TABLE 4-1:Optical properties of the central aperture lens.

Objective distance (mm)	3
Image distance (mm)	6
Magnification	-0.73
Angular magnification	-0.31
Focal length at object side (mm)	1.26
Half opening angle at the source (mrad)	3
Spherical coefficient at object side (mm)	2704.21
Axial chromatic coefficient at object side (mm)	5.45
Spherical aberration FW50 at object side (nm)	13.14
Chromatic aberration FW50 at object side (nm)	0.69

However, their application is impaired due to the difficulty of having the target in the uniform field.

To compare the axial aberration coefficients of an aperture lens to those of an einzel lens, computer models are built with the same lens diameter and focal length ($f_{\text{obj}}=1.264$ mm). The geometry and potentials are shown in Figure 4-2. ELD [4.15], a 2D first-order finite element program for electrostatic lens design is used to calculate the axial aberrations at the object side at infinite magnification. The chromatic aberration coefficients for both lenses are of similar magnitude ($C_c(\infty)=1.25$ mm for the aperture lens and $C_c(\infty)=2.20$ mm for the einzel lens). However, the spherical aberration coefficient ($C_s(\infty)$) of the einzel lens is 4873.54 mm, much larger than that of the aperture lens (86.65 mm).

The spherical integrals, which illustrate the contribution of $C_s(\infty)$ from different parts of the lens, are plotted in Figure 4-2.c for the aperture lens and in Figure 4-2.d for the einzel lens. As shown, the $C_s(\infty)$ of the aperture lens comes from the focusing effect in the lens aperture; while the $C_s(\infty)$ of the einzel lens has four contributions: not only the focusing effects in the first and last electrodes, but also the diverging effects in the central electrode (as shown in Figure 4-2.b) contribute to a positive spherical aberration coefficient of about 1218 mm per part. Each part is larger than the whole single aperture because the focusing effect of each part must be larger than the focusing effect of the single aperture lens: in an einzel lens, the net focusing effect is the difference between two

positive contributions and two negative contributions. As a result, the $C_s(\infty)$ of the einzel lens is 56.24 times larger than that of the aperture lens.

The small $C_s(\infty)$ leads to a great advantage for the multibeam source: if the spots projected by the microlenses are dominated by spherical aberration, a smaller $C_s(\infty)$ means a larger beam opening angle. Filling factor (FF), defined as the ratio of the beam diameter in the lens plane and the lens diameter, is proportional to the beam opening angle and it is a very important figure for the multibeam source, because the total current transmitted is proportional to the square of the filling factor:

$$I = cj\pi\alpha^2 FF^2 \left(\frac{d_l}{P_l} \right)^2 \quad (4-1)$$

where c is a coefficient related to the geometrical arrangement of the microlenses, α is the half opening angle of the broad beam, j is the angular current density of the source, P_l is the lens pitch and d_l is the lens diameter. The smaller $C_s(\infty)$ leads to a larger beam opening angle, a larger filling factor, and thus a larger total current.

Therefore, by using the aperture lenses, the beamlet half opening angle, and thus the filling factor, is $56.24^{1/3}$ times larger due to the smaller $C_s(\infty)$ than that of einzel lenses. The total current is 14.68 ($56.24^{2/3}$) times larger than that of a multibeam source with the einzel lens array.

4.4 The Aperture Lens Array

To reduce off-axial aberrations, the current limiting aperture of an outer lens is shifted such that the virtual aperture sits in the lens plane and is symmetrical along the optical axis of that lens [4.11]. The lens diameter is small compared to the electrode thickness to create a limited lens field. This is advantageous because the current limiting aperture array can be integrated with the microfabricated aperture lens array, and fine alignment between these two arrays is possible by a mask aligner with sub-micron resolution.

TABLE 4-2: Deviations in Gaussian image plane for the outermost lens with an incident angle of 0.05 rad.

			Deviations		
		Formulas	Total deviations	Uniform field	Aperture lens
Geometric	Spherical	$M \cdot S_A \alpha_a^2 \bar{\alpha}_a$	-53.17	0.06	-53.23
	Coma	$M \cdot K_A \alpha_a \beta_o \bar{\alpha}_a$	2.23	0.72	1.51
	Field curvature	$M \cdot F_A \alpha_a \beta_o \bar{\beta}_o$	-20.47	8.73	-29.20
	Astigmatism	$M \cdot A_A \beta_o^2 \bar{\alpha}_a$	-1.18	8.73	-9.91
	Distortion	$M \cdot D_A \beta_o^2 \bar{\beta}_o$	106.02	106.02	0.00
Chromatic	Axial	$M \cdot X_A^* \alpha_a \Delta V / V$	-1.49	0.44	-1.93
	Transverse	$M \cdot T_A^* \beta_o \Delta V / V$	5.29	5.29	0.00

The optical properties of the aperture lens array are listed in Table 4-1. The geometry, electrode potential and electric field of the aperture lenses are the same as that in the previous section. Note that C_s here is not the $C_s(\infty)$ discussed in the previous section: the C_s for a situation in which the object is not infinitely magnified is always larger than $C_s(\infty)$ and having the relationship as $C_s = C_s(\infty) \cdot (1 + 1/M)^4$. For a half opening angle of 3 mrad at the source, the filling factor of the aperture lens is 90%. The spherical and chromatic FW50 disks in the object side are calculated using formulas in [4.16]. Note that we are assuming that the walls of the lens electrode are perfectly smooth and have a uniform potential. It is an experimental and engineering challenge to obtain that. An alternative for the present design is to use a thin membrane lens array (electrode thickness \ll lens diameter), and aperture the beams further downstream in the system.

The total deviations in the Gaussian image plane for the aperture lens array are calculated using the formulas in Table 4-2, where S_A , K_A , F_A , A_A , D_A , X_A^* and T_A^* are aperture-dependent aberration coefficients and calculated in ELD, α_a and β_o are the complex slope and complex coordinate in the object plane [4.17, 4.18], as shown in Figure 4-3.a.

The aberrations due to the uniform acceleration field are calculated in ELD by setting the aperture position at the source position. The complex coordinate and slope are set in the asymptotic object plane, which is located at the image position of the aperture lens (without the acceleration field effect), as illustrated in Figure 4-3.b. Note that for the uniform field simulation, α_a has an opposite sign from the α_a in Figure 4-3.a, because the angular magnification of the aperture lens is negative; β_o also has an opposite sign from the β_o in Figure 4-3.a because

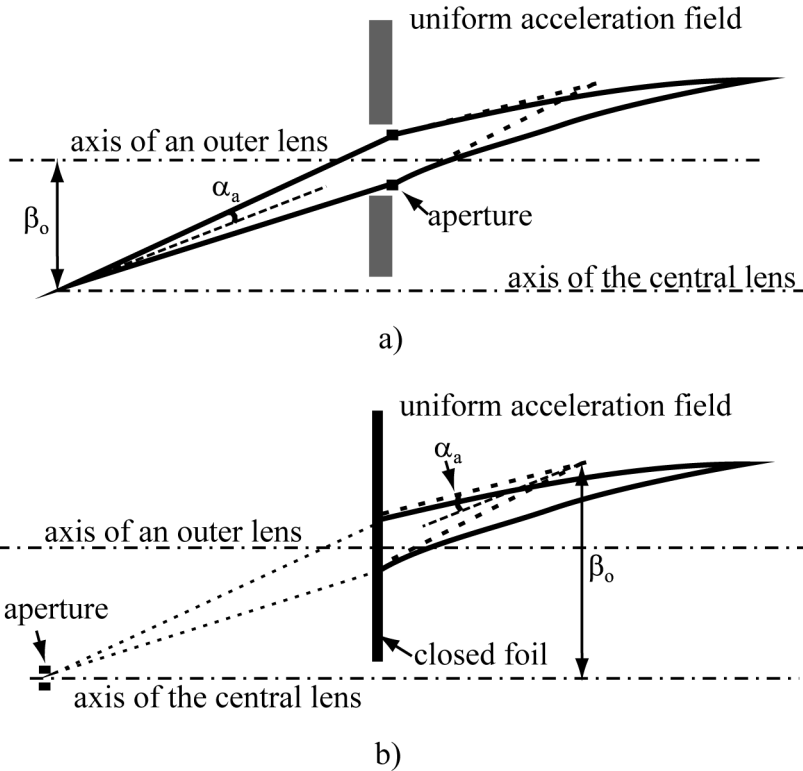


Figure 4-3: a) Complex coordinate and slope in the object plane, and the aperture for simulating the aberrations of the aperture lens array; b) complex coordinate and slope in the asymptotic object plane, and the aperture for simulating the aberrations of the uniform field.

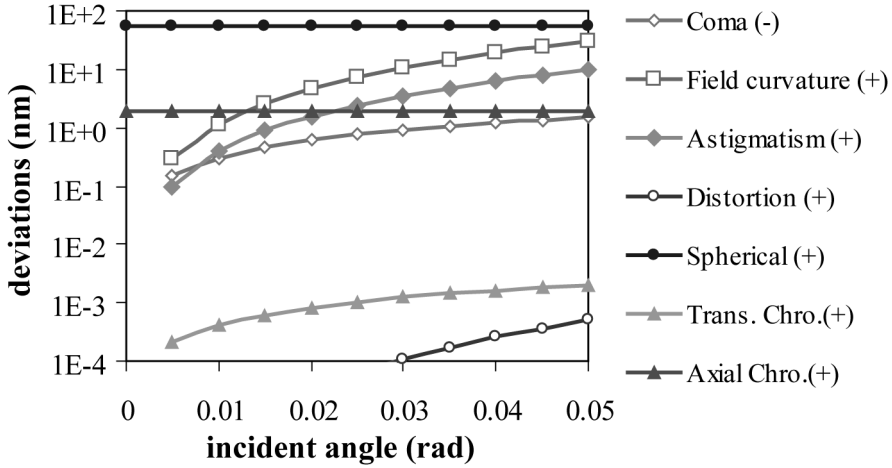


Figure 4-4: Amplitude of deviations in the Gaussian image plane due to the aberrations of the aperture lens.

the object and image are always in different sides of the axis of the outer lens. The magnification of the uniform field is 1. The total deviations and the deviations due to the uniform field are listed in Table 4-2, calculated for the outermost lens with an incident angle of 0.05 rad.

The deviations due to the aperture lens array itself are extracted by subtracting the deviations of the uniform field from the total deviations. It is shown that the transverse chromatic aberration and distortion are mainly due to the acceleration field, instead of the aperture lens array. The same result has been observed previously [4.11].

The amplitude of deviations in the Gaussian image plane due to the aperture lenses is plotted in Figure 4-4, as a function of the incident angle. The sign of the aberrations is shown in the legend. The spherical aberration is the largest contribution, equal to a FW50 disk of 9.5 nm in the image side. Note that the spherical FW50 disk is calculated by times 0.18 of the deviations in the Gaussian image plane [4.16].

4.5 The Accelerator Lens

Bauer [4.19] has shown that for LEERM (low energy electron reflection microscope), the spherical aberration and chromatic aberration are much larger in the immersion lens than in the homogeneous acceleration field such that the aperture has to be reduced by a factor of two and the resolution is by a factor of 2 worse. In the multibeam source, however, a uniform acceleration field can not be used because the blanker array should be in a field free region. An accelerator lens is built to supply the acceleration field for the aperture lens array locally and project the multiple virtual images at the blanker array, with well controlled aberrations.

The accelerator lens has two electrodes: the first electrode has a thickness of 0.25 mm and a radius of 1.2 mm, while the second one has a thickness of 0.5 mm and a radius of 0.8 mm. The geometry, axial field and potential of the accelerator lens are plotted in Figure 4-5. The electric field in front of the central aperture lens is the same as discussed in the previous two sections and the central aperture lens has the same focal

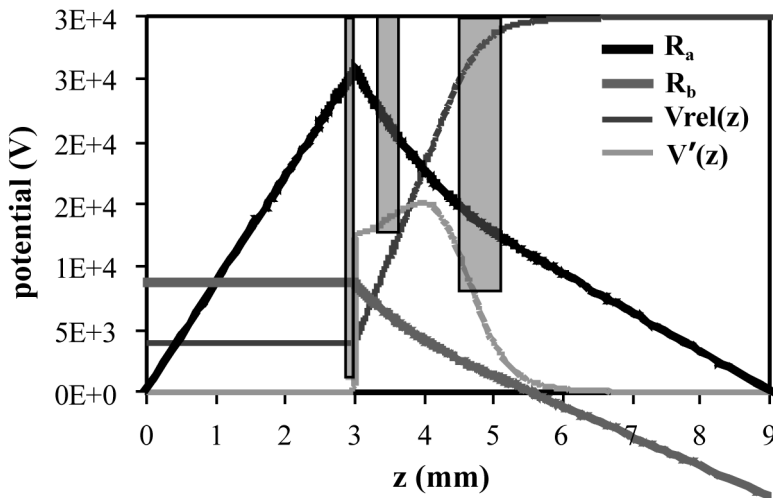


Figure 4-5: Configuration of the accelerator lens, showing two characteristic trajectories, the axial potential and field.

length. Two characteristic trajectories $R_a(z)$ and $R_b(z)$, defined by their initial coordinates in the object plane $z = z_o$,

$$\begin{aligned} R_a(z_o) &= 0, \quad R'_a(z_o) = 1; \\ R_b(z_o) &= 1, \quad R'_b(z_o) = 0; \end{aligned} \quad (4-2)$$

are also illustrated in Figure 4-5. The virtual images from the aperture lenses are projected into the blanker array with a magnification of 1.36.

To study the aberrations of the accelerator lens, especially the off-axis aberrations, the aperture lens array is treated as a closed foil in the simulation because the lens holes are very small compared to the accelerator lens and only change the field locally. The aberration coefficients are simulated in the same way as for the uniform field. It shows that the accelerator lens is a negative lens, having a negative focal length, and all the aperture dependent coefficients are negative. This is very unique to this design because the negative aberrations from the accelerator lens may cancel the positive aberrations from the aperture lens array or from the reduction column. The deviations in the Gaussian image plane are calculated using the formulas in Table 4-2 and the amplitude is plotted in Figure 4-6.

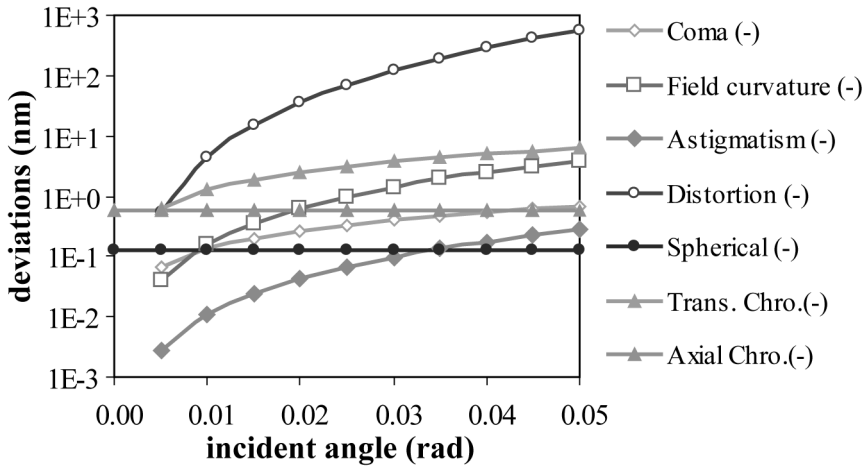


Figure 4-6: Amplitude of deviations of the accelerator lens in the Gaussian image plane.

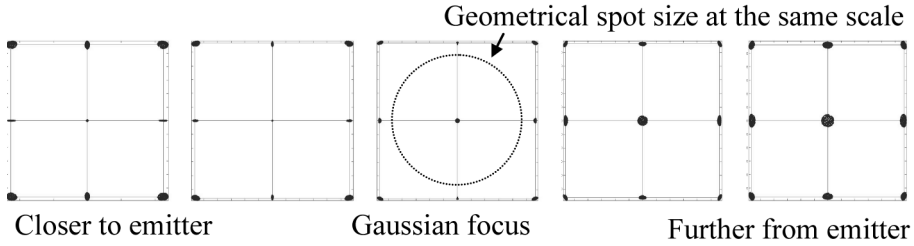


Figure 4-7: Central 3 by 3 through focus series in the accelerator lens. The pitch is 38 μm , aberration disks are magnified 2000 times.

The deviations for the whole system are the sum of the deviations due to the aperture lenses times the magnification of the accelerator lens and the deviations due to the accelerator lens: which result a coma of 2.73 nm, astigmatism of -13.16 nm, spherical deviation of -72.04 nm, chromatic deviation of -2.04 nm and transverse chromatic aberration of 6.29 nm. Field curvature is not listed because it can be corrected by field variation and will be discussed in the next section. These data divided by the magnification of the accelerator lens are comparable to the total deviations as shown in Table 4-2. It shows all the deviations are comparable or smaller except astigmatism, which is mainly induced by the aperture lenses. The spherical aberration is still the largest contribution.

The through focus series for the central 3-by-3 beamlets are shown in Figure 4-7, assuming there is no aberrations from the aperture lens array. The aberration disks are magnified by 2000 times, and the geometrical source size is plotted in the same scale and is much larger than the aberration disks. Negative field curvature is shown as expected (the central beamlet focuses at a shorter distance to the emitter). Negative astigmatism is also present from the through focus series of the outer beams.

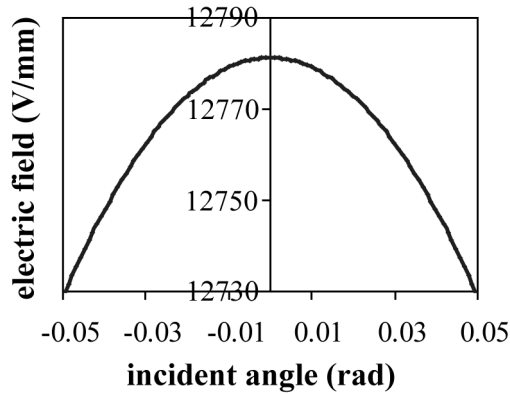


Figure 4-8: Electric field in front of the aperture lens.

4.6 Field Curvature Correction

Field curvature in the MBS has three parts: the positive geometrical field curvature, a positive contribution from the aperture lens array and a negative contribution from the accelerator lens. The geometrical field curvature is intrinsic for the MBS due to the fact that outer beams are travelling obliquely.

Because the focal length of aperture lenses is inversely proportional to the electric field, field curvature can be compensated by varying the field in front of the aperture lens array. The field can be adjusted by the geometry of the accelerator lens and the electrode potentials, creating a stronger field for the central aperture lens. The field variation in front of the aperture lens array is shown in Figure 4-8, assuming the aperture lens plate is a planar surface without lens holes. The field curvature can be fully compensated by adjusting the geometry and potentials of the accelerator lens. Slight overcompensation is preferred because the presence of the lens holes may decrease the field variation.

4.7 The Multibeam Source Performance

The total length from the tip to the blanker array is 8.9 mm. 100 aperture lenses are fabricated on a 20 μm -thick Silicon membrane, arranged in a hexagonal pattern at a pitch of 25 μm . The lens array and accelerator lens project multiple source images at a pitch around 38.4 μm at the blanker array. The half opening angle of the broad beam is limited around 0.05 rad, where the angular current density is uniform.

Assuming the Schottky emitter has a tip radius of 0.62 μm , the distance between the tip and extractor is 0.381 mm, this would give a virtual source size of 32.9 nm, an angular current density at the extractor of 0.5 mA/sr, and a reduced brightness of $1.5 \times 10^8 \text{ A/m}^2\text{srV}$ [4.20, 4.21]. The system performance is listed in Table 4-3. The central spot size is calculated by adding spherical and chromatic FW50 disks to the geometrical spot size, using formulas in [4.16]. For the outermost spot size, coma, astigmatism and transverse chromatic deviations are added to the central spot size using square root of the sum of squares. Field curvature is compensated. Negative distortion is ignored because it doesn't blur the beams and may be corrected by adjusting the position of

TABLE 4-3: System performance of the multibeam source.

Beam half opening angle (mrad)	3
Reduced Brightness ($\text{A/m}^2\text{srV}$)	1.5×10^8
Filling factor	90%
Potential at objective side (V)	4000
Potential at image side (V)	30000
Magnification	0.99
Angular magnification	0.37
C_s at image side (mm)	5.63 E4
C_c at image side (mm)	1.11 E2
Central spot size (nm)	40.4
Outermost spot size (nm)	43.1
Beamlet current (nA)	14.14
Total current (nA)	1414

aperture lenses or compensated by the positive distortion in the reduction column.

Trajectory displacement in the multibeam source is mainly in the section between the tip and the current limiting aperture array, where the broad beam is not yet split. Assuming the beam is travelling with a constant potential of 4 kV, the FW50 value due to trajectory displacement is roughly estimated at 4.93 nm [4.20]. The Boersch effect occurs mainly in a short distance (microns) after the tip, where the beam potential is low and current density is high. More details can be found in [4.22, 4.23].

4.8 Conclusions

It is possible to design a multibeam source, having the following properties:

- (1) a 90% filling factor of the aperture lens due to its small spherical aberration coefficient,
- (2) reduced off-axial aberrations of the aperture lens array by shifting current limiting apertures for the off-axial lenses,
- (3) full compensation of field curvature by adjusting the geometry and electrode potentials of the accelerator lens,
- (4) acceleration to a potential of 30 kV without introducing much transverse chromatic aberration.

The multibeam source is capable of delivering more than 1 μA current to the reduction optics with minimized aberrations.

A multibeam source with different requirements: such as magnification, pitch, beam potential etc., can be built with similar components with the same principles.

The performance of the multibeam source is dependent on the Schottky emitter. Only axial properties of the Schottky emitter, such as brightness and energy spread, have been investigated till now, and it is not yet clear if off-axial beamlets will have the same properties. Currently, an experimental setup is being built to test the emitter and subsequently, the multibeam source performance.

Reference

- [4.1] M. J. Van Bruggen, B. van Someren, and P. Kruit, J. Vac. Sci. Technol. B 23, 2833 (2005).
- [4.2] Masato Muraki and Susumu Gotoh, J. Vac. Sci. Technol. B 18, 3061 (2000).
- [4.3] Stefan Eder-Kapl *et al.*, Microelec. Engi. 83, 968 (2006).
- [4.4] P. Kruit, Microelec. Engi. 84, 1027 (2007).
- [4.5] A. van den Brom, A. van Veen, W. Weeda, G. Berglund, M. Wieland, and P. Kruit, J. Vac. Sci. Technol. B 25, 2245 (2007).
- [4.6] D. S. Pickard, T. R. Groves, W. D. Meisburger, T. Crane, and R. F. Pease, J. Vac. Sci. Technol. B 21, 2834 (2003).
- [4.7] S. T. Coyle *et al.*, J. Vac. Sci. Technol. B 22, 501 (2004).
- [4.8] S. Tanimoto *et al.*, J. Vac. Sci. Technol. B 25, 380 (2007).
- [4.9] L. R. Baylor *et al.*, J. Vac. Sci. Technol. B 22, 3021 (2004).
- [4.10] T. H. P. Chang, L. P. Murray, U. Staufer, and D. P. Kern, Microelec. Engi. 21, 129 (1993).
- [4.11] Y. Zhang and P. Kruit, Physics Procedia 1, 553 (2008).
- [4.12] A. K. Dokania, J. F. M. Velthuis, Y. Zhang, and P. Kruit, J. Vac. Sci. Technol. B 25, 504 (2007).
- [4.13] Y. Zhang, C. T. H. Heerkens, M. J. Van Bruggen, and P. Kruit, J. Vac. Sci. Technol. B 24, 2857 (2006).

- [4.14]R. Guckenberger and H. Heil, Proc. of the Fifth European Cong. on Electron Microscopy, (1972) unpublished.
- [4.15]B. Lencova and G. Wisselink, ELD 3.7, Electron Optical Design Program Package ELD 3.7 (2002).
- [4.16]J. E. Barth and P. Kruit, Optik Stuttgart 101, 101 (1996).
- [4.17]B. Lencova and M. Lenc, Optik Stuttgart 97, 121 (1994).
- [4.18]B. Lencova and M. Lenc, Optik Stuttgart 105, 121 (1997).
- [4.19]E. Bauer, Ultramicroscopy 17, 51 (1985).
- [4.20]J. Orloff, *Handbook of Charged Particle Optics*, CRC Press (1997).
- [4.21]M. Bronsgeest, private communication.
- [4.22]M. S. Bronsgeest, J. E. Barth, P. Kruit, G. A. Schwind, and L. W. Swanson, J. Vac. Sci. Technol. B 25, 2049 (2007).
- [4.23]A. H. V. van Veen, C. W. Hagen, J. E. Barth, and P. Kruit, J. Vac. Sci. Technol. B 19, 2038 (2001).

Chapter 5

Integrated Multi-electron-beam Blanker Array for Sub-10 nm Elec- tron Beam Induced Deposition

Journal of Vacuum Science and Technology B 24(6), 2857(2006).

Abstract

An integrated multi-electron-beam blanker array is proposed for the multi-electron-beam source (MBS) reported by M. J. Van Bruggen [J. Vac. Sci. Technol. B 23(6), 2005], which aims at the throughput improvement of sub-10 nm electron beam induced deposition (EBID). The integrated blanker array consists of a current limiting aperture array, a blanker array and a micro-aperture-lens array. The integrated blanker array generates 100 individually controlled beamlets, projecting the virtual source image in the principal plane of the field lens. The electrostatic crosstalk, charging and contamination are reduced by the grounded current limiting aperture plate above the blankers. The blanker array and micro-aperture-lens array are fabricated on a first wafer, while the current limiting aperture array is fabricated on a second, 100 μm thick wafer. The wafers will be bonded with an alignment accuracy of approximately 200 nm. The first test chips, where the blankers are grouped and controlled by external circuitries, are under fabrication and key processes are tested.

5.1 Introduction

In order to improve the throughput for maskless lithography, several multi-beam systems are under development [5.1, 5.2]. In such systems, the individual beam on/off switching is essential to define writing patterns. Several multi-beam blanking arrays [5.3-5.6] have been proposed, but the crosstalk, charging and contamination are common problems: Yasuda [5.3] proposed a blanking aperture array, in which the lateral static crosstalk is reduced by guard walls. The system however may suffer from charging and contamination in the apertures. G.Winograd [5.4] proposed another multi-blanker system where the charging is eliminated but the static crosstalk is up to 15% at the crossover plane.

M. J. Van Bruggen [5.7] proposed a multi-beam source module (MBS) for the fabrication of sub-10 nm structures with electron beam

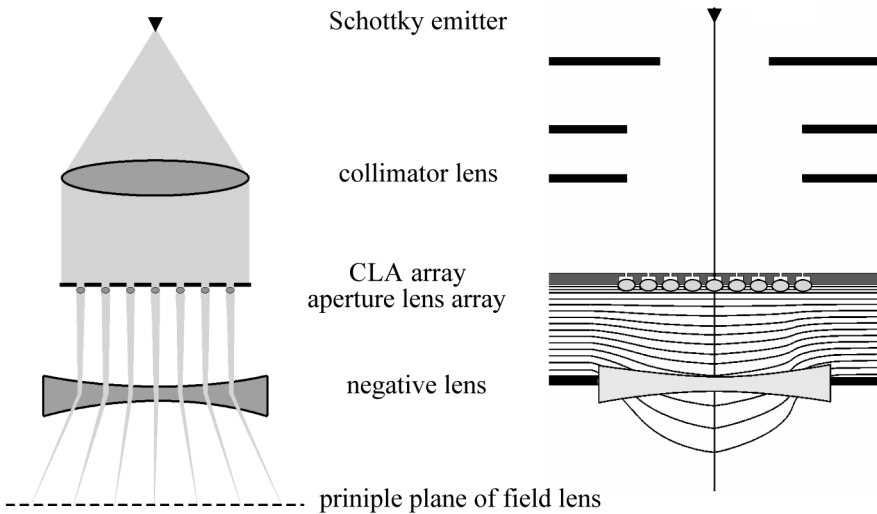


Figure 5-1: a) Schematic of the multi-beam source module.
b) Electrode configuration and the electrostatic field between the micro-aperture-lens array and the negative lens.

induced deposition (EBID). The module consists of a Schottky emitter, a collimator lens, a 10 by 10 current limiting aperture array (CLAA), a 10 by 10 micro-aperture-lens array (ALA) and a negative lens, as shown in Figure 5-1.a. The electrode configuration and the electrostatic field between the ALA and the negative lens are plotted in Figure 5-1.b. The negative lens effect and the micro-aperture-lens effect are established by setting electrode 4 to a higher voltage than electrode 3. The MBS projects the 100 virtual source images in the principal plane of the field lens, which will be demagnified by the standard optics of a scanning electron microscope (SEM) to get sub-10 nm spots on the wafer. A multi-beam blanker array (BA) is required for the individual control of each beamlet created by a current limiting aperture. The deposition pattern is defined by the multi-beam blanker array and a blanking aperture placed at a crossover further down in the SEM column, in which the MBS is mounted.

In this paper, we present an integrated multi-electron-beam blanker array, to be used in the MBS for sub-10 nm EBID. The integrated blanker array comprises a CLAA, a BA and a ALA, generating 100 individually controlled, focused beamlets from the diverging beam emitted by a Schottky source. The integrated blanker array is carefully designed to reduce crosstalk, charging and contamination. Key fabrication processes are developed. The first chips will be tested in the MBS module.

5.2 Design of the Integrated Blanker Array

According to the system requirements of the MBS, the 10-by-10 multi-beam blanker array is arranged in a pitch of 80 μm , well aligned to the CLAA and the ALA. Each micro-blanker is capable of providing a beam deflection angle of 2 mrad with an on-off switching frequency of 260 kHz. Since the blankers are not in a conjugate plane of the crossovers on the sample, it is important to have very low crosstalk because it will influence the beam position. An angular error of 1% of the full 2mrad deflection angle makes a shift of 33 nm in the foci plane. If the reduction optics has a magnification of 1/100, the shift is 0.33nm at the wafer. The wiring crosstalk can be reduced by high speed blanking. The angular

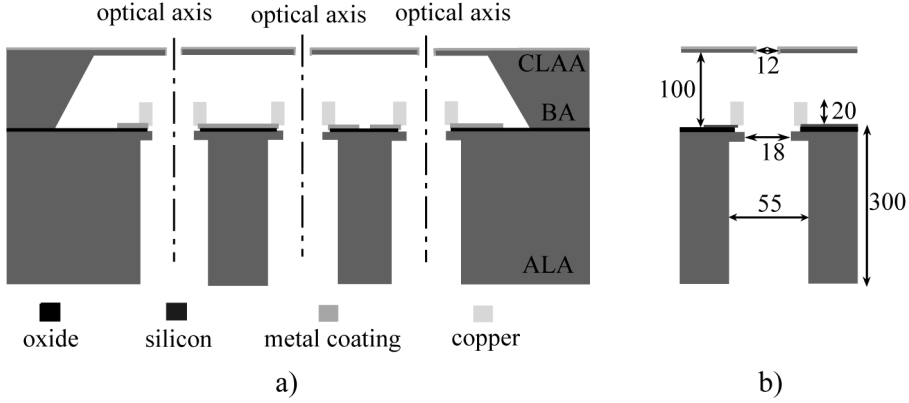


Figure 5-2: a) Schematic of the integrated multi-electron-beam blanker array, from top to bottom CLAA, BA and ALA. b) Dimensions of the integrated blanker array in microns.

error due to static crosstalk, charging and contamination should be minimized less than 1% of the full 2 mrad deflection angle.

To avoid large mechanical misalignment between CLAA, BA and ALA afterwards in the setup, these three arrays are integrated into one part and placed between the collimator lens and the negative lens. Because the aperture lens effect and the negative lens effect are established by the electrical field between the aperture lens plate and the negative electrode, there are two options regarding the integration sequence: BA-CLAA-ALA or CLAA-BA-ALA. The first option is similar as the blanking aperture array proposed by Yasuda [5.3], which has the advantage of fabrication simplicity, but suffers from charging, contamination and crosstalk. The second option offers good device performance: 1st, the crosstalk is dramatically reduced with the grounded CLAA plate above the BA; 2nd, since the blanker plate is protected by the CLAA plate, the contamination and charging are attenuated; 3rd, the thickness of the aperture plate is in the order of microns, a layer of metal with good conductivity may be used to cover the CLAA plate to reduce charging and contamination in the apertures. However, the difficulty is in the bonding process of three components: high alignment accuracy is needed to prevent off-axis aberrations in the aperture lenses.

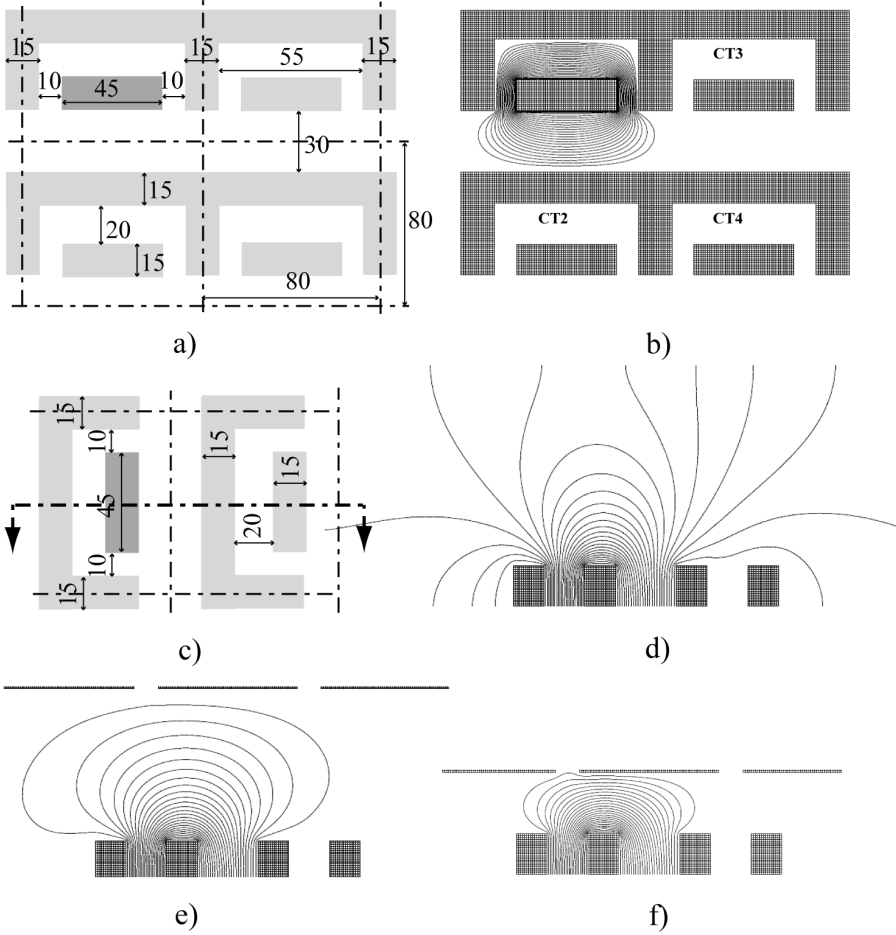


Figure 5-3: a) Dimensions of the blanker electrodes (microns); b) simulation result of in-plane crosstalk; c) the cross-section where out-of-plane crosstalk is observed; d) simulation result of the out-of-plane crosstalk; e) simulation result of the out-of-plane crosstalk with the grounded CLAA plate at 80 μm away from the blankers; f) simulation result of the out-of-plane crosstalk with the grounded CLAA plate at 30 μm away from the blankers.

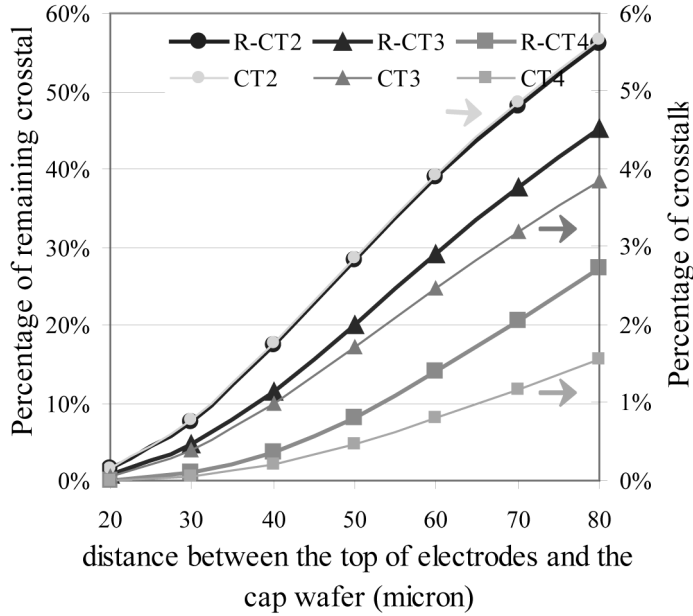


Figure 5-4: The percentage of remaining crosstalk and percentage of crosstalk due to the presence of the grounded CLAA plate above BA.

The schematic of the integrated multi-electron-beam blanker array is shown in Figure 5-2.a. The BA and ALA are fabricated on a 300 thick wafer, while the CLAA is fabricated on a 100 μm thick cap wafer. The electrodes are electroplated copper with 20 μm in height. The detailed dimensions of the integrated blanker array are shown in Figure 5-2.b. The CLAA plate, ALA plate and the grounded electrodes are at 2 kV and a blanking voltage of 8 V is applied to the blanking electrode when the blanker is on.

Great care should be taken in minimizing the electrostatic crosstalk. The crosstalk can be categorized as in-plane crosstalk due to fringing fields extending from the sidewalls of the electrodes, and out-of-plane crosstalk due to fringing fields extending from the top of the electrodes. The dimensions of the blanker electrodes are shown in Figure 5-3.a. The potential contour is plotted in b, where the crosstalk with adjacent

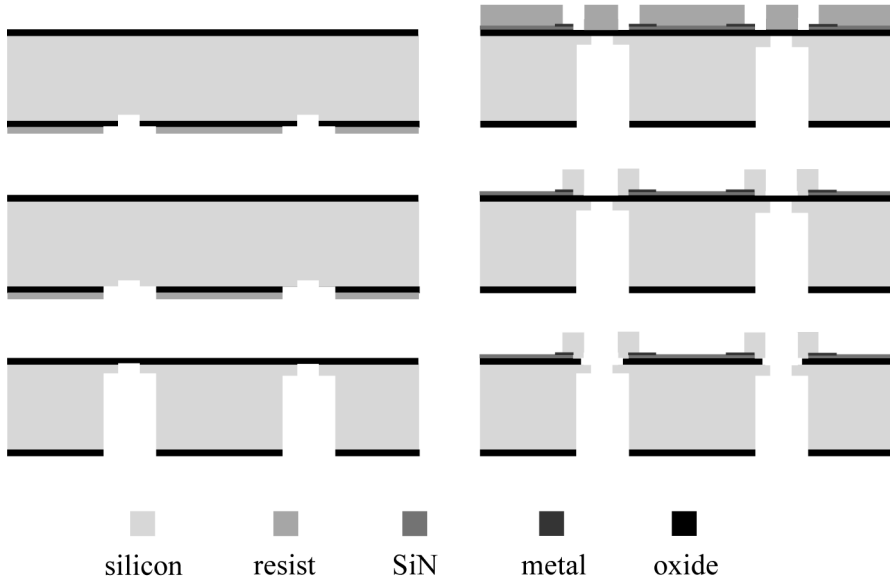


Figure 5-5: The fabrication process for the blanker array and aperture-lens array.

blankers are named as CT2, CT3 and CT4. It can be seen that the in-plane crosstalk is eliminated by the grounded electrodes.

From the cross-section as shown in Figure 5-3.c, the out-of-plane crosstalk without grounded CLAA plate is plotted in d and the out-of-plane crosstalk with a grounded plate at 80 above BA is presented in e. In order to have quantitative data for the total crosstalk of the blankers, a 3D 2-by-2 blanker array with the same dimensions as that in Figure 5-2.a and Figure 5-3.a has been built in a finite element program. The crosstalk is defined as the ratio of the beam deflection angle in the adjacent blanker to the full deflection angle when a blanker is on. When there is no CLAA plate above BA, the crosstalk is 10.1% for CT2, 8.5% for CT3 and 5.7% for CT4.

By placing a grounded CLAA plate above the electrodes, the crosstalk can be further reduced. The ratio of the remaining crosstalk to the original crosstalk when there is no grounded CLAA plate is plotted in Figure 5-4 as a function of the distance between the top of the blanker

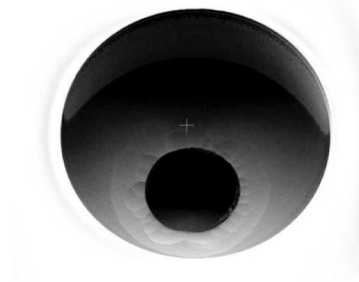


Figure 5-6: The top view of the double aperture plate.

electrode and the cap wafer. The percentage of crosstalk is also shown in Figure 5-4: the crosstalk is below 1% for CT2 when the distance is smaller than 33 μm , which implies either using an extra-thin cap wafer or defining a cavity in the bottom wafer where the cap wafer is located.

For the first test chips, a 100 μm thick cap wafer is used and the crosstalk is expected to be around 5.6% for CT2, 3.8% for CT3 and 1.6% for CT4.

5.3 Fabrication

The first test chips are under fabrication, in which the 10-by-10 blankers in a pitch of 80 are group addressed. The fabrication process of the BA and ALA is shown in Figure 5-5. The process starts with a 300 μm thick boron-doped wafer, with thermal oxide on both sides. The top side of the wafer forms the BA and the bottom side forms the ALA. A two step Bosch process is applied to etch the holes using separate masks for each step, until reaching the oxide on the other side of the wafer. Balancing the etching and passivation is essential for the double aperture plate. The double aperture plate is shown in Figure 5-6.

The wiring of the blankers and the plating base are made of a 200 nm thick Mo-Cu-Ti stack, patterned by a lift-off technique on top of an insulating layer of 500 nm thermal oxide and a patterned layer of 100 nm PECVD nitride. The blanker electrodes are then electroplated using a 26

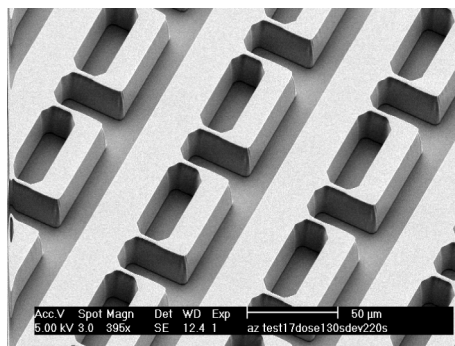


Figure 5-7: The 26 μm thick AZ9260 resist mold for the blanker array.

μm thick plating mold, which is shown in Figure 5-7. The patterned nitride is then used as an etch mask to remove the oxide from surfaces in the vicinity of the electron path.

The CLAA is made from a double side polished 100 μm thick silicon wafer, in which thin Si membranes are made using KOH wet etching. A thick oxide layer is deposited on the bottom to prevent short circuit of the blanker wiring, the CLAA wafer is then bonded to the BA-ALA wafer at 4 corners using a special silver paste, which is ultra-high vacuum compatible.

The current limiting apertures are etched using focused ion beam (FIB), aligned to the BA and ALA through the alignment markers on the bottom wafer, as shown in Figure 5-8.a. A test structure has been made by bonding a 100 μm thick wafer on the bottom wafer, on which metal structures of alignment markers and periodical lines with 100 nm linewidth in a pitch of 5 μm are present. Then the FIB is focused on the bottom wafer, aligned to the markers in the SEM mode. Another set of periodical lines with 100 nm linewidth in a pitch of 4.9 μm is etched on the cap wafer and the bottom wafer. The two sets of periodical lines on the bottom wafer form a vernier structure, from which the alignment error can be determined with a resolution of 100 nm. The vernier structure shown in Figure 5-8.b indicates a misalignment of 200 nm. This alignment accuracy is sufficient to suppress off-axial aberrations in the

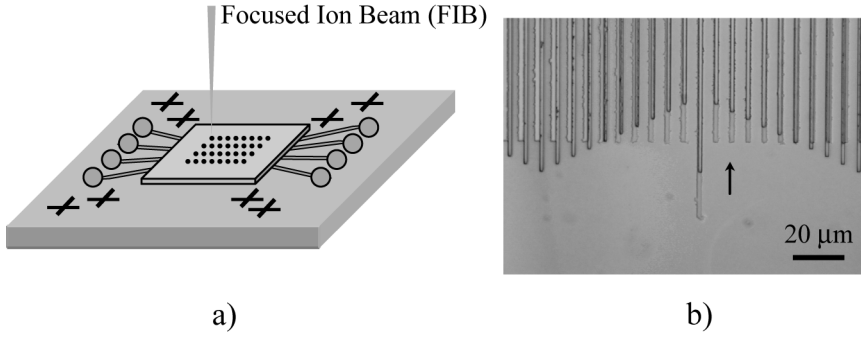


Figure 5-8: a) The current limiting apertures are etched by FIB. The alignment to the blanker array is through the alignment markers on the bottom wafer. b) Vernier structures on the bottom wafer showing the alignment accuracy of approximately 200 nm.

ALA. A 100 μm defocus of the FIB should be taken into account when defining the current limiting apertures.

5.4 Conclusions

In this paper, the design steps for the integrated multi-electron-beam blanker array have been described, showing how the design parameters influence the device performance, especially the crosstalk. The in-plane crosstalk is minimized by guard walls and the out-of-plane crosstalk is reduced by the presence of the grounded CLAA plate. The contamination and charging are reduced due to the fact that the blanker electrodes and lens apertures are protected from direct electron illumination. A proof-of-concept chip with 100 blankers addressed in 6 groups is under fabrication. The double aperture plate is formed by deep silicon dry etching and the blanking electrodes are made by the electroplating. The CLAA is aligned to the BA with an accuracy of 200 nm.

Reference

- [5.1] H. Yasuda, S. Arai, J. I. Kai, Y. Ooae, T. Abe, S. Maruyama, and T. Kiuchi, *J. Vac. Sci. Technol. B* 14, 3813 (1996).
- [5.2] E. Yin, A. D. Brodie, F. C. Tsai, G. X. Guo, and N. W. Parker, *J. Vac. Sci. Technol. B* 18, 3126 (2000).
- [5.3] H. Yasuda *et al.*, *Jpn. J. Appl. Phys.* Vol. 32, 6012 (1993).
- [5.4] G. Winograd, V. Krishnamurthi, R. Garcia, L. H. Veneklasen, M. Mankos and F. Pease, *J. Vac. Sci. Technol. B* 18, 3052 (2000).
- [5.5] I. L. Berry, A. A. Mondelli, J. Nichols, and J. Melngailis *J. Vac. Sci. Technol. B* 15, 2382 (1997).
- [5.6] G. W. Jones, S. K. Jones, M. D. Walters, and B. W. Dudley, *IEEE Trans. on Electron Devices*. Vol. 36, No.11, 2686 (1989).
- [5.7] M. J. Van Bruggen, B. van Someren, and P. Kruit, *J. Vac. Sci. Technol. B* 23, 2833 (2005).

Chapter 6

Experiments towards a High Brightness 100-electron-beam Source

Poster presentation at 52nd International Conference on Electron, Ion, and Photon Beam Technology and Nanofabrication (EIPBN).

In this chapter, we report the experimental results towards a working high brightness 100-electron-beam source. Three different multibeam source designs have been presented in chapter 2, 3 and 4. A multibeam source designed with the same principles as that in chapter 4, but with a maximum acceleration voltage of 12 kV is chosen for experiments. The optical column operates at lower voltages. It demands a smaller electric field between the electrodes and thus has less stringent precautions on electric breakdown. The configuration of the multibeam source is described in section 6.1. This multibeam source requires a high-brightness Schottky emitter working at a low extraction voltage. The experiment of a miniature low power Schottky emitter is reported in section 6.2. The optical components are microfabricated. The process of microfabrication and the alignment between the optical components are presented in section 6.3. The results are analyzed and challenges towards a working 100-beam-source are discussed. The blanker array fabrication is briefly reported in section 6.4.

6.1 The Multibeam Source for Experiments

Three different multibeam source designs have been described in chapter 2, 3 and 4 individually. The designs in chapter 2 and chapter 3 are intended for massively parallel electron beam lithography. These two designs are limited by three factors: 1) the multibeam source should be capable of being stacked in a closely packed array with a pitch of 1.5 mm to generate tens of thousands of electron beams; 2) the outermost beams from two adjacent multibeam units should have the same distance as the beam pitch within one unit; and 3) these beams can be collimated by a deflector array at the conjugate plane of the electron source, therefore, the beam potential at the deflector array should be low enough so that the required deflection voltage is less than 15 volts. The configuration in chapter 2 is simpler in terms of microfabrication and alignment, while the design in chapter 3 offers better system performance due to smaller aberration coefficients of the aperture lenses. Despite the fact that these two designs fulfil the system requirements of delivering high brightness beams with high total current, the closely packed Schottky emitter array of 1.5 mm pitch with high position stability is unsubstantial: the typical lateral position stability of a commercial Schottky emitter is around 5 μm , while the Schottky emitter array requires each emitter to have a lateral stability of 250 nm; the vertical shift of a commercial Schottky emitter is not specified in a single column system, because it can be easily compensated by re-focusing, however, a vertical stability of 100 nm is required for the emitter array. Apart from this extremely high stability requirement, the closely packed multibeam units face serious engineering challenges, such as fine alignment, high electric field, tight thermal control of the emitters, etc. Coulomb interactions may be another concern because high currents are travelling together and the beams are decelerated to a few hundreds volts at the blanker array.

Instead of being stacked in an array, both these two designs can work as a single unit to generate 100 beams. A multibeam source designed with the same principles as that in chapter 3, but using a Schottky emitter at an extraction voltage of 5 kV, has been presented for generating

multiple electron beams to increase the throughput of electron beam induced deposition [6.1].

In chapter 4, a multibeam source is presented for high resolution applications. When emerging from the multibeam source, the beams are not necessarily parallel, and the design is not limited by the closed-packing requirement. Therefore, this multibeam source has the following superior properties: 1) the broad beam travels at 4 keV before reaching the aperture lens array, and the sub-beams are accelerated towards the blanker array, therefore, the Coulomb interactions are smaller compared with the previous designs; 2) a macro deflector can be put between the emitter and the aperture lens array to correct emitter position shifts without influencing the functionality of other optical components; and 3) higher beam potential at the conjugate plane is easier for imaging, while complicated image amplifier or MCP (multi-channel plate) are necessary in the previous designs where the beam potential is below 1000 eV. As the previous designs, the multibeam source in chapter 4 suffers from high electric fields between electrodes, but this can be conveniently avoided by lowering the extraction voltage.

TABLE 6-1: The optical performance of the multibeam source for experiments.

Beam half opening angle (mrad)	4
Filling factor	62.5%
Potential at objective side (V)	1000
Potential at image side (V)	8000
Magnification	-7.0
Angular magnification	-0.05
C_s at image side (mm)	1.8 E7
C_c at image side (mm)	1.8 E3
FW_s 50 (nm)	26.7
FW_c 50 (nm)	7.6
Central spot size (nm)	255
Angular current density (mA/sr)	0.2
Beamlet current (nA)	10.05
Total current (nA)	1005

Therefore, a multibeam source designed with the same principles as that in chapter 4, but with a low extraction Schottky emitter, is preferred for experiments. The low extraction voltage allows operating the optical column at lower voltages. The highest potential of the optical column is limited by the maximum voltage of the feed-through connectors in the test setup, i.e., 12 kV. The optical properties of this multibeam source are listed in Table 6-1. The extraction voltage is set at 1000 volts and the distance between the tip and the extractor is reduced accordingly to maintain a sufficiently high electric field at the tip apex. Note the objective distance is reduced to 1.2 mm to limit the Coulomb interactions. The optical column magnifies the virtual source by a factor of -7. Assuming a virtual source size of 36.5 nm, the spot sizes expected at the YAG screen is 255 nm. This is easier for detection than the one-to-one magnification in chapter 4. The spherical and chromatic FW50 disks are much smaller compared to the geometrical source size, and higher fillings of the aperture lens are possible. However, considering that the lens holes are not perfectly round and may induce higher order aberrations, the filling factor is kept to 62.5%. A beamlet current of 10 nA is calculated assuming an angular current density of 200 $\mu\text{A/sr}$. The assumptions of the virtual source size and the angular current density result in a brightness of approximate $1.5 \times 10^8 \text{ A/m}^2\text{srV}$.

TABLE 6-2: The dimensions and potentials of the multibeam source for experiments.

component	Lens radius (mm)	Electrode Thickness (mm)	Potential w.r.t. the ground (V)	Distance to the tip (mm)
Emitter	-	-	-8000	0
Extractor	0.08	0.2	-7000	0.1
Aperture lenses	0.008	0.02	-7000	1.25
Accelerator electrode 1	0.8	0.2	-6800	1.45
Accelerator electrode 2	1.2	0.3	0	2.35
YAG screen	-	0.1	0	19.29

The configuration of the multibeam source for testing is listed in Table 6-2. The potentials of the source and optical elements are raised negatively with respect to the ground by high voltage power supplies. The second accelerator electrode and the YAG screen is biased at ground potential. This optical configuration will be tested in a UHV setup. The performance of the multibeam source will be evaluated by measuring the beam sizes and the probe currents using knife-edges on a YAG screen. The results of the experiment will give insight not only in the multibeam source performance, but also in the off-axial performance of the Schottky emitter.

The experimental results with low power Schottky emitter are presented in section 6.2. The fabrication and alignment of the optical components are illustrated in section 6.3. Several issues regarding the microfabrication and experiments are discussed. A brief update of the blanker array is described in section 6.4.

6.2 Low Power Schottky Emitter

The input power required to heat a standard Schottky emitter to 1800 K is substantial. It is typically larger than 2 Watts. In the multibeam source, the extractor plate and aperture lens electrode are very close to the emitter and impinged by high current. Elevated temperatures on these electrodes result in thermal stress, which may cause electrode deformation, rupture of the metal coating or even thermally induced misalignment. For a multibeam source, where multiple emitters are used, the heat conducted and radiated from the emitters may raise the overall system temperature to an unacceptable level. Therefore, low power Schottky emitters (LPSE) are preferred. Miniature low power Schottky emitters investigated by Kim [6.2] present promising results: for an emitter with a tip radius of $0.8\text{ }\mu\text{m}$ and a tip-extractor distance of $200\text{ }\mu\text{m}$, the angular current density reaches $100\text{ }\mu\text{A/sr}$ when the extraction voltage is around 2500 volts. To meet the assumptions, a brighter source with higher I' at low extraction voltage is preferred. In our experiment, we use the miniature low power Zr/O/W(100) Schottky emitter with a suppressor electrode and heating filaments, as shown in Figure 6-1. The



Figure 6-1: left, a standard Schottky emitter with a suppressor electrode (sitting in its holder inside the glass cap), the diameter of this source is 17 mm; right, a miniature low power Schottky emitter with a suppressor electrode (sitting in its holder inside the glass cap), the diameter of this miniature source is 4 mm.

extractor is a silicon electrode with a 80 μm diameter hole. By bringing the emitter closer to the extractor, the extraction voltage can be lowered without much influencing in the reduced brightness. The emission current and emission pattern are recorded and analyzed. The experimental setup is described in section 6.2.1. The microfabrication of the extractor electrode is reported in section 6.2.2. In section 6.2.3, the result is presented and analyzed. Finally, some issues are discussed in section 6.2.4.

6.2.1 The Experimental Setup

Figure 6-2 shows the schematic of the experimental setup. It consists of a base vacuum chamber and a six-cross upper vacuum chamber. One side port of the six-cross is connected with a manual valve, a turbo molecular pump and a pre-vacuum pump. The manual valve is closed when the pressure in the chamber is reaching the ultimate pressure of the turbo pump. The getter ion pump (GIP) and titanium sublimation pump

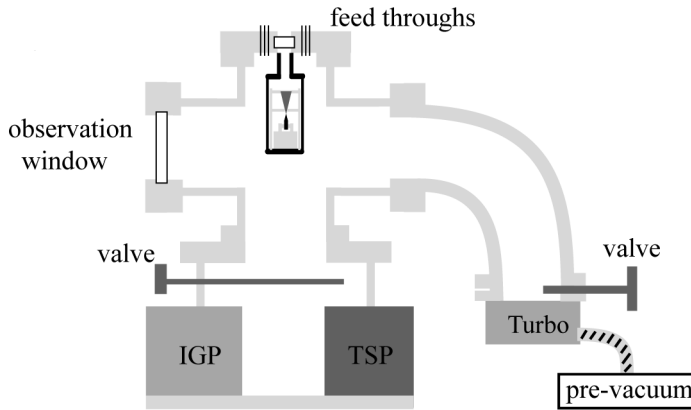


Figure 6-2: Schematic overview of the experimental setup.

(TSP) are installed in the base chamber, separated by a manual valve from the upper chamber. This valve is closed to keep the base chamber at vacuum when venting the upper chamber.

The optical column is mounted on a four-pillar stage and attached to a CF150 flange on the top port of the six-cross vacuum chamber. The feed-throughs, including three 7-pin connectors, three 4-pin connectors, are also welded to this flange. In the center of this flange, there is an observation window fixed by a CF40 flange. The light coming from the YAG screen transmits through the observation window and is recorded by a CCD camera outside the vacuum chamber. The detailed mechanical drawing is shown in Figure 6-3. This entire optical stack can be observed from another side-port of the six-cross chamber, as shown in Figure 6-2.

Figure 6-4 shows a photo of the optical column on the mounting flange. The 3-axis nano-positioning piezo stage is fixed to the top plate. For each axis, a voltage ranging from -20 volts to 130 volts can be applied, which creates a motion of up to 100 μm in open-loop, or 80 μm in closed-loop operation. The closed-loop system overcomes the effect of hysteresis and drift so that the piezo stage does not contribute to the tip position shift. The LPSE is clamped by the tip holder and they are

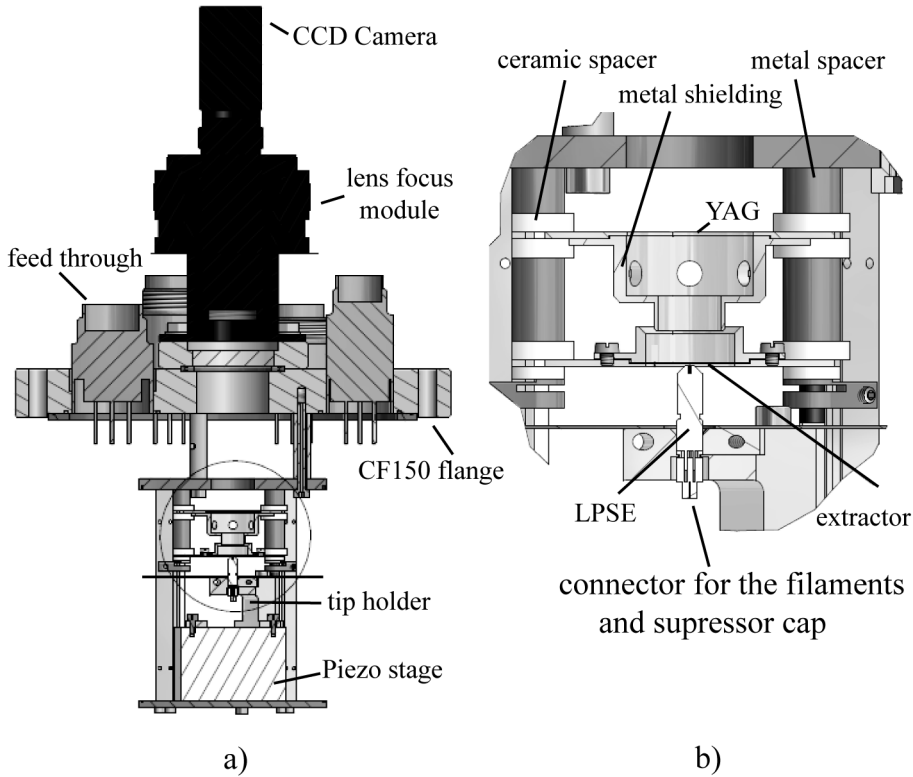


Figure 6-3: a) The detailed mechanical drawing of the experimental configuration, including the optical lens and CCD camera outside the vacuum, the flange with feed-throughs, and the optical column inside the vacuum chamber; b) the zoom-in drawing of the optical column.

attached to the piezo stage through precision pin holes. The tip radius is $0.55\text{ }\mu\text{m}$. Opposite to the emitter at around $300\text{ }\mu\text{m}$ is the microfabricated extractor. The YAG screen is 20.3 mm away from the tip. The schematic presentation of the optical column is shown in Figure 6-4.b. This optical column is put inside the ultra high vacuum chamber, which has a background pressure of $5 \times 10^{-11}\text{ mbar}$. The emitter is controlled with a

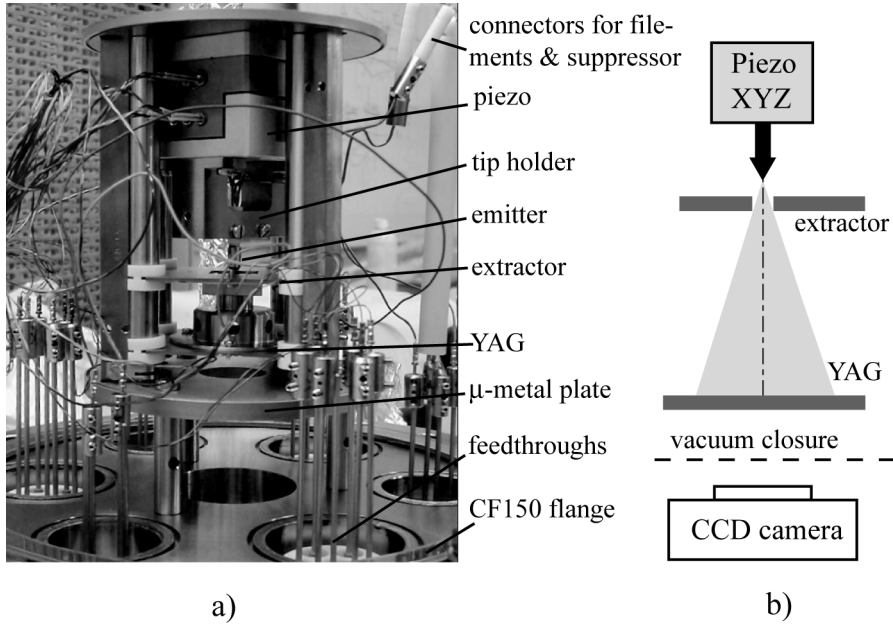


Figure 6-4: a) Photo of the optical column on the mounting flange; b) the schematic presentation of the optical column.

field emission gun supply unit (FGSU) which is raised to a negative potential using a Heinzinger high voltage supply. The extractor and YAG are biased at ground potential. The current falling on the extractor, and the current coming through the extractor hole which is collected by the YAG screen and the metal shielding, are recorded.

6.2.2 Microfabrication of the Extractor Electrode

The extractor electrode is fabricated at the DIMES class 10,000 clean room. The fabrication process flow is illustrated in Figure 6-5.a. The process starts with a 200- μm thick double-side polished *p*-type silicon wafer. The wafer is thermally oxidized to get a 1300 nm SiO_2 film. It is subsequently spin-coated with HMDS and e-beam resist (ZEP 520). HMDS promotes adhesion between the oxide and the resist. The resist is then exposed by an electron beam pattern generator (EBPG 5000) with a

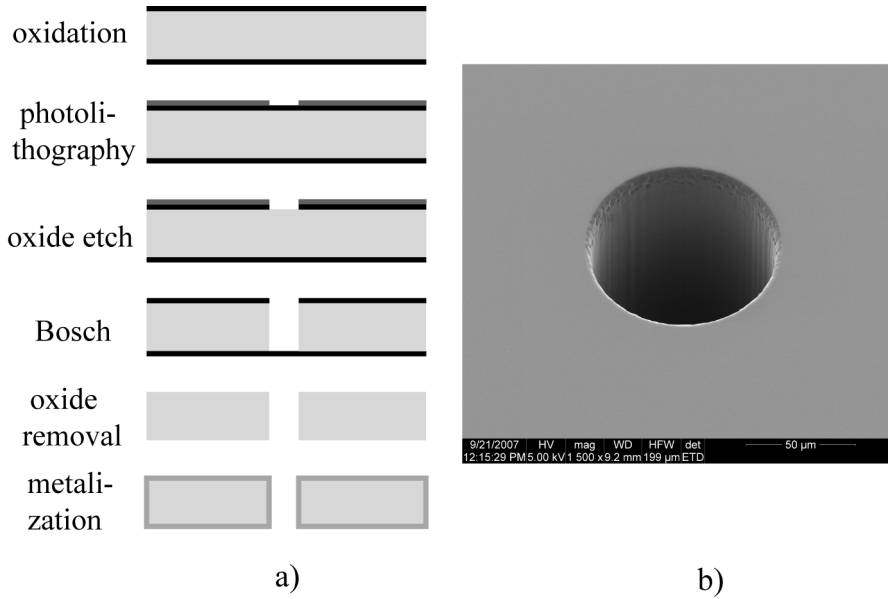


Figure 6-5: a) Schematic overview of the extractor fabrication process flow; b) SEM picture of the extractor hole.

dose of $300 \mu\text{C}/\text{cm}^2$. After development, the oxide is dry etched with the patterned resist serving as etch mask. The resist is then stripped and the extractor hole is etched in a deep silicon dry etching process (Bosch process). The Bosch process is also known as time-multiplexed etching because it alternates repeatedly between a plasma-etching mode and a passivation-deposition mode to achieve nearly vertical structures. The passivation layer, a substance similar to teflon, condensates on the sidewalls and protects them from lateral etching. The oxide mask is then removed, and the wafer is cleaned with oxygen plasma and wet etching to remove the passivation layer. Finally, the extractor electrode is sputter-coated with 20 nm Cr adhesion layer and 200 nm Mo. A SEM picture of the extractor electrode is shown in Figure 6-5.b.

6.2.3 Experimental Results

The low power Schottky emitter is started up by applying the filament current in several steps via FGSU until it reaches 0.74 A. This filament current approximately equals to a tip operating temperature of 1800 K. To reduce the undesired thermionic emission from the shank, the suppressor voltage is set at minus 200 volts with respect to the emitter. The tip is positioned by the 3-axis Piezo stage, where X- and Y-axes are used to align with the extractor, and the tip-extractor distance is adjusted

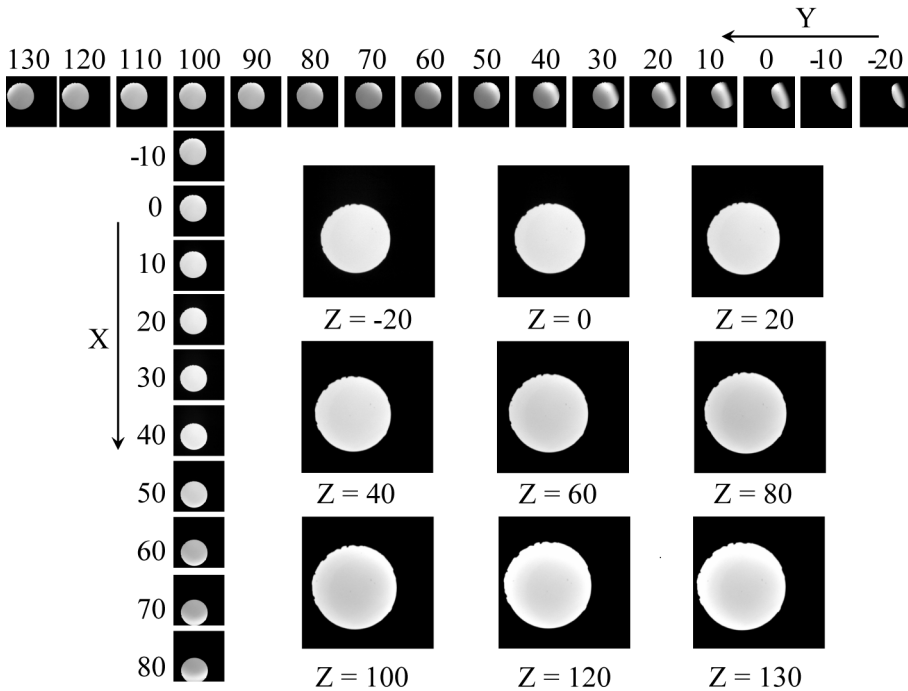


Figure 6-6: A typical alignment process as a function of piezo voltages on the X-, Y-axes. When the emitter is aligned, the emission pattern is recorded with different tip-extractor distances by applying different piezo voltages on the Z-axis. 10-Volts change in the Piezo voltage equals to $6.67 \mu\text{m}$ position shift.

by the Z-axis. During the alignment, the piezo stage operates in open-loop system. The potential of the Z-axis is kept at -20 volts, which results in the maximum tip-extractor distance to prevent damage to the emitter. The extraction voltage is approximately 3300 volts to obtain a clear emission pattern with “dog ears”. A typical alignment process is shown in Figure 6-6. By scanning the emitter via one axis, the edges of the emission pattern - the “dog ears”- are found and the center of the emission pattern along this axis is determined as the middle of two “dog ears”, assuming the emission pattern is symmetric. A good alignment is achieved when the center of the emission pattern is recorded. Once the emitter is aligned, the distance between the emitter and the extractor can be decreased via the Z-axis. As the tip-extractor distance becomes smaller, the total current rises due to a stronger electric field at the emitter. At the same time, the aperture angle becomes larger, thus the emission pattern recorded becomes bigger, and the emission profile changes from a uniform disk to a disk with a brighter ring, as shown in Figure 6-6.

The experimental plots of the total current, and its two components - the extractor current and YAG current are shown in Figure 6-7 for a tip-extractor distance of around 300 μm in a) and 200 μm in b). The YAG current is the emission from the central, low work function (100) facet. The extractor current consists of the emission from the four (100) planes along the emitter shank and part of the emission from the central facet (the outer portion of the facet). The relative contribution of the YAG current to the total current, as shown in Figure 6-7.c, increases with the extraction voltage because the electric field at the central facet is much higher than that along the emitter shank. This means that the central facet emission transits into a more field-dependent, extended Schottky emission regime at a lower value of V_e than does the emission from the shank [6.3]. The higher slope of the YAG contribution curve at smaller tip-extractor distance can be explained by a larger field enhancement factor as defined in Eq. (1-4), thus a higher electric field at the tip apex. The emission transits quickly into the extended Schottky emission regime, where the emission is magnified by the term of $\pi q / \sin(\pi q)$ as indicated in Eq. (1-5).

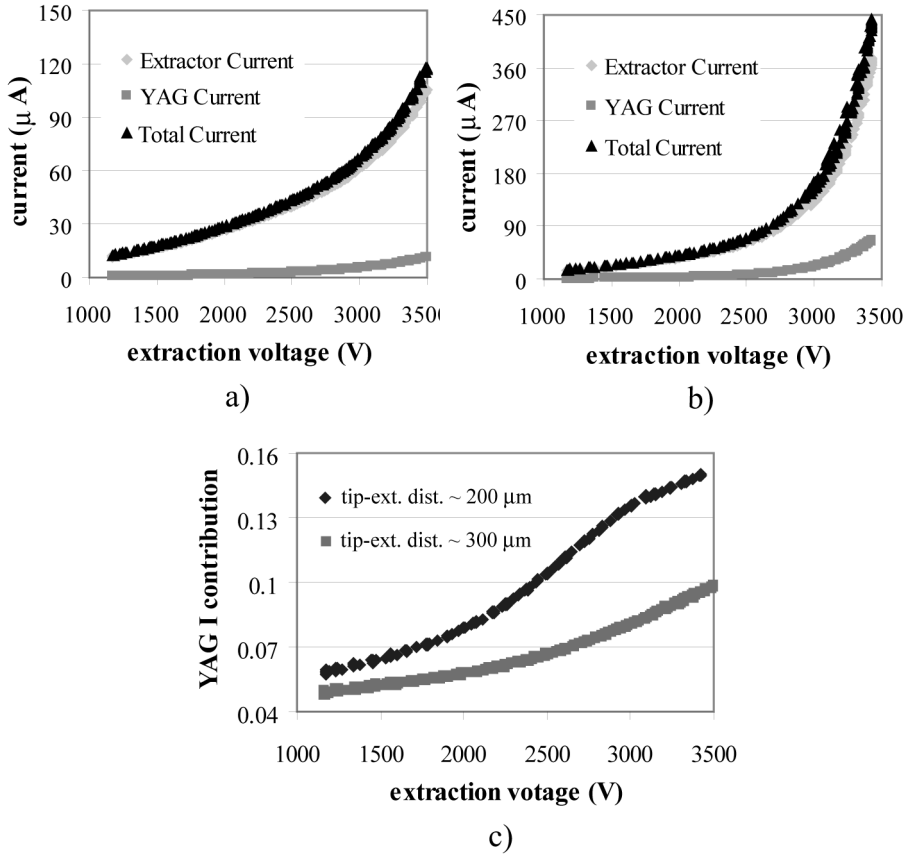


Figure 6-7: Experimental plots of the total current, extractor current and YAG current versus the extraction voltage, with a tip-extractor distance of a) $300\text{ }\mu\text{m}$; b) $200\text{ }\mu\text{m}$; c) the relative contribution of the YAG current to the total current.

The YAG current is plotted versus the extraction voltage for different piezo voltages on the Z-axis, as shown in Figure 6-9.a. The Schottky plot is shown in Figure 6-9.b. The experimental data deviate from the straight-line Schottky plot at the upper end of the data range because the emission mechanism crosses the boundary separating the Schottky emission and extended Schottky emission. The assumed angular current

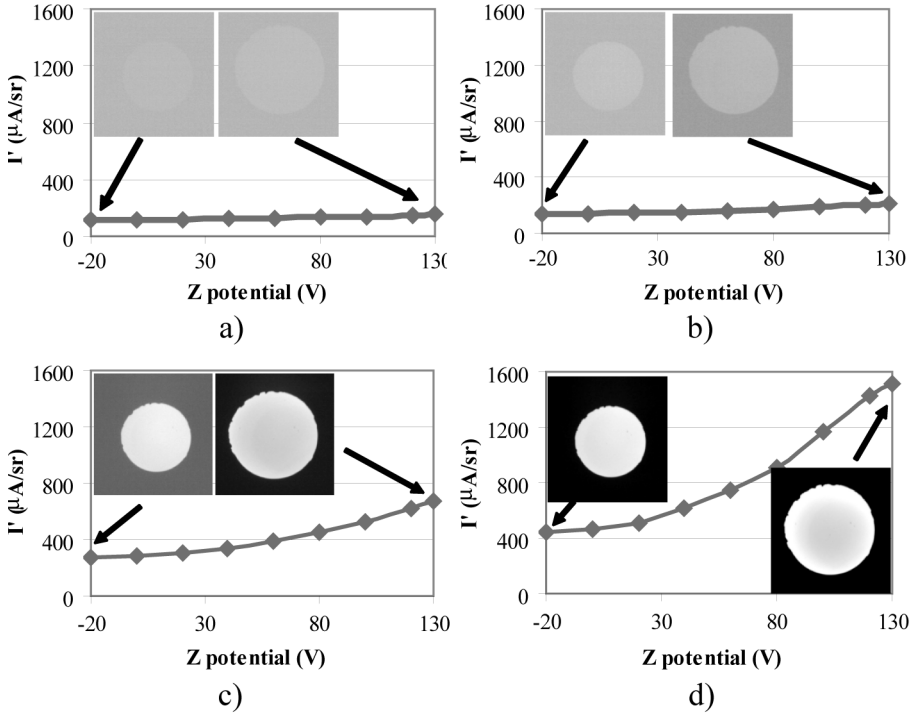


Figure 6-8: Angular current density versus the piezo voltage on Z-axis, with an extraction voltage of approximately a) 2230 volts; b) 2400 volts; c) 3000 volts; and d) 3300 volts. The emission patterns at V_z of -20 volts and 130 volts are present.

density of 200 $\mu\text{A}/\text{sr}$ is indicated by the dashed line. It can only be reached at an extraction voltage of 2380 volts or higher.

In Figure 6-8, the emission pattern is recorded when the tip-extractor distance is reduced and the extraction voltage is fixed. When the extraction voltage is 2230 volts, the angular current density increases from 114 $\mu\text{A}/\text{sr}$ to 152 $\mu\text{A}/\text{sr}$ by reducing the tip-extractor distance from 300 μm to 200 μm . The emission pattern is hardly seen because only a few microampere current falls on the YAG screen and the beam potential is low. At higher extraction voltages, the angular current density

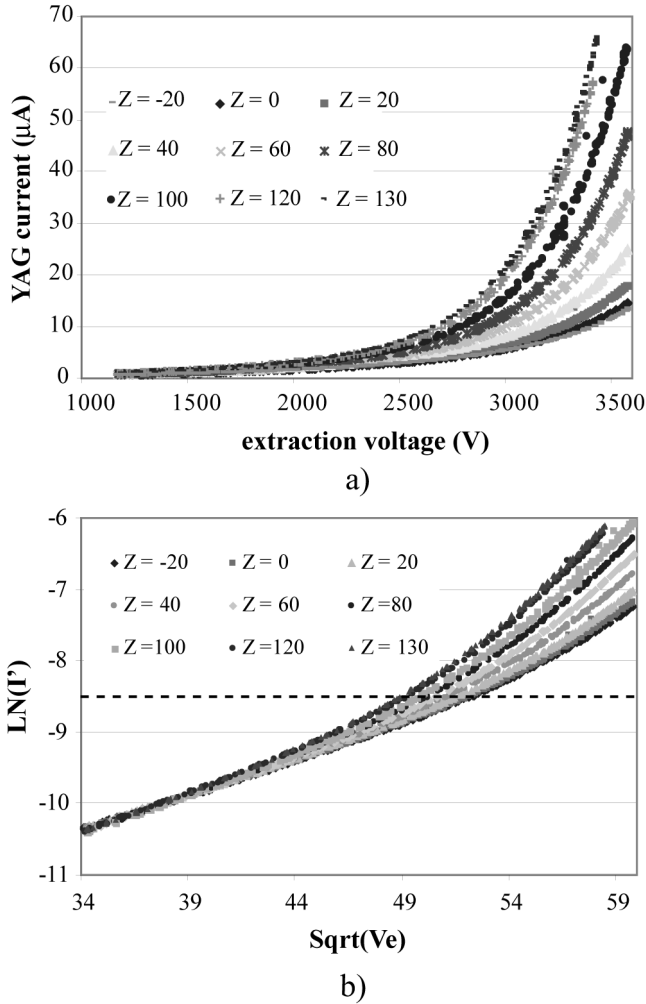


Figure 6-9: The experimental plots for different piezo voltages on Z-axis, a) The YAG current; and b) Schottky plots where the dash line indicates an angular current density of $200 \mu\text{A}/\text{sr}$.

increases much faster with reducing the tip-extractor distance. Higher contrast emission patterns are obtained because of the higher current and

higher electron energy. The defective roundness in the extractor hole becomes more apparent in the emission pattern.

6.2.4 Discussions and Summary

In the experiment with the low power Schottky emitter, the alignment process between the emitter and the extractor electrode are demonstrated with the 3-axis piezo stage. Emission patterns are recorded, as well as the current falling on the extractor electrode and the YAG screen. High angular current density at low extraction voltage is achieved by bringing the emitter closer to the extractor hole. However, the angular current density is lower than the assumed value. The recorded output of the high voltage supply has a large noise level. And the emission patterns reveal defects in the extractor hole. These issues will be discussed.

6.2.4.1 The Angular Current Density

It is clear from Figure 6-9 that the assumption we made in section 6.1 - 200 $\mu\text{A}/\text{sr}$ at an extraction voltage of 1000 volts - cannot be achieved with this emitter at the shortest tip-extractor distance of 200 μm . Instead, at a 200 μm tip-extractor distance, an extraction voltage of 1000 volts, and a suppression voltage of -200 volts, the angular current density is only around 20 $\mu\text{A}/\text{sr}$. By reducing the suppressor voltage, or increasing the filament current, a higher angular current density can be achieved. For example, raising the tip temperature to 1825 K (by changing the filament current from 0.74 A to 0.76 A) and decreasing the suppressor voltage to -55 volts, the angular current density increases to 40 $\mu\text{A}/\text{sr}$. However, the filament current is limited by the maximum tip operating temperature (around 1850 K). At higher temperatures, the ZrO reservoir evaporates quickly and the lifetime reduces. At 1900 K, the lifetime of the emitter is around 10% of the standard value. Decreasing the suppression voltage further causes the shank emission to increase drastically, which is not desired either.

Alternatively, the angular current density can be enhanced by creating a higher electric field at the tip apex. This may be achieved by reducing the tip-extractor distance, or replacing the current LPSE with one having smaller tip radius. For example, with a LPSE of 0.27 μm tip-radius at 100

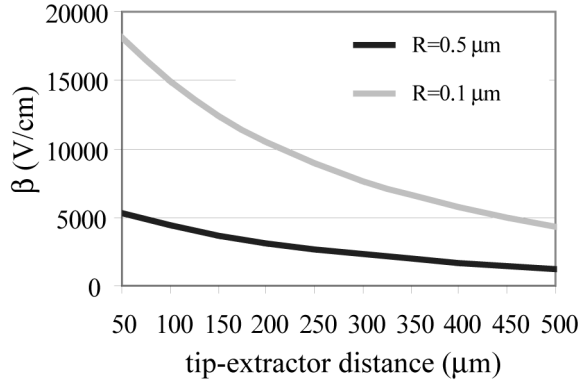


Figure 6-10: Field enhancement factor versus tip-extractor distance for emitters with different tip radius ($V_e = 1000$ volts, $V_s = -300$ volts).

μm tip-extractor distance, the angular current density is 130 μA/sr at 1000 volts [6.4]. The electric field at the tip apex is related to the tip radius and the tip-extractor distance by the field enhancement factor, which can be calculated using Eq. (1-4). The field enhancement factor for different tip-extractor distances and tip radii is plotted in Figure 6-10. By reducing the tip-extractor distance from 200 μm to 100 μm, the β rises by a factor of approximately 1.4. For an emitter with tip radius of 0.1 μm, β is around 3.8 times larger than that for one of 0.5 μm radius. However, emitters with smaller tip radius have smaller virtual source size. This may lead to difficulties in probe size measurements. And reducing the tip-extractor distance increases the chance of collision between the emitter and extractor.

In fact, the low angular current density is the result of a low electric field at the tip apex. And it indicates that the electron source is working at a lower brightness than the assumed 1.5×10^8 A/m²srV. The consequence of a lower-brightness source is that the probe current on the YAG screen is smaller and the probe sizes are larger due to a larger virtual source size. But it does not change the optical properties of the multibeam source, such as the magnification, axial and off-axial aberrations. When the angular intensity is 20 μA/sr, the current density in a focused probe is

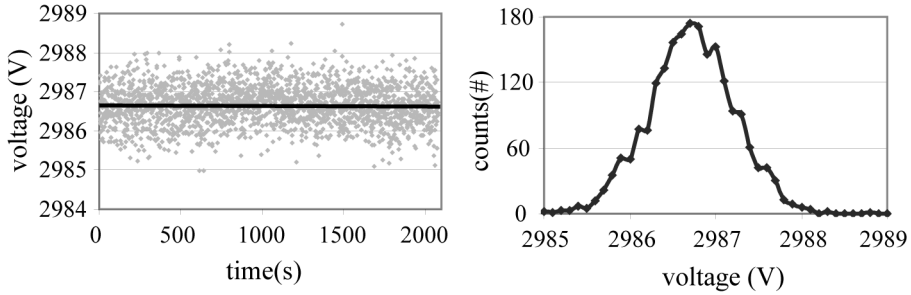


Figure 6-11: a) The recorded voltage versus time; b) the histogram of the voltage.

much higher than that of the shadow emission pattern at $I' = 1500 \mu\text{A/sr}$ ($V_e = 3300 \text{ V}$). Furthermore, the potential of the focused probe is around 8000 volts. Thus at $20 \mu\text{A/sr}$, high contrast images of the multiple probes can be obtained and high signal-to-noise knife edge measurements can be achieved. Therefore, a lower-brightness source does not harm the objectives of the experiments, i.e. to evaluate the multibeam performance and to acquire insight into the off-axial performance of the Schottky emitter by comparing the axial and off-axial probe sizes and probe currents.

6.2.4.2 High Voltage Supply

A Heinzinger high voltage supply is used to raise the potential of the emitter negatively with respect to ground. The output of the high voltage supply is monitored every 3 seconds. These data points and the histogram are plotted in Figure 6-11. As shown, the stability of the high voltage is around 0.07%.

The instability of the power supply could be a serious problem in the case of the multibeam experiment, where 3 high voltage power supplies are necessary, as listed in Table 6-2. If each power supply has a potential variation of ± 1 volts, the worst case scenario results in a spotsize growth of 95 nm over the nominal value due to overfocus or defocus. Moreover, the instability of the power supplies causes lateral position instabilities for the off-axial beamlets. Instable probe positions create

difficulties for knife edge measurements. For the specific multibeam source, the stability of the high voltage power supplies must therefore be improved by two orders of magnitude with respect to the standard FGSU power supply of the Schottky electron source. The same conclusions have been drawn by Van Bruggen [6.1].

6.2.4.3 Microfabrication

Defects in the extractor hole are revealed from the emission patterns illustrated in Figure 6-6 and Figure 6-8. The sizes of the defects can be calculated from the emission patterns. The unroundness as indicated in Figure 6-12.a is due to a defect of approximately $2.8\ \mu\text{m}$. These defects could be at the edge or in the sidewall of the extractor hole. The defects are revealed by the SEM images in Figure 6-12.b and c. These images are made after teflon cleaning. As shown, part of the teflon layers still remain. The samples are cleaned again and examined in the SEM again. However, due to the limited depth of focus, the middle of the sidewalls cannot be clearly seen. The unroundness in the emission pattern may be due to remaining teflon layers at the middle of the sidewall since it is difficult for the teflon etchant to reach that location.

Apart from the remaining teflon layers, also the irregularities at the edge of the extractor hole contribute to the unroundness of the emission

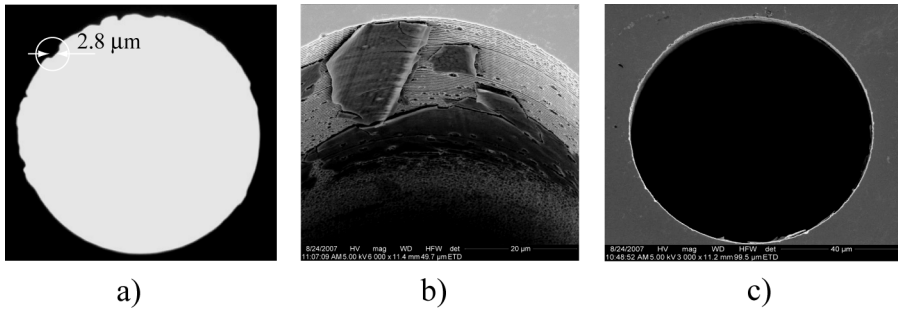


Figure 6-12: a) The recorded emission pattern; b) the sidewall of the extractor hole with teflon layers, and c) the SEM image of the extractor hole with hanging teflon layer at the bottom.

patterns. These irregularities are usually in the order of a tenth of a micron, and they may be due to the oxide etch or Bosch process.

In summary, the oxide dry etch, Bosch process and the teflon cleaning should be improved to make round lens holes. The roundness of the lens holes is essential for the multibeam experiments: the performance of the multibeam source can only be assessed when the blur induced by the lens unroundness is smaller than the aberration disks.

6.2.4.4 Summary

The experiment with LPSE demonstrates the alignment mechanism between the emitter and extractor hole. The performance of the LPSE at low extraction voltage is analyzed. Due to insufficient electric field strength at the tip apex, the emitter is working in the Schottky regime when the extraction voltage is below 2000 volts. This results in lower brightness and lower angular intensity than the assumptions. Fortunately, a lower-brightness source does not jeopardize the goals of the multibeam experiment. The multibeam experiment can be carried on with the current emitter and its operational settings. However, the experiment with LPSE reveals that the quality of the microfabrication, especially the roundness of the lens holes, and the high voltage power supplies must be improved for the multibeam source experiments.

6.3 The Optical Column

Before the multibeam experiment can be conducted, the optical components must be microfabricated, and aligned to each other and to the emitter. The microfabrication is reported in section 6.3.1. Section 6.3.2 presents the alignment and buildup of the optical column. Finally, several issues with regard to the multibeam experiment will be discussed in section 6.3.3.

6.3.1 Microfabrication

The microfabrication process flow chart for the accelerator electrodes is similar to that of the extractor plate as illustrated in Figure 6-5.a,

except different masks will be used in photolithography. The fabrication of the aperture lens electrode is more complex. The process flow is shown in Figure 6-13. The process starts with 200 nm Si_3N_4 deposition using LPCVD (low pressure chemical vapour deposition). In the photolithography process, the mask for KOH etching is patterned into the resist on the backside of the wafer, which serves as the etch mask for the subsequent Si_3N_4 dry etching, as shown in Figure 6-13.c. After the KOH

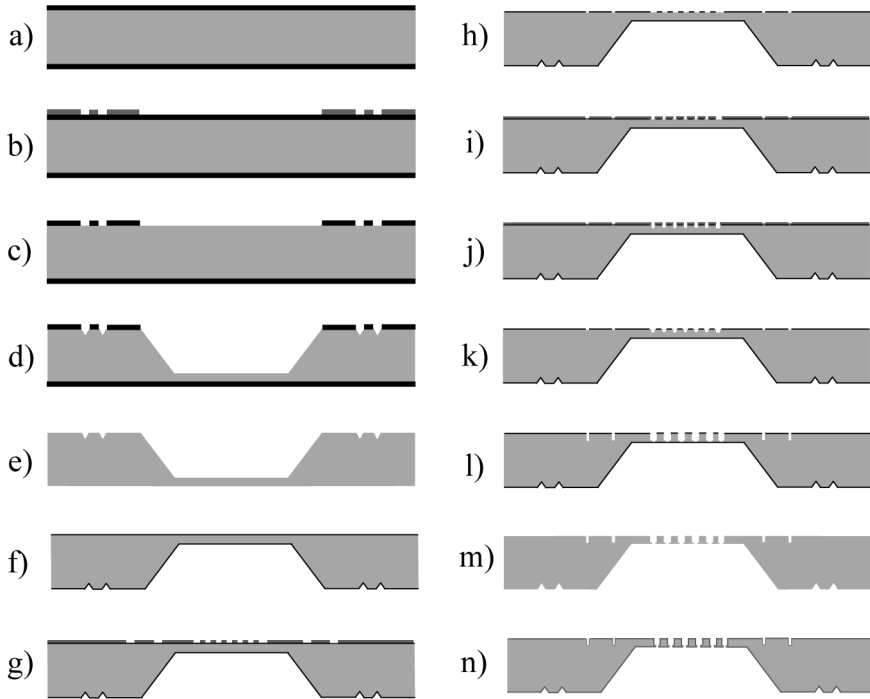


Figure 6-13: The schematic overview of the microfabrication processes for the aperture lens array: a) Nitride LPCVD, b) photolithography, c) Nitride etch, d) KOH etch, e) Nitride removal, f) oxidation, g) photolithography, h) oxide etch, i) photolithography, j) deep silicon dry etch, k) resist strip, l) deep silicon dry etch, m) oxide removal, and n) Mo coating.

etch and Si_3N_4 removal, a 200- μm -thick silicon membrane is formed, on which the aperture lenses will be made. The wafer is then thermally oxidized. The second lithography process is made on the frontside of the wafer, as shown in Figure 6-13.g. This lithography is aligned to the backside pattern with a sub-micron alignment accuracy. This pattern is then transferred to the oxide. In Figure 6-13.i, the third lithography defines the mask for the current limiting apertures. Then the CLAs are etched in the first Bosch process. After resist strip, the aperture lens holes are etched in the second Bosch process, with the patterned oxide as the etch mask. The oxide is then removed, and the wafer is thoroughly cleaned to remove teflon layers. The samples are then examined with SEM. Additional processes may be performed to remove silicon fibers, if there are any. Silicon fibers are most likely to appear around the sidewalls of the current limiting apertures. This is because the passivation layers from the first Bosch process prevent the substrate from etching in the following Bosch process. These silicon fibers can be easily removed with an oxidation process followed by an oxide etch. Finally, 20 nm Cr and 200 nm Mo are sputtered onto the sample, as shown in Figure 6-13.n.

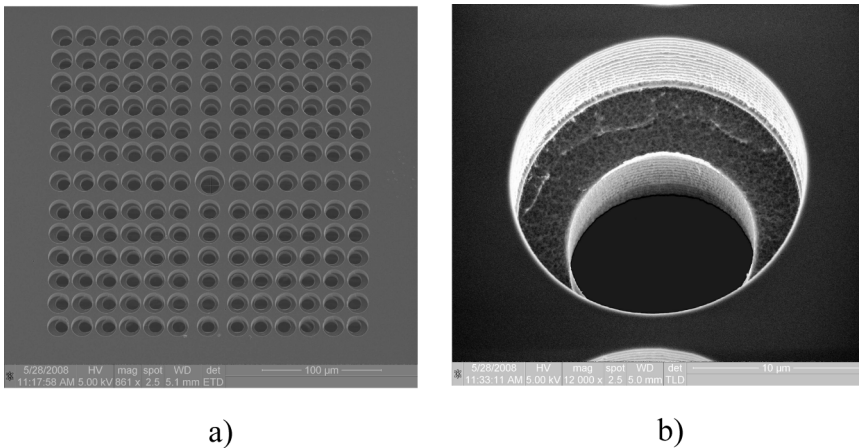


Figure 6-14: a) SEM image of the 13x13 aperture lens array; b) the central aperture lens and its current limiting aperture before metal coating.

Note the notches on the frontside and backside of the aperture lens electrode. They are well aligned to each other and will be used as reference marks for building up the optical stack. The extractor is aligned to the backside notches, which are created by KOH etching. And the two electrodes of the accelerator lens are aligned individually to the frontside notches, which are made in the second Bosch process.

SEM images of the aperture lens array are shown in Figure 6-14.a. Before Mo coating, the samples are examined under SEM, as shown in Figure 6-14.b. The undulating sidewalls are the typical result of the time-multiplexed etching. It indicates that the passivation layers are fully removed. The central aperture lens and its current limiting aperture are larger than the others to ensure a good signal-to-noise measurement for the axial probe. It also facilitates the alignment between the emitter and the optical stack: during the alignment, the emitter is negatively biased around 3000 volts, and the other electrodes are at ground potential, the larger current limiting aperture allows a larger and clearer shadow image. As shown in Figure 6-14, the roundness of the lens holes are improved.

6.3.2 Optical Column Buildup and Alignment

In the multibeam source, the quality of the off-axial beamlets is very sensitive to misalignment between the optical components, and the emitter. The typical alignment resolution of the multibeam source should be in the order of a micron. Such high alignment accuracy can not be achieved by pushing each element against the glass pillars in the four-pillar stage, as in the case of the extractor plate. Instead, the following method is used: the extractor electrode, the aperture lens array, the two-electrode accelerator lens and the glass spacers are aligned and glued subsequently under a mask aligner with sub-micron accuracy. This optical stack is then clamped by its holder. The detailed schematic overview of the optical stack is shown in Figure 6-15. The relative position between the optical stack and its holder is kept by pushing the stack with two springs to the precisely made struts inside the holder, as shown in Figure 6-16. The holder is then put in the four-pillar stage. The four pillar stage provides a coarse alignment of tens of microns. Fine

alignment between the emitter and the optical stack is achieved by the piezo stage.

As shown in Figure 6-15, the dimension of the optical stack is defined by the 3-glass-spacer unit between the two electrodes of the accelerator lens. These glass wafers are diced with an accuracy of $10\text{ }\mu\text{m}$. And they are aligned and glued to each other with an accuracy of $20\text{ }\mu\text{m}$. This spacer unit consists of two $200\text{-}\mu\text{m}$ -thick glass wafers with a hole of 10 mm , and one $300\text{-}\mu\text{m}$ -thick glass wafer with a hole of 7 mm . This configuration creates a longer surface path between the two electrodes of the accelerator lens, which helps to avoid electric breakdown.

The optical stack assembly process starts with aligning the accelerator electrode 1 to the aperture lens array. The alignment takes place in a mask aligner equipped with a custom-made mask holder and a dummy 4 inch wafer holder. The aperture lens array and the $200\text{-}\mu\text{m}$ -thick glass spacer are glued together, acting as the “wafer”. The accelerator electrode 1 serves as the “mask”. Through the transparent lens hole, the accelerator electrode is aligned to the notches on the backside of the aperture array. Once they are aligned, the mask aligner makes contact and presses them against each other. Several drops of UV curable glue are then delivered at the sidewalls by a precision dispensing tool. Subsequently, the UV glue is cured by illuminating it using a UV spot cure machine-Omniculture 1000. The cure time is in the order of a

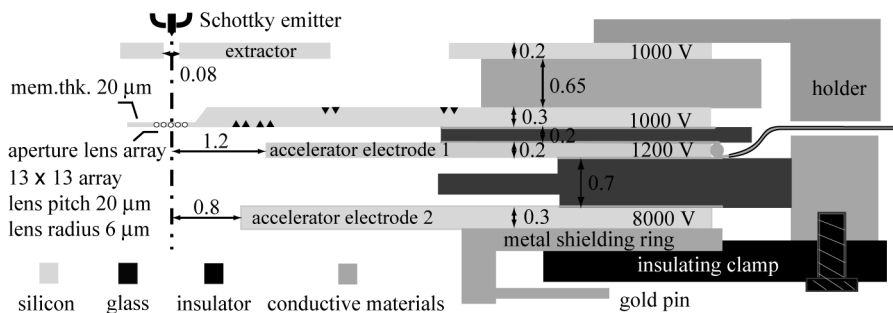


Figure 6-15: Schematic overview of the optical stack, including the extractor, aperture lens array and accelerator lens, which are aligned and glued into one unit and clamped by the holder.

minute, depending on the volume of the drops. With the same procedure, the accelerator electrode 2 and the extractor electrode are bonded to the optical stack.

Three different glues are used in the assembly: OPTOCAST 3505, OPTOCAST 3415 Gen 2, and ECCOBOND 56C. ECCOBOND 56C is a UHV-compatible conductive silver paste. It is used to bond the feedthrough wire (with insulation coating) to the accelerator lens 1.

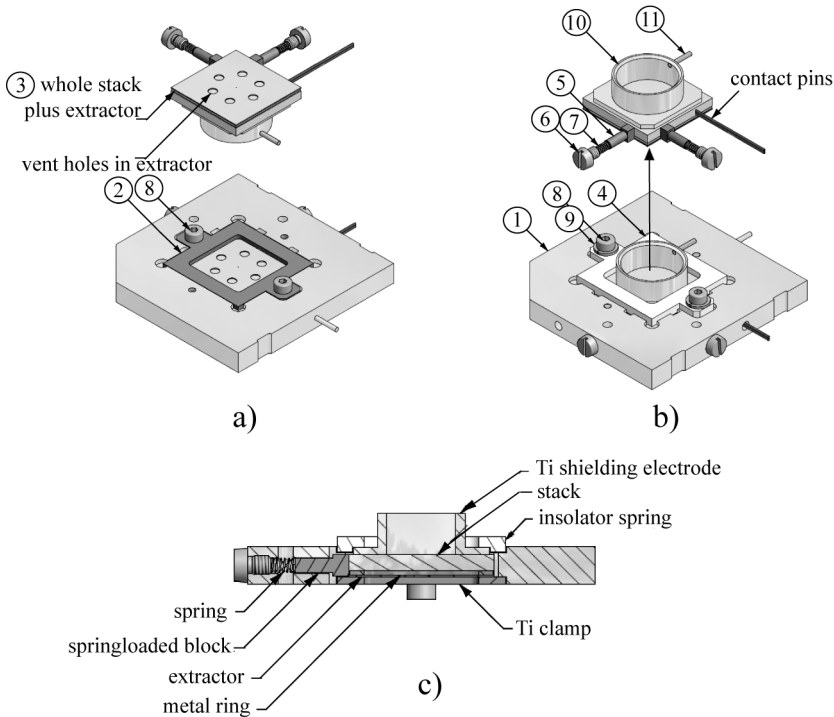


Figure 6-16: Mechanical drawing of the holder and optical stack; a) the front side (facing the emitter); b) the backside; and c) the cross-sectional view, with 1) holder, 2) Ti clamp, 3) optical stack, 4) ceramic clamp, 5) block, 6) screw, 7) non-magnetic spring, 8) screw, 9) spring washer, and 10) shielding electrode.

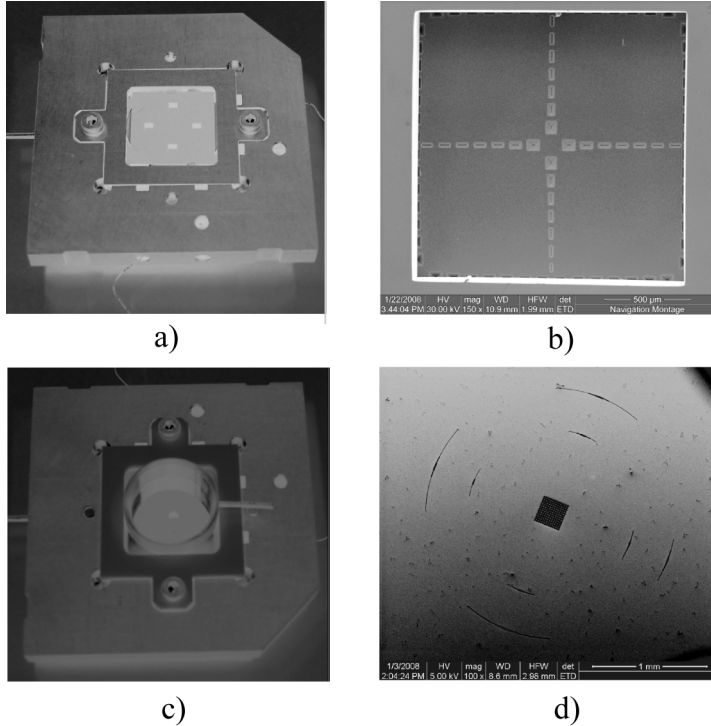


Figure 6-17: a) Photo of the optical stack in its holder (front side); b) sub-micron alignment between the extractor and aperture lens array; c) photo of the optical stack in its holder (back side); d) the alignment marks on the backside of aperture lens array, to which the two electrodes of the accelerator lens are aligned.

OPTOCAST 3505 and 3415 Gen 2 are both UHV-compatible UV curable glues. Both of them have high dielectric strength, high working temperature, low thermal expansion and linear shrinkage. OPTOCAST 3505 is used to bond the three-piece spacer unit. Its low viscosity ensures uniform thickness after bonding. OPTOCAST 3415 Gen 2 is a UV and heat curable one-component epoxy. It is used to glue the rest of the optical components. Generally speaking, due to surface tension, the glue tends to flow underneath the wafer, where it cannot be reached by the UV

light. The uncured glue may cause a serious problem for the ultra high vacuum. The second cure mechanism of OPTOCAST 3415 Gen 2 provides a solution for this situation: the unexposed glue can simply be cured in an oven.

As shown in Figure 6-15, the extractor and the holder are at the same potential, and they are connected to the aperture lens electrode via a metal spacer. The potential of the accelerator electrode 1 is supplied via the wire. The gold pin is joined to the accelerator electrode 2 and they are at ground potential. Figure 6-17 shows a photo of the optical stack in its holder. Through the four venting holes in the extractor plate, the extractor plate is aligned to the reference marks in the aperture lens electrode, as shown in the SEM image in Figure 6-17.b. The alignment marks on the backside of the aperture lens array is shown in Figure 6-17.d, to which the two electrodes of the accelerator lens are aligned.

6.3.3 Discussions

Knife edges are proposed to measure the spot size for each beamlet. Unlike the traditional knife edge measurement where a transmission electron detector or secondary electron detector collects the signal, we make the knife edges on the YAG screen and use a CCD camera to collect the signal. When a beamlet is scanned over a knife edge, image series of the light signal produced by the YAG screen are recorded by the CCD camera. The spot size can be analyzed from the intensity change of those images. The knife edges are made of Tungsten strips, arranged in a hexagonal pattern so that measurement can be taken from three different directions. Then the spot profile is constructed from the knife edge measurements in three directions. Instead of using deflectors to scan the beamlets, the 3-axis piezo stage is used to scan the emitter laterally. The lateral shift of the emitter results in probe position shift at the YAG screen. Since the magnification of the multibeam column is -7, the shift of the emitter will be magnified by the same factor at the YAG screen. The maximum scan distance of the emitter, however, should not be larger than the alignment resolution of the optical column, i.e, 1 μm . Therefore, it is essential that the size of one hexagon is smaller than 7 μm .

In the multibeam source, the off-axial beamlets arrive obliquely on the YAG screen. The incident angle of the outermost beamlet is in the order of 100 mrad. The tilting may induce a large error for the spot size measurements [6.5]: for a 50 keV beam with a convergence semi-angle of 10 mrad, the measured spot size using <100> silicon knife edge increases from 10 nm to more than 40 nm by tilting the sample stage from vertical to 100 mrad. Therefore, the knife edge sample must be calibrated first in SEM, with the help of a photodiode or a CCD image sensor. In the calibration, a probe with similar half-opening angle and beam energy should be measured at different tilting angles. The result of the calibration will be the reference for the future multibeam experiment.

It is difficult to measure the probe current for each beam individually, because the knife edges are made on a conductive surface (usually a layer of Aluminium film is deposited on top of the insulating YAG to prevent charging). However, a good estimation may be obtained by mapping the total YAG current and the probe intensity of a 100-probe image.

6.4 The Blanker Array

The blanker array has been fabricated in the class 10000 clean room at DIMES. A photo of the plating base and a SEM image of a blanker with copper electrodes are shown in Figure 6-18. The blanker array has

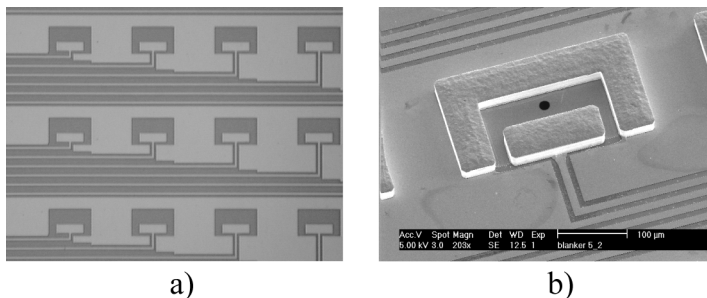


Figure 6-18: a) Photo of the plating base; b) SEM image of a blanker with copper electrodes.

been tested in a multibeam setup. Successful beam blanking has been demonstrated. The experimental result may be found in the dissertation of Van Bruggen [6.1].

6.5 Conclusions

This chapter presents the experimental results of a multibeam source designed with the same principles as that in chapter 4. We demonstrated the key parts of the multibeam source: a Schottky emitter with low extraction voltage; the microfabrication of the optical components, including the blanker array, and the alignment of the optical column.

The low power Schottky emitter is positioned by the 3-axis piezo stage with respect to the extractor electrode. The source is calibrated for uniform angular current density at low extraction voltages.

The quality of microfabrication plays a very important role for the optical performance of the multibeam source. This is due to the high filling factors of the aperture lenses and the accelerator lens. The extractor, aperture lens array and the accelerator lens have been fabricated. But in general, the quality of the microfabrication, in terms of roundness, alignment, etc. should be further improved.

The multibeam source has stringent requirements on the column alignment. We have demonstrated the fine alignment of the emitter and the extractor through the three-axis piezo stage. The optical column is aligned under a mask aligner and glued into one unit. Alignment accuracy of a micron is achieved. The emitter then can be aligned to the glued optical column by the piezo stage.

And finally, the blanker array has been successfully fabricated in the clean room.

Reference

[6.1] M. J. Van Bruggen, *Multi-electron beam system for high resolution electron beam induced deposition*, ISBN: 978-90-9022655-2.

Conclusions

- [6.2] H. S. Kim, M. L. Yu, E. Kratschmer, B. W. Hussey, M. G. R. Thomson, and T. H. P. Chang, *J. Vac. Sci. Technol. B* 16(6), 2468 (1995).
- [6.3] J. Orloff, *Handbook of Charged Particle Optics*, CRC Press (1997).
- [6.4] J. P. Spallas, C. S. Silver, L. P. Muray, T. Wells, and M. El-Gomati, *Microelec. Engi.* 83, 984 (2006).
- [6.5] S. A. Rishton, S. P. Beaumont, and C. D. W. Wilkinson, *J. Phys. E: Sci. Instrum.*, 17, 296 (1984).

Chapter 7

Summary and Conclusions

This work is dedicated to the development of high brightness 100-electron-beam sources to increase the throughput of electron beam lithography, inspection, and electron beam induced deposition. Most multibeam sources in literature are intended for high throughput electron beam lithography, aiming at technology node of 65 nm or larger. The multibeam sources in this thesis are designed for the future generation applications, that is, in case of electron beam lithography and inspection, the technology node of 45 nm or smaller. Therefore, Schottky emitters, having high brightness and small virtual source sizes, are employed for all the concepts. In addition, great effort has been taken to minimize the aberrations in the multibeam sources so that a larger aperture angle can be used and the delivered current is maximized.

In chapter 2 and chapter 3, the footprint of the multibeam sources is limited to 1.5x1.5 mm, so that it can be used as one element in an array of many elements to generate a large number of electron beams. In chapter 2, the broad beam is first split in sub-beams that are focused by a microlens array and subsequently collimated by a deflector array. A

2-electrode immersion microlens array with offset apertures is preferred over an einzel lens array due to its small off-axial aberrations. This configuration avoids the large angular error due to spherical and chromatic aberration of the collimator lens. This multibeam source is capable of generating 100 parallel beams with beam current of approximately 2 nA. In chapter 3, novel electron optical components - an electrostatic aperture lens array and a “zero-strength decelerating macrolens” - are used to direct and project the virtual source image at the deflector array. The aperture lens is capable of having a filling factor as high as 85% due to its small spherical aberration coefficient and it allows skewed incidence up to 110 mrad with very small off-axial aberrations. Together with the macrolens operating at “zero strength mode”, the transverse chromatic aberration and field curvature of the multibeam source are greatly reduced. From a Schottky source with brightness of 10^8 A/m²srV, the multibeam source can produce 100 beams with a probe current of 15.7 nA per beam.

In chapter 4, the multibeam source is not limited by the 1.5 mm pitch, and an accelerating macrolens can be used instead of the decelerating macrolens in chapter 3. This multibeam source comprises a Schottky emitter, an aperture lens array, an accelerator lens, and a conjugate blanker array. The beamlets emerge at 30 kV, compatible with most scanning electron microscope-type systems commercially available. For a Schottky source with brightness of 1.5×10^8 A/m²srV, the multibeam source allows a transmission of more than 1000 nA current to the reduction optics with uniform spot sizes.

The main achievement of this work is the electron-optical design of the 100-electron-beam source. For the multibeam source concepts in chapter 2, 3, and 4, different design principles are used. But all of the concepts have the following unique properties:

1) Large filling factor can be used for the microlenses due to their small spherical aberration coefficients: the filling factor of the microlens is 25%, 85%, and 90% for the multibeam sources in chapter 2, 3 and 4. Note that for the aperture lenses, the aperture angle is not limited by aberrations even with a filling factor of 90%. This should be compared to filling factors of about 10% in typical einzel type lenses;

2) The off-axial aberrations of the microlens arrays are reduced by shifting the current limiting apertures for the off-axial microlenses;

3) The aberrations of the macrolens are minimized; and

4) The field curvature can be compensated: for the multibeam source in chapter 2, the field curvature is compensated by adjusting the lens radius of the microlens array; and for the multibeam sources in chapter 3 and 4, by manipulating the electric field in front of the aperture lenses.

A multibeam source with different requirements: such as magnification, pitch, beam potential *etc.*, can be built with similar components with the same principles.

In chapter 5, the design and fabrication of a multi-electron-beam blanker array has been described. The in-plane crosstalk is minimized by guard walls and the out-of-plane crosstalk is reduced by the presence of a grounded current limiting aperture array plate. The contamination and charging are reduced because the blanker electrodes and lens apertures are protected from direct electron illumination. The blanker array has been successfully fabricated and the testing results can be found in the dissertation of Van Bruggen.

In chapter 6, a multibeam source designed with the same principles as in chapter 4 is built for experiments. A Schottky emitter is calibrated at low extraction voltage by bringing the emitter closer to the extractor using a 3-axis piezo stage. The optical components are fabricated in the Dimes cleanroom. The optical column is aligned and glued into one unit, and the alignment resolution is demonstrated to be around 1 micron.

The future work of this thesis would be to continue the experiments in chapter 6. The most important experiment will be the measurement of the probe sizes and the probe current of the 100-beam-source. The method is discussed in chapter 6.3.3. In order to have satisfactory results, there are several challenges: 1) the quality of microfabrication, in terms of roundness, alignment *etc.*, must be improved; 2) the stability of the power supplies needs to be at least 1 order of magnitude better; 3) the optical column must be built with sufficient alignment accuracy; and 4) the accuracy of knife edge measurement and the probe current mapping should be studied. The knife-edges on a YAG screen have been fabricated and calibrated separately by Zhongzi Wang. The measurement results of the probe sizes and probe current will demonstrate the performance of the

multibeam source, and give insight on the off-axial performance of the Schottky emitter.

Chapter 8

Samenvatting en Conclusies

Dit werk is opgedragen aan de ontwikkeling van een hoge helderheid 100 elektronen bundel bronnen voor het vergroten van de doorvoer van elektron lithografie, inspectie en elektron geïnduceerde depositie. De meeste multi bundel bronnen in de literatuur zijn bedoeld voor hoge doorvoer elektronen lithografie, die zich richtte op de technologie van 65 nm of groter. De multi bundel bron in dit proefschrift is ontworpen voor de toekomstige generatie toepassingen, voor de elektron lithografie en inspectie is dit de 45 nm technologie en kleiner. Daarom zijn Schottky bronnen met hoge helderheid en kleine virtuele bronnen in alle concepten gebruikt. In additie is er grote moeite gestoken in het minimaliseren van de aberraties in de multi bundel bronnen, zodat de geleverde stroom gemaximaliseerd is en een grote openingshoek gebruikt kan worden.

In hoofdstuk 2 en 3 is de voetdruk van de multi bundel bronnen gelimiteerd tot 1.5×1.5 mm, zodat deze gebruikt kan worden als één element in een matrix van meerdere elementen voor het generen van een grote hoeveelheid elektronen bundels. In hoofdstuk 2, is de brede elektronen bundel eerst opgesplitst in sub bundels die gefocuseerd zijn

met micro lenzen en daarna gecollimeerd worden door een deflector matrix. Een 2 elektrode micro immersie lens matrix met compensatie aperturen geeft de voorkeur over een enkel lens vanwege de kleine van de as aberraties. Deze configuratie vermijdt een grote hoek fout veroorzaakt door sferisch en chromatisch aberraties van de collimator lens. Deze multi bundel bron is in staat 100 parallelle bundels met een stroom van ongeveer 2 nA te generen. In hoofdstuk 3 worden nieuwe elektrostatische optisch componenten gebruikt: een elektrostatische apertuur lens matrix en een 'zero strength' vertragende macro lens, voor het projecteren van het virtuele bron beeld op de plek van de deflector matrix. Doordat de apertuur lens weinig sferisch aberraties heeft en hoeken tot 110 mrad accepteert met heel weinig van de as aberraties kan deze gevuld worden tot 85%. Samen met de macrolens in 'zero strength' modes wordt de transversale chromatisch aberraties en veld verbuiging van de multi bundel bron zeer verminderd. Het is mogelijk om 100 bundels te generen met een probe stroom van 15.7 nA per bundel, met een Schottky bron met een helderheid van 10^8 A/m²srV.

In hoofdstuk 4, is de multi bundel bron niet gelimiteerd door de 1.5 mm steek en in dit geval kan er dan een versnellende macro lens gebruikt worden inplaats van een vertragende macro lens, zoals in hoofdstuk 3. Deze multi bundel bron bestaat uit een Schottky bron, een apertuur lens matrix, een versnellende lens en een conjugate blanker matrix. Deze bundels komen te voorschijn met 30 keV, wat vergelijkbaar is met meeste commerciële raster scan elektronen microscopen. Voor een Schottky bron met een helderheid van 1.5×10^8 A/m²srV is de multi bundel bron instaat meer dan 1000 nA stroom naar het reduceer optiek the transporteren met een uniforme spot grootte.

Het grootste succes van dit werk is het ontwerp van de elektron optiek van de 100 elektron bundel bron. In hoofdstuk 2, 3 en 4 zijn andere ontwerp principes gebruikt voor de multi bundel bron concepten. Maar alle concepten hebben de volgende unieke eigenschappen:

1) Grootte lens vul factoren kunnen worden gebruikt door dat alle concepten weinig sferisch aberraties kennen: de vul factor is 25%, 85% en 90% voor de multi bundel bronnen in hoofdstuk 2, 3 en 4. Noteer dat voor apertuur lenzen de openingshoek niet gelimiteerd is door aberraties

zelfs niet met vul factor van 90%. Vergeleken met een vulfactor van ongeveer 10% voor een typische enkel lens;

2) De van de as aberraties van de micro lens matrix zijn gereduceerd door het verplaatsen van de stroom limiterende aperturen voor de van de as micro lenzen;

3) De aberraties van de macro lens zijn geminimaliseerd; en

4) De veld verbuiging kan worden gecompenseerd; in hoofdstuk 2 is dit gedaan door het aanpassen van de lens straal van de micro lens matrix; in hoofdstuk 3 en 4 is dit gedaan door het manipuleren van het elektrische veld voor de apertuur lenzen. Een multi bundel bron met andere eisen, zoals: vergroting, steek, bundel potentiaal etc., kan worden gebouwd met soortgelijke componenten met dezelfde ontwerp principes.

In hoofdstuk 5 is het ontwerp en de fabricatie van een multi elektronen bundel blanker matrix beschreven. De in het vlak cross talk is geminimaliseerd door muurtjes en de uit het vlak cross talk is gereduceerd door een geaard stroom limiterend apertuur te gebruiken. Vervuiling en oplading op de blanker elektrodes en lens aperturen is gereduceerd door ze af te schermen voor directe elektronen. De blanker matrix is met succes gefabriceerd en test resultaten kunnen worden gevonden in de dissertatie van Van Bruggen.

In hoofdstuk 6 is een multi bundel bron ontworpen en gebouwd voor experimenten met dezelfde ontwerp principes als in hoofdstuk 4. Een Schottky bron is gekalibreerd op een laag extractie voltage door deze dichterbij de extraktor te brengen met een 3 assen piezo stage. De optische componenten zijn gefabriceerd in de Dimes clean room. De optische kolom is uitgelijnd en gelijmd tot 1 component en het is aangetoond dat dit kan met een uitlijn fout van ongeveer 1 micron.

Toekomstig werk naar aanleiding van dit proefschrift is het continueren van de experimenten van hoofdstuk 6. Het meest belangrijke experiment is het meten van de probe groottes en stromen van de 100 bundel bron. Deze methode is besproken in hoofdstuk 6.3.3. Om hierbij goede resultaten te behalen zijn er een aantal uitdagingen: 1) de kwaliteit van de micro fabricatie; in de termen van rondheid, uitlijning etc. moet verbeterd worden; 2) de stabiliteit van de voedingen moet ten minste 1 order verbeterd worden; 3) de optisch kolom moet met genoeg uitlijn precisie gebouwd worden; en 4) de precisie van de mes rand metingen en

probe stroom in kaart bringend moet bestudeerd worden. De mes randen op een YAG scherm zijn gemaakt en gekalibreerd door Zhongzi Wang. De resultaten van de metingen van de probe groottes en stromen zullen de prestaties van de multi bundel bron aantonen en zal inzichten geven in de prestaties van een van de as gebruikte Schottky bron.

Acknowledgement

In July 2004, I started my PhD project in Delft. Looking back on these exiting, productive and very enjoyable 4 years, I would like to thank many people for their encouragement, contribution and support.

I would like to express my gratitude to Prof. Pieter Kruit, for introducing me to the world of charged particle optics. This thesis would not have been written without his encouragement and stimulating suggestions.

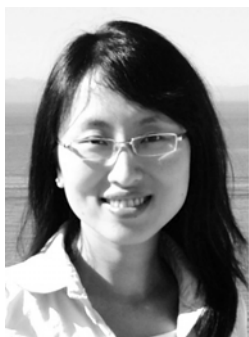
It is my great pleasure to work with my colleagues, Kees, Jim, Martijn, Merijn, Willem, Anda, Anand, David, Ben, Vincenzo, Ali and Christiaan. Martijn has passed his extensive knowledge of multibeam systems while the projects were overlapped. I would like to thank Jim and Kees, who is always patient and have enough time for difficult questions. Special thanks to Merijn for the fruitful discussions and for explaining the difficult term of “off-axial reduced brightness”. I would like to thank Christiaan for translating chapter 7 and the propositions into Netherlands. In addition, I like to express my thanks to Elly and Margaret for supporting and organizing many enjoyable events.

The vital success of my experiment is dependent on the technicians: Vladimir, Carel, Tonny, Jan, Frans and Jacques. I have learnt many microfabrication techniques from Carel and Tonny in the first year during the design and fabrication of the blanker array. Vladimir has taken a big responsibility of fabricating all the optical elements in the multibeam source.

Jan, Frans and Jacques help me with vacuum setups, measurement software and electronics. Together with Jan, a spectacular vacuum level of 10^{-11} mbar has been reached in the new-built vacuum setup. I would like to thank them all for the highly skilled work and valuable contributions.

Finally, I would like to express my deepest gratitude to my parents for their constant support and encouragement in all my professional decisions. I understand it must be difficult for them as the only child is far away. Last but not the least, I would like to acknowledge my husband, Xinyang. He is the reason why I came to the Netherlands in the first place. I would never be able to finish my PhD without him being there.

About the Author



Yanxia Zhang was born in Huhhot, P. R. China on December 16, 1979. She received the degree of B.Sc in Information and Electronic Engineering from Zhejiang University in 2002. From September 2002 to July 2004, she studied in the department of Electrical and Computer Engineering in Concordia University, Montreal, Canada. And she received the degree of M.Sc in April 2005. In July 2004, she joined the Charged Particle Optics Group in Delft University of Technology. There, she worked on designing high brightness multi-electron-beam sources for fast patterning applications. She is working for Mapper Lithography since July 2008.

